2014

IRON AND IRON OXIDE FUNCTIONALIZED MEMBRANES WITH APPLICATIONS TO SELECTED CHLORO-ORGANIC AND METAL REMOVAL FROM WATER

Minghui Gui
University of Kentucky, guiminghui@gmail.com

STUDENT AGREEMENT:

I represent that my thesis or dissertation and abstract are my original work. Proper attribution has been given to all outside sources. I understand that I am solely responsible for obtaining any needed copyright permissions. I have obtained needed written permission statement(s) from the owner(s) of each third-party copyrighted matter to be included in my work, allowing electronic distribution (if such use is not permitted by the fair use doctrine) which will be submitted to UKnowledge as Additional File.

I hereby grant to The University of Kentucky and its agents the irrevocable, non-exclusive, and royalty-free license to archive and make accessible my work in whole or in part in all forms of media, now or hereafter known. I agree that the document mentioned above may be made available immediately for worldwide access unless an embargo applies.

I retain all other ownership rights to the copyright of my work. I also retain the right to use in future works (such as articles or books) all or part of my work. I understand that I am free to register the copyright to my work.

REVIEW, APPROVAL AND ACCEPTANCE

The document mentioned above has been reviewed and accepted by the student's advisor, on behalf of the advisory committee, and by the Director of Graduate Studies (DGS), on behalf of the program; we verify that this is the final, approved version of the student's thesis including all changes required by the advisory committee. The undersigned agree to abide by the statements above.

Minghui Gui, Student

Dr. Dibakar Bhattacharyya, Major Professor

Dr. Thomas Dziubla, Director of Graduate Studies

IRON AND IRON OXIDE FUNCTIONALIZED MEMBRANES WITH APPLICATIONS TO SELECTED CHLORO-ORGANIC AND METAL REMOVAL FROM WATER

DISSERTATION

A dissertation submitted in partial fulfillment of the
requirements for the degree of Doctor of Philosophy in the
College of Engineering
at the University of Kentucky

By
Minghui Gui

Lexington, Kentucky

Director: Dr. Dibakar Bhattacharyya, Alumni Chair Professor of Chemical Engineering

Lexington, Kentucky

2014

ABSTRACT OF DISSERTATION

IRON AND IRON OXIDE FUNCTIONALIZED MEMBRANES WITH APPLICATIONS TO SELECTED CHLORO-ORGANIC AND METAL REMOVAL FROM WATER

The development of functionalized membranes with tunable pores and catalytic properties provides us an opportunity to manipulate the membrane pore structure, selectivity and reactivity. By introducing the functional groups into membrane pores, dissolved metal ions and reactive particles can be effectively immobilized within the polymer matrix for toxic chloro-organic and heavy metal remediation in water.

A polyelectrolyte functionalized membrane platform with tunable pore size and ion exchange capacity has been developed for iron/iron oxide nano-catalyst synthesis and chlorinated organic compound (trichloroethylene, TCE and polychlorinated biphenyls, PCBs) degradation. Highly robust polyvinylidene fluoride (PVDF) microfiltration membranes are used as the support with cross-linked polyacrylic acid (PAA) filled in the pores. By varying the environmental pH, PAA hydrogels have either swelling or collapsing behavior, resulting in different effective membrane pore sizes for different separation purposes. Cation exchange groups (i.e. carboxyl groups) in PAA chains prevent the aggregation and leaching of nanoparticles (NPs) during in-situ synthesis and reaction. Depending on the catalyst loading and residence time, TCE and PCBs can be completely degraded by reduction of zero-valent iron and bimetallic iron/palladium NPs, or iron oxide catalyzed free radical oxidation at near-neutral pH. Biphenyl from PCB dechlorination can be further oxidized by hydroxyl radicals (OH•) generated from hydrogen peroxide (H_2O_2) decomposition. Hydroxybiphenyls and benzoic acid are identified as oxidation products. Line scan and elemental mapping in transmission electron microscopy (TEM) and X-ray photo electron spectroscopy (XPS) characterizations are conducted to understand the effect of iron surface transformation on NP reactivity, and to optimize the membrane functionalization.

The same platform can also be used to remove toxic metal selenium in the scrubber water of coal-fired power plants. By reducing the salt concentration in water or increasing the residence time and temperature, the concentration of selenium oxyanions in functionalized membrane permeate can be reduced to less than 10 μg/L. Selenium is captured in membranes by both iron reduction to metallic selenium and iron oxide adsorption. The full-scale flat sheet functionalized membranes and spiral wound modules have also been developed. Iron NPs with alterable loadings are successfully synthesized

inside the membrane module for real water applications.

KEYWORDS: Membrane separation, water treatment, surface modification, advanced oxidation, pH responsive

MINGHUI GUI
Student's Signature

9/23/2014
Date

IRON AND IRON OXIDE FUNCTIONALIZED MEMBRANES WITH APPLICATIONS TO SELECTED CHLORO-ORGANIC AND METAL REMOVAL FROM WATER

By

Minghui Gui

DR. DIBAKAR BHATTACHARYYA
Director of Dissertation

DR. THOMAS DZIUBLA
Director of Graduate Studies

9/23/2014
(Date)

ACKNOWLEDGEMENTS

First, I would like to thank my advisor Prof. Dibakar Bhattacharyya for his generous support and insightful guidance in the last five years. Thank you for encouraging and inspiring me with your passion and insight on research. I have been fortunate to have you as my advisor, teaching me all aspects of membrane and water research. I also appreciate your critical comments and our high quality discussions, which make me always keep moving forward and become better. My doctoral committee members have been providing me help for improving this research. I would like to thank Prof. Lindell Ormsbee for the discussion about the practical aspects of this research. I would also like to thank Prof. John Balk and Prof. Thomas Dziubla for providing technical support on nanoparticle and membrane characterization.

I would like to thank Ms. Tricia Coakley and Mr. John May in Environmental Research Training Laboratory (ERTL) at University of Kentucky (UK) for their analytical assistance. I also want to thank Dr. Frank Huggins, Dr. Jia Ye, Dr. Dali Qian, Dr. Lei Wang, Xu Jiang, Nicolas Briot, Dr. Phillip Swartzentruber, Dr. Jin Luo, and Mr. Larry Rice for their help on materials characterization. Prof. Yang-Tse Cheng, Prof. Stephen Rankin, Prof. J. Zach Hilt, Prof. Andrew Morris, Prof. Yinan Wei and Prof. Richard Eitel, thank you all for sharing the instruments and resources in your labs.

I also want to acknowledge my previous and current labmates: Dr. Vasile Smuleac, Dr. Li Xiao, Dr. Scott Lewis, Dr. Noah Meeks, Ruo He, Andrew Tomaino, Sebastian Hernandez, Andrew Colburn, Steven Weinman, Brett Miller, Erica Davis, Thao Ngo and Douglas Davenport. Special thanks go to Joe Papp and Chris Stevens, who worked with me on this project throughout their undergraduate studies. I would like to

convey my thankfulness to my classmates and friends at UK: Dr. Qingliu Wu, Xuepei Shi, Sundar Prasanth Authimoolam, Robert Wydra, William Mercke, Jie Pan, Dr. David Cochran, Dr. Zhiqiang Chen, and Dr. Binghui Wang.

Finally, I would like to thank my wife for her help and support in our life. The best part of my time at UK is to meet her. I also want to thank my parents, who are always patient and supporting my decisions emotionally and financially.

This research is supported by the National Institute of Environmental Health Sciences Superfund Research Program (NIEHS-SRP) of the National Institutes of Health (NIH) under Award Number P42ES007380, Department of Energy Kentucky Research Consortium for Energy and Environment (DOE-KRCEE, DE-FG05-03OR23032), and Southern Company in Birmingham, AL. The content is solely the responsibility of the authors and does not necessarily represent the official views of NIH. I also want to acknowledge the significant contributions of Ultura Inc. in Oceanside, CA towards the joint development of full-scale membranes.

TABLE OF CONTENTS

LIST OF TABLES

LIST OF FIGURES

Chapter One Background and Objectives

This chapter provides critical literature reviews on functionalized membrane synthesis, chlorinated organic remediation, and selenium removal technologies. It starts with an introduction of membrane separation technology. This is followed by a discussion about the existing problems in traditional membrane separation. Then an overview of functionalized membrane and its applications is given to explain how to improve the membrane performance via controlling the pore structure. Next, the different methods for chlorinated organic remediation were detailed, with a focus on reductive and oxidative pathways. Finally, the existing selenium removal technologies are discussed since it's an important application of functionalized membranes.

1.1 Membrane Separation Technologies

A membrane is a selective and semi-permeable barrier between two adjacent phases, which can let some substances pass through while retaining the others. Depending on the pore structure and size, commercial membranes can be classified as microfiltration (MF), ultrafiltration (UF), nanofiltration (NF), forward/reverse osmosis (FO/RO), and pervaporation (PV) (Ho and Sirkar 1992; Bernardo, Drioli et al. 2009). Figure 1.1 shows the typical pore size range for membranes used in water treatment. For different separation purposes, different membranes are selected to combine throughput with content. The state-of-the-art membrane technology allows the separation of species, mainly based on size exclusion (MF, UF and NF), charge exclusion (NF), and solubility/diffusivity difference (FO/RO and PV). The driving force is mainly from chemical potential difference across the membrane, including pressure, concentration, and electrical field (e.g. electrodialysis, ED) (Baker 2004; Baker, Wijmans et al. 2010).

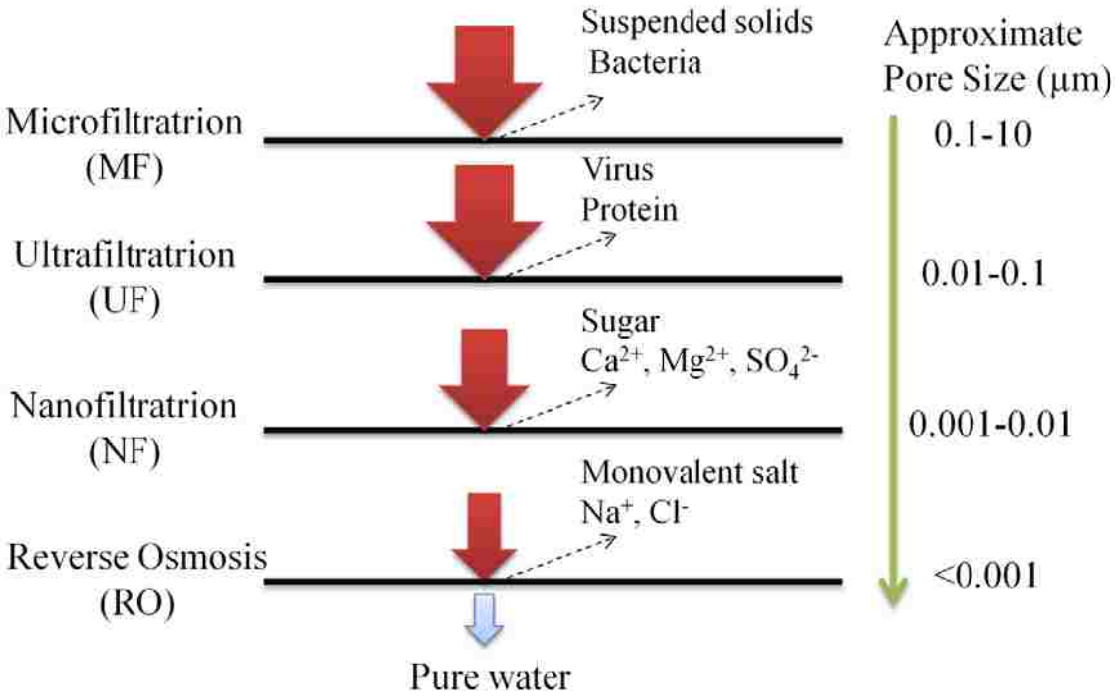

Figure 1.1. Commercial membranes and their applications in water treatment.

Initially inspired by biological membranes existing in nature and human body, various synthetic membranes have been developed since then. However, the poor stability and selectivity of early membranes limited their industrial applications, until the first breakthrough in 1960s when Loeb and Sourirajan synthesized the first practical cellulose acetate (CA) RO membrane (Loeb Sidney 1964). This asymmetric membrane was made with a thin active layer and highly porous substrate, which gave high flux and good stability. However, the hydrolysis and biodegradation of CA could significantly lower the rejection. Later, the stability and performance were further improved by the development of thin-film composite membranes (TFC) with an ultrathin aromatic polyamide skin supported by UF polysulfone membrane on top of non-woven backing materials such as polyester (Lau, Ismail et al. 2012).

Different technologies have been applied to membrane synthesis to form various pore sizes and internal structure. For dense and nonporous membranes like RO and NF, interfacial polymerization is mainly used to create a highly cross-linked aromatic polyamide layer. For porous membranes such as MF and UF, nonsolvent and thermally induced phase separation can create more open structure with “finger” or “spongy” shape (vandeWitte, Dijkstra et al. 1996; Guillen, Pan et al. 2011). Although most membranes are made of organic polymer, some inorganic materials like zeolite (Kosinov, Auffret et al. 2014), alumina (Zhan and Lei 2014), graphene oxide (Huang, Liu et al. 2014; Joshi, Carbone et al. 2014), carbon nanotube (Majumder, Chopra et al. 2005; Walther, Ritos et al. 2013), ceramic (Wei, Fan et al. 2013), and supported liquid film (Patil, Kandwal et al. 2013) also provide the benefits such as improved permeability, selectivity, thermal stability and mechanic strength (Li, Fane et al. 2008).

Today, commercial membranes are playing an important role in energy and environmental applications such as oil and gas, pharmaceutical, medical, and water treatment, especially seawater desalination and industrial wastewater reuse. In industrial plants, membrane modules such as spiral wound and hollow fiber are widely used for different processes. They provide large effective areas for separation, and most importantly their well-designed structure can reduce the membrane fouling such as concentration polarization. Compared to other separation processes, membrane separation is a low energy consumption technology, but there is still a lot of space for improvement. For seawater desalination with RO membranes, the minimum energy calculated from a reversible thermodynamic process is 1.06 KWh/m^3, while the best designed and controlled pilot-scale studies can get about 1.8 KWh/m^3 (Elimelech and Phillip 2011). The growing demand for developing next generation membrane has resulted in the development of membrane functionalization technologies (Ulbricht 2006; Bhattacharyya, Schafer et al. 2013). It provides improved physical and chemical properties, such as high water flux under normal temperature (permeability), precise pore size for molecule separation (selectivity), excellent long-term performance in different water matrix (stability), and ability to capture or degrade specific compounds through chemical reactions (reactivity).

1.2 Functionalized Membrane and Its Applications

There is always a trade-off between permeability and selectivity for traditional membranes. Due to the fouling and polymer degradation with organic and inorganic substances in water matrix, the membrane rejection will decline. Additionally, commercial membranes are not effective for removing some organic compounds with

high solubility/diffusivity in membrane materials. With improvement in membrane formation procedure or post treatment, the functionalized membrane is a potential solution to above issues (Figure 1.2).

1.2.1 Membrane Formation

The membrane pore structure can be manipulated in membrane synthesis, resulting in enhanced permeability and selectivity (Park, Yoon et al. 2003; Nunes, Behzad et al. 2011; Qiu, Yu et al. 2013). Block polymers have been used to create highly ordered pores through direct patterning and self-assembly (Marques, Vainio et al. 2013). Polystyrene-block-polyisoprene (PSt-b-PI) (Hashimoto, Tsutsumi et al. 1997), polystyrene-block-polylactide (PSt-b-PL) (Zalusky, Olayo-Valles et al. 2002), and triblock polyisoprene-block-poly (2-cinnamoylethyl methacrylate)-block-poly(tert-butyl acrylate) (Liu, Ding et al. 1999) have been reported to create nanoporous membranes with high porosity and tunable pores. Average pore size between 20 and 30 nm was obtained.

Another important functionalized membrane is the mixed matrix membrane (MMM). MMMs are mainly made of nonporous organic polymer incorporated with dispersed inorganic particles for gas separation (Nunes and Peinemann 2006). Embedded particles such as molecular sieves or zeolites have higher diffusivity than polymeric materials, and also improve the selectivity of gas molecules in polymer membrane due to their accurate size and shape (Chung, Jiang et al. 2007). Silica particles have also been used to increase the free volume in polysulfone membrane, resulting in a significant enhancement in permeability (Ahn, Chung et al. 2008). With thiol-functionalized silica particles, MMMs can also be expanded to the capture of heavy metals like silver (Ladhe,

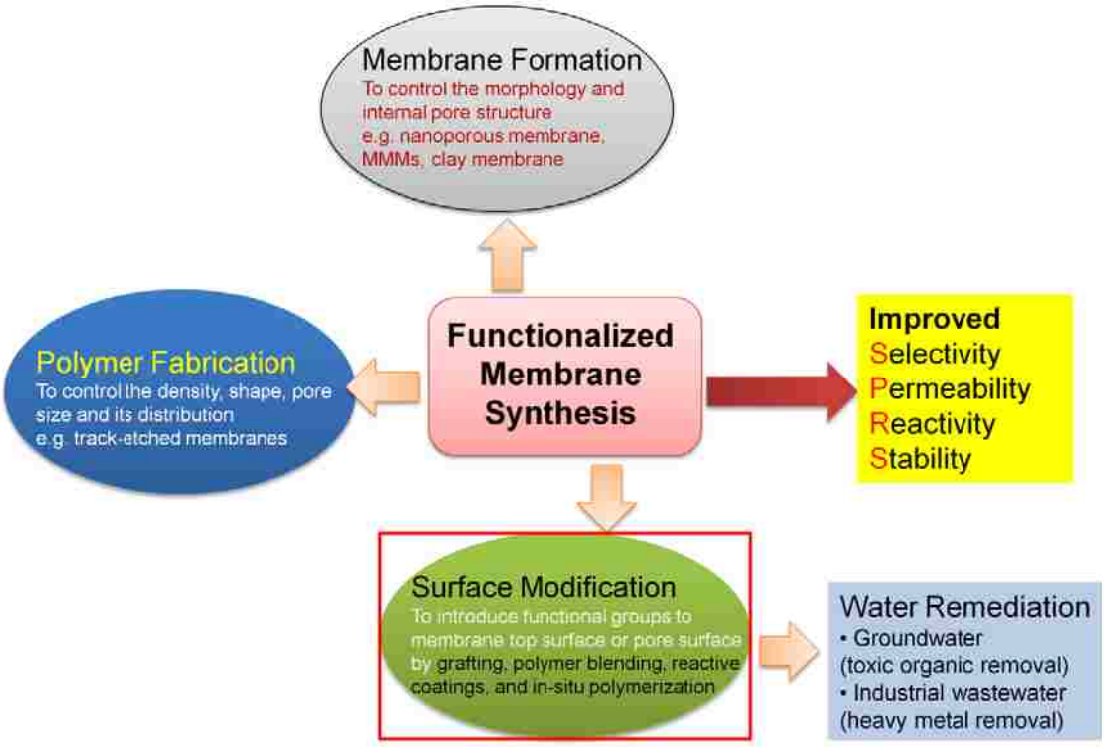

Figure 1.2. Functionalized membrane synthesis techniques

Frailie et al. 2009) and mercury (Meeks, Davis et al. 2013) in water.

Additionally, clays can also enhance the membrane performance when they are added in polymeric membranes to form nanocomposite (Paul and Robeson 2008). Clays act as a semi-permeable filter due to the diffuse double layer (DDL) in pores (Malusis, Shackelford et al. 2003). Although clays are negatively charged, the compensation of excess cations can generate the positively charged electric fields surrounding the clay minerals. The electric fields will reject the charged ions such as K^+, Na^+, and Ca^{2+} via electrostatic repulsion. Those properties provide an opportunity for water desalination and contaminant removal (Prince, Singh et al. 2012). The incorporation of clays also causes the change of glass transition temperature and crystallinity of polymers. The addition of layered-silicate (phyllosilicate) improved the permeability and mechanical strength of polysulfone membranes (Monticelli, Bottino et al. 2007). Due to the ability of improving the proton conductivity, clays have also been applied in the field of fuel cells. Nafion (perfluorosulfonylfluoride copolymer resin)/montmorillonite (MMT) nanocomposite membranes were made via direct melt intercalation of Nafion into MMT or organic modified MMT for methanol fuel cell (Jung, Cho et al. 2003).

1.2.2 Polymer Fabrication

Membrane pore structure including density, shape, size, and size distribution can all be fine-tuned through post fabrication. The development of polymer processing and microfabrication technology provides us an opportunity to create vertically aligned pores with uniform pore size. The track-etched polycarbonate (PC), polypropylene (PP), and polyethylene tetrephthalate (PET) membranes with vertical pores and narrow pore size distribution are already commercial available (Apel 2001; Sartowska, Orelovitch et al.

2012). Those membranes were synthesized by irradiation followed by a controlled chemical etching (e.g. alkali with additives) to make pores. The pore size ranges from 10 nm to 1 micron. The cylindrical pore shape of track-etched membrane makes it an ideal filter to study the transport and adsorption of cells and proteins fouling (Tracey and Davis 1994). Another example with well-controlled internal structure is the anodically oxidized alumina membrane, which has much higher porosity (up to 50%) than track-etched membrane (up to 15%). This membrane is made of a thin layer on top with smaller pore size (down to 10 nm) supported by a thick layer with large pore size (up to 100-200 nm) from the same material. The synthesis process involves the controlled growth of membrane as well as pore development and propagation (Thompson 1997). It is frequently used as support materials for novel separation processes such as biomimetic enzyme immobilization (Chen, Zhang et al. 2014). Some other membranes synthesized via lithography were also reported to have low thickness, uniform pore size, and higher permeability (Han, Xu et al. 2005; Girones, Lammertink et al. 2006).

1.2.3 Membrane Surface Modification

In recent years, membrane surface modifications have become a very important area of activities. By attaching novel functional groups such as carboxyl and amine groups or introducing hydrophobicity/hydrophilicity on membrane top/pore surface, undesired surface interactions such as membrane fouling can be effectively reduced, while useful properties such as reactivity, affinity and responsive behavior can be introduced for improving the selectivity, stability and longevity of membranes. It also extends the membrane separation technology to new application areas such as toxic organic and heavy metal removal.

Grafting

One approach is to graft polymers or functional groups on membrane surface. By using the high energy electron beam, plasma, UV irradiation, or chemical treatment (oxidation), the base membrane materials are activated with the formation of hydroxyl or carboxyl groups on their surface. Those functional groups can attach ligands or polymers through covalent binding such as 1-ethyl-3-[3-dimethylaminopropyl] carbodiimide/N-hydroxysulfosuccinimide (EDC/NHSS) mediated two-step amine coupling (Guan and Zhang 2011). PAA was successfully grafted on PVDF membranes to create negatively charged pores with ion exchange capacity and pH responsive behavior (Gupta and Chapiro 1989; Gupta and Chapiro 1989; Hautojarvi, Kontturi et al. 1996; Clochard, Begue et al. 2004; Nasef and Hegazy 2004; Grasselli and Betz 2005). To better control the growth of polymer gains and reduce the polydispersity, advanced polymerization techniques such as reversible addition-fragmentation transfer (RAFT) and atom transfer radical polymerization (ATRP) were used to attach PAA and poly(2-vinylpyridine) in MF membrane pores (Betz, Begue et al. 2003; Singh, Husson et al. 2005; Singh, Wang et al. 2008; Karppi, Akerman et al. 2010; Zhang, Zhu et al. 2014). Acrylic and sulfo-containing vinyl were also grafted on RO and NF membranes to introduce the hydrophilicity on aromatic polyamide skin surface, and to improve the fouling properties (Belfer, Purinson et al. 1998; Belfer, Purinson et al. 1998). At high degrees of grafting, the monomers such as acrylic acid could penetrate the active layer of NF and RO membranes, and acrylic acid polymerization also took place inside the pores of the support (Freger, Gilron et al. 2002). With functional groups from graft polymerization incorporated in pores, membrane adsorptive chromatography has been developed for

high-throughput antibodies, protein, dye, and metal purification (Bhut and Husson 2009; Orr, Zhong et al. 2013). Compare to ion exchange resin chromatography, adsorptive membranes provide high permeability and shorter diffusion times for molecules to meet active sites in convective mode (Charcosset 2012).

Polymer Blending

Polymers with functionalized groups can be mixed with base polymer for membrane synthesis. Nanofibrous composite membranes (NFC) made by electrospinning of cross-linked hyperbranched polyethyleninimine (PEI) supported by PVDF nanofibrous scaffolds onto commercial PVDF MF membranes had high permeate flux and salt rejection at low pressure (Park, Cheedrala et al. 2012). Positively charged amine groups on PEI enhanced the ion-selectivity of NF membrane via charge exclusion. A temperature and pH responsive membrane was synthesized by phase inversion of PVDF and poly (N-isopropylacrylamide-co-acrylic acid) (PNA) microgels in N, N-dimethyformamide (DMF) (Chen, He et al. 2014). The improved hydrophilicity and antifouling properties were obtained due to PNA microgels incorporated. PAA-polysulfone (PSf) membranes prepared by phase inversion (with DMF as solvent) were studied in heavy metal and dye rejection (M'Bareck, Nguyen et al. 2006). By varying the ratio of polysulfone and polyarylic acid, asymmetric membranes could be obtained with high ion exchange capacity and retention of lead.

Reactive Coatings

Another approach is to coat the membrane pore surface with functional groups via adsorption/adhesion. Layer-by-layer (L-b-L) assembly with polyelectrolytes is an emerging technique for creating a reactive coating on membrane surface. Polycations and

polyanions can interact with each other through electrostatic binding. To enhance the stability of coatings, polyelectrolyte multilayer is always needed (Bruening, Dotzauer et al. 2008; Qiu, Qi et al. 2011; Joseph, Ahmadiannamini et al. 2014). By changing the number of layers and types of functional groups, membranes show enhanced selectivity during solute transport. Highly permeable and ion selective membranes were prepared from poly(L-glutamic acid)/poly(L-lysine) (PLGA/PLL) multilayer, with the first layer covalently attached to PC track-etched membrane (Hollman and Bhattacharyya 2004). The multilayer adsorption of poly(N,N'-dicarboxymethyl) allylamine (PDCMAA) and protonated poly(allylamine) (PAH) shows high Cu^{2+}/Mg^{2+} selectivity (up to 50) due to the facilitated transport of iminodiacetic acid (IDA) groups in PDCMAA (Sheng, Wijeratne et al. 2014). The same phenomenon was also observed in poly (sodium 4-styrenesulfonate) PSS/PAH membrane diffusion dialysis with K^{+}/Mg^{2+} selectivity larger than 350 (Cheng, Yaroshchuk et al. 2013). The multilayer obtained from L-b-L assembly can also be used for catalytic particle synthesis and enzyme immobilization. Enzymes such as glucose oxidase (GOx) were immobilized in PAA/PAH and PSS/PAH functionalized PVDF membrane pores for hydrogen peroxide in-situ generation and groundwater remediation (Datta, Cecil et al. 2008; Lewis, Datta et al. 2011; Palai and Bhattacharya 2013; Palai, Singh et al. 2014). Uniformly dispersed Au nanoparticles were also immobilized in PAA/PAH functionalized membranes, showing high reactivity in 4-nitrophenol reduction (Dotzauer, Dai et al. 2006).

In-situ Polymerization

In-situ polymerization technique allows the direct synthesis of cross-linked polymer with functional groups in porous MF or UF membranes such as PVDF and

polyethersulfone (PES) (Xu, Dozier et al. 2005; Madaeni, Zinadini et al. 2011). Typically, monomers are mixed with initiator and cross-linker in aqueous or organic phase, followed by dip-coating to let polymerization solution diffuse into membrane pores and thermal polymerization. Instead, polymers can be dissolved in solvent followed by cross-linking reaction to form macroscopic entanglement. By incorporating stimuli-responsive polymers such as PAA and poly(N-isopropylacrylamide) PNIPAAm in MF membranes, membrane pores become tunable with environmental pH and temperature. Additionally, PAA provides high ion exchange capacity for membranes, which allows the capture of heavy metals and in-situ synthesis of reactive particles for water remediation.

Extensive research has been done on iron based nanomaterial synthesis in PAA functionalized PVDF membranes, including Fe^{2+}/Fe^{3+} chelates, Fe, Fe/Pd, Fe/Ni, and iron oxides (Li, Bachas et al. 2007; Tee and Bhattacharyya 2008; Venkatachalam, Arzuaga et al. 2008; Li, Li et al. 2010; Smuleac, Bachas et al. 2010; Parshetti and Doong 2012; Seteni, Ngila et al. 2013; Wang, Yang et al. 2013; Xiao, Isner et al. 2013; Yang, Wang et al. 2014). Those functionalized membranes act as a cost-effective platform for simultaneous reaction and separation.

1.3 Chlorinated Organic Compound Remediation

Chlorinated organic compounds such as trichloroethylene (TCE) and polychlorinated biphenyls (PCBs) are potentially carcinogenic and widely distributed in hazardous waste sites. Most of them were used as industrial solvents before being banned by 1980s. However, significant amount is still present in soil and groundwater today.

Lots of effort has been put into the remediation of those compounds. Physical treatments like air stripping, soil venting, activated carbon adsorption, and in-well

aeration are capital intensive (Russell, Matthews et al. 1992), and those organics are released to the environment without degradation. Bioremediation under aerobic or anaerobic conditions can completely destruct TCE by reduction, but the growth of microorganism has to be well controlled (Bowman, Jimenez et al. 1993; Wood 2008; Hazen 2010). To date, chemical remediation is considered as one of the most promising methods. Depending on the reaction mechanism, either reductive pathway with zero-valent iron (Wang and Zhang 1997; Bezbaruah, Krajangpan et al. 2009; He, Zhao et al. 2010; Freyria, Bonelli et al. 2011), or oxidative pathway with hydrogen peroxide, ozone, permanganate and persulfate (Gates and Siegrist 1995; Laine and Cheng 2007; Ahmad, Simon et al. 2011) can be used.

1.3.1 Reductive Pathway

In reductive pathway, zero-valent iron (ZVI) acts as an electron donor. In the presence of chloro-organics such as TCE, iron can directly reduce TCE to ethylene. The overall reduction can be written as,

$$Fe^0 + RCl + H^+ \rightarrow Fe^{2+} + RH + Cl^- \quad \text{(E1.1)}$$

where RCl represents the chlorinated hydrocarbon. Iron can also be corroded in water, forming ferrous ions and hydrogen gas, depending on the aerobic or anaerobic conditions (Johnson, Fish et al. 1998).

$$2Fe^0 + O_2 + 4H^+ \rightarrow 2Fe^{2+} + 2H_2O \quad \text{(E1.2)}$$

$$Fe^0 + 2H_2O \rightarrow Fe^{2+} + H_2 + 2OH^- \quad \text{(E1.3)}$$

Ferrous iron released from iron surface can precipitate as ferrous hydroxide, maghemite and magnetite, which inhibit the electron transfer. TCE degradation rate decreases as the

concentration of ferrous ion increased. (Liu, Tseng et al. 2006). However, dissolved hydrogen gas can't be activated without a suitable catalytic surface.

The development of nanotechnology allows the synthesis of nanomaterials with high specific surface area for heterogeneous catalysis. For example, iron nanoparticles are more effective electron donors than bulk iron (Wang and Zhang 1997). A second metal such as palladium and nickel is usually added to form bimetallic Fe/Pd and Fe/Ni, acting as catalysts for hydrogen activation. Highly reductive hydrogen radicals (H•) can be generated on Pd or Ni surface, and reduce the chloro-organics via hydrodechlorination (He and Zhao 2008; Meyer, Hampson et al. 2009). TCE is reduced to ethane, and PCBs are converted to biphenyl. Iron is continuously consumed to provide the hydrogen gas.

$$Fe^0 + Pd^{2+} \rightarrow Pd^0 + Fe^{2+} \quad \text{(E1.4)}$$

$$H_2 \rightarrow H\bullet + H\bullet \quad \text{(E1.5)}$$

$$TCE + 8H\bullet \rightarrow Ethane + 3H^+ + 3Cl^- \quad \text{(E1.6)}$$

$$PCB + mH\bullet \rightarrow Biphenyl + nH^+ + nCl^- \quad \text{(E1.7)}$$

The field study with carboxymethyl cellulose (CMC) stabilized iron nanoparticles and trace Pd coating shows that chlorinated ethene concentrations were reduced first by chemical reduction, followed by biological dechlorination for sustained enhanced destruction of chlorinated ethenes in the subsurface (He, Zhao et al. 2010).

To extend the long-term performance of iron nanonparticle, iron sulfides were synthesized on iron surface to preserve the capacity of the system and to maintain strongly reducing conditions (Kim, Kim et al. 2011; Fan, Anitori et al. 2013; Kim, Kim et al. 2014). Fe/FeS has advantages over iron oxide coated iron (Fe/FeO) with respect to reactivity and longevity.

1.3.2 Oxidative Pathway

In-situ chemical oxidation (ISCO) has been widely used in water remediation (Huling and Pivetz 2006) with oxidants such as permanganate (MnO_4^-), ozone (O_3), persulfate ($S_2O_8^{2-}$), and hydrogen peroxide (Fe^{2+}/H_2O_2, UV/H_2O_2). Permanganate can mineralize many contaminants by direct or free radical oxidation over a wide pH range (3.5-12.0). However, it's not effective on some recalcitrant organics such as benzene and PCBs. Ozone is also a strong oxidant, but its on-site generation is required due to its instability (Amarante 2000). Persulfate has been proven effective for BTEX oxidation. To enhance the production of sulfate radicals, iron containing catalysts are usually added (Ahmad, Teel et al. 2012).

Fenton Reaction

Fenton reaction has been extensively studied due to its applicability in different scenarios. In aqueous phase, hydroxyl radicals (OH•) are produced via the reaction of ferrous ions with H_2O_2 under the acidic conditions (pH 3-4). Ferric ions formed in this process can also react with H_2O_2 to regenerate the ferrous ions. OH• can immediately oxidize most organic contaminants nonselectively ($k=10^7$ to 10^{10} $M^{-1}s^{-1}$) (Pignatello, Oliveros et al. 2006), resulting in low concentration at the steady sate (10^{-6} to 10^{-4} M). In large-scale treatment, H_2O_2 and ferrous salts can be co-injected to the subsurface directly, and low concentration of H_2O_2 solution is preferred and can be added continuously to reduce its overall consumption. However, a rapid decomposition of H_2O_2 is always observed due to its reaction with minerals and microorganism in soil. The transport distance of reactants from injection wells is limited by the side reactions and formation of ferric hydroxide precipitates.

Modified Fenton Reaction

A lot of work has been done to improve the Fenton system and among them two ways are most promising. One is to extend the useful pH range to the near neutral conditions by adding the ligands. The nontoxic iron-chelating agents such as sodium pyrophosphate (Venny, Gan et al. 2012), chitosan (Lee and Lee 2010), citrate (Seol and Javandel 2008; Lewis, Lynch et al. 2009), gluconic acid (Ahuja, Bachas et al. 2007), and phosphotungstate (Lee and Sedlak 2009) can stabilize iron in aqueous phase without forming iron hydroxide precipitates.

The other way is to use the heterogeneous Fenton reaction with iron oxides as the catalysts for H_2O_2 decomposition (Tyre, Watts et al. 1991; Ravikumar and Gurol 1994; Miller and Valentine 1995; Lin and Gurol 1998; Valentine and Wang 1998; Huang, Lu et al. 2001; Yeh, Chen et al. 2004; Hartmann, Kullmann et al. 2010). The reactions of iron oxide with H_2O_2 are shown in Table 1.1. Different forms of iron oxide have been studied such as goethite, ferrihydrite, hematite and magnetite. The Fenton-like reaction forms free radicals such as OH• or ferryl ions (IV) based on different mechanisms (Keenan and Sedlak 2008), which further oxidize the aliphatic and aromatic organics. Magnetite is one of the most efficient iron oxide catalysts due to the existence of reactive Fe(II) sites in its structure. Fe^0/Fe_3O_4 composites prepared by mechanical grinding and thermal treatment show enhanced reactivity towards the oxidation of methylene blue via electron transfer between Fe^0 and Fe(III) (Costa, Moura et al. 2008). The surface area normalized rate constants are similar for most iron oxides (Valentine and Wang 1998; Huang, Lu et al. 2001; Kwan and Voelker 2003). Therefore, iron oxide nanoparticles and nanowires with high specific surface area were synthesized to create more catalytic sites (Ai, Lu et al.

Table 1.1. Modified Haber-Weiss mechanism for H_2O_2 decomposition on iron oxide surfaces. ≡Fe(II) and ≡Fe(III) stand for iron oxide surfaces.

$\equiv Fe(II) + H_2O_2 \rightarrow \equiv Fe(III) + OH^- + OH\bullet$
$\equiv Fe(II) + OH\bullet \rightarrow \equiv Fe(III) + OH^-$
$H_2O_2 + OH\bullet \rightarrow H_2O + HO_2\bullet$
$OH\bullet + OH\bullet \rightarrow H_2O_2$
$OH\bullet + HO_2\bullet \rightarrow H_2O + O_2$
$HO_2\bullet + HO_2\bullet \rightarrow H_2O_2 + O_2$
$H_2O_2 + HO_2\bullet \rightarrow H_2O + O_2 + OH\bullet$
$\equiv Fe(III) + H_2O_2 \rightarrow \equiv Fe(II) + H^+ + HO_2\bullet$
$\equiv Fe(III) + HO_2\bullet \rightarrow \equiv Fe(II) + H^+ + O_2$
$\equiv Fe(II) + HO_2\bullet \rightarrow \equiv Fe(III) + HO_2^-$

2007; Zelmanov and Semiat 2008; Giraldi, Arruda et al. 2009). Silica and alumina supports further improved the performance of iron oxide catalysts in dye and phenol degradation due to the interaction of Fe with Si and Al (Pham, Lee et al. 2009; Pham, Doyle et al. 2012). The soil normally contains all three elements, which provides a benefit for PCB oxidative degradation (Ahmad, Simon et al. 2011). Iron nanoparticles in oxygenated water can also produce H_2O_2 and OH• for the oxidation of molinate (Joo, Feitz et al. 2004), benzoic acid (Joo, Feitz et al. 2005; Lee, Keenan et al. 2008) and methanol (Keenan and Sedlak 2008; Lee and Sedlak 2008). A recent study further proved that the free radical production is primarily produced by surface catalysis of iron oxides instead of the dissolved iron released from the particle surface. The catalytic sites are much more effective than the dissolved ferric ions in terms of producing OH• (Voinov, Pagan et al. 2011). In addition to iron oxide, some other iron related materials were also studied for heterogeneous Fenton reaction (Pouran, Raman et al. 2014). FeOCl can generate the free radicals 2-4 orders of magnitudes greater than that over iron oxides due to its unique structural configuration of iron atoms and the reducible electronic properties (Yang, Xu et al. 2013).

1.4 Selenium Oxyanion Removal Technologies

Selenium (Se) is an essential trace element in human and animal nutrition. However, the recommended selenium intake for human is limited between 40 μg and 400 μg per day. Higher level of Se turns out to be toxic for human due to its tendency to accumulate in soft body tissue. Selenium is widely distributed in soil and rock at ppm (mg/L) level, and can easily be accumulated in mining and manufacturing wastewater and agriculture drainage (Lemly 2004; Zhang, Wang et al. 2005). Depending on redox

and pH conditions, selenium can exist in different valence states. The potential-pH equilibrium (Pourbaix) diagram of selenium-water system is shown in Figure 1.3 (Bouroushian 2010). The oxyanions selenate (VI) and selenite (IV) are two main species in the environment, while elemental selenium (Se^0) and selenide (-II) have low water solubility and are usually found under reducing conditions. Other forms can be found in organism as amino acids and enzymes such as selenocysteine.

Conventional water treatment technologies such as coagulation with ferric sulfate and alum are not effective for selenium in pilot plant studies (Lalvani 2004). The other existing physical and chemical methods include ion exchange (Maneval, Klein et al. 1985), membrane filtration (Oppelt 2001), biological reduction (Hageman, van der Weijden et al. 2013), adsorption (Zhang and Sparks 1990; Jordan, Ritter et al. 2013), and chemical reduction (Olegario, Yee et al. 2010; Yoon, Kim et al. 2011).

1.4.1 Ion Exchange

The electrostatic binding between strong-base anion exchanger resins and selenium oxyanions is highly dependent on environmental pH and ionic strength in water. The removal efficiency is related to the concentrations of other anions such as sulfate and nitrate in water. Sulfate behavior in ion exchange is identical to selenate, and the selenite removal is also limited by sulfate and nitrate.

1.4.2 Membrane Filtration

Commercial membranes such as NF membrane have been studied for selenium removal (Kharaka, Ambats et al. 1996). More than 95% removal was achieved. Compared to RO membrane, NF membrane is more cost-effective since it has higher water permeability with lower pressure drop. However, the concentrated selenium in the

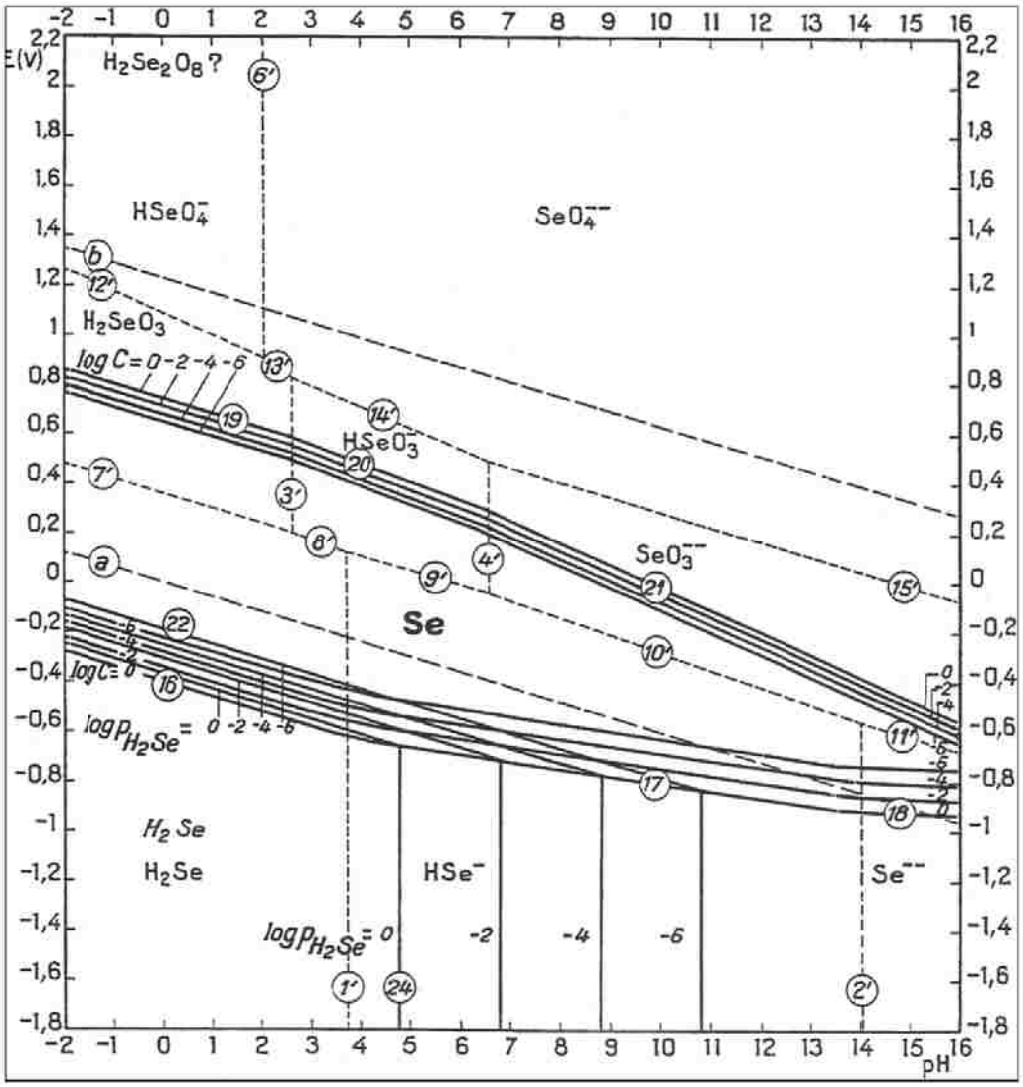

Figure 1.3. Potential-pH equilibrium (Pourbaix) diagram for selenium-water system at 25 °C (Bouroushian 2010).

retentate requires further treatment like crystallization or cementation. Additionally, selenium always exists with high concentrations of salts, which increase the osmotic pressure significantly, resulting in higher energy consumption during the membrane separation.

1.4.3 Biological Reduction

Biological treatment such as bacterial/enzymatic reduction by using sulfate reducing bacteria (e.g. Pseudomonas stutzeri) has been proved to have long-term treatability. Sulfate with concentration below 4000 mg/L doesn't show any significant interference towards selenium reduction by using this method. Previous studies show that Se (VI) was first reduced to Se (IV), followed by further reduction to Se^0 by anaerobic bacteria (Maiers, Wichlacz et al. 1988; Oremland, Hollibaugh et al. 1989). Commercial selenium removal processes such as ABMet (GE) can reduce more than 99% selenium in flue-gas desulfurization (FGD) water through biological reduction (Sonstegard, Pickett et al. 2008). The core part is a biofilter system, which includes an activated carbon packed bed impregnated with selenium reducing bacteria. Selenium concentration below 5 μg/L was achieved. Additionally, nitrate and nitrite were also reduced to nitrogen gas. However, the growth of microorganism has to be well controlled, and thus the cost of this treatment is relatively high.

1.4.4 Adsorption

Selenium oxyanion adsorption with alumina, activated carbon and iron oxides has been established. Activated carbon adsorption is not effective for selenium, while alumina only works for selenite. Iron oxides forms either inner- or outer-sphere surface complexes with selenate (Yamaguchi, Okazaki et al. 1999; Peak and Sparks 2002; Das,

Hendry et al. 2013), but these complexes are not stable in the presence of other anions such as sulfate. Although ferrihydrite was selected by US EPA as the Best Demonstrated Available Technology (BDAT) for selenium (selenite) removal, its adsorption capacity was low (around 10 mg Se/g ferrihydrite). Polymers with positively charged amine groups such as chitosan can attract negatively charged selenium oxyanions by electrostatic interactions. However, previous study shows that low pH environment is required to achieve high removal efficiency (Qian, Huang et al. 2000).

1.4.5 Chemical Reduction

Zero-valent iron (Fe^0) and its bimetallic nanoparticles (Mondal, Jegadeesan et al. 2004; Huang, Peddi et al. 2013) were reported to reduce Se (VI, IV) to Se^0 or Se (-II), which primarily precipitates on iron surface. Ferrous ions released in electron transfer reaction will precipitate as hydroxide, and some other iron oxides can also be formed due to subsequent oxidation. Those Fe(II) bearing materials could also reduce Se (VI, IV) to Se^0 (Murphy 1988; Myneni, Tokunaga et al. 1997; Zingaro, Dufner et al. 1997; Scheinost and Charlet 2008; Schellenger and Larese-Casanova 2013). High salt concentration can lower the reduction rate through the competing adsorption (Zhang, Wang et al. 2005).

1.5 Research Objectives

Although nanomaterials such as iron and iron oxide nanopaticles have been extensively studied in the lab scale for groundwater remediation and industrial water treatment, their applications in real world are limited due to the potential threat to environment and the unknown toxicity to human. For underground water treatment such as chloro-organic remediation, the direct injection of unsupported nanoparticles may cause serious environmental issues due to the particle leaching, such as

oxidation/reduction potential, turbidity, local pH/temperature, and dissolved heavy metals. Additionally, those particles will stay in groundwater system for a long period, and no effective way exists to completely remove them after remediation. For aboveground water treatment, the separation of particles from treated water is critical since nanoparticles can easily get access to the drinking water source. The aggregation and oxidation of particles may also significantly lower the reactivity. Therefore, a support or stabilizer is needed to enhance the stability of nanoparticles and facilitate the separation step. Although many supporting materials such as silica (Zheng, Zhan et al. 2008; Meeks, Smuleac et al. 2012), activated carbon/carbon nanotubes (Tseng, Su et al. 2011; Zhan, Sunkara et al. 2011), polyelectrolytes (Kanel, Goswami et al. 2008; Phenrat, Kim et al. 2009; Golzar, Saghravani et al. 2014) and polysaccharides (Dalla Vecchia, Luna et al. 2009; Gong, Liu et al. 2014) have been used to control the particle size and reduce the aggregation, the functionalized membranes provide added benefits such as highly porous structure and convective flow treatment (Figure 1.4). With functionalized membrane supported iron and iron oxide, pollutants can be removed when they are permeated through the membranes.

The overall objective of this research is to integrate nanotechnology with membrane separation for developing a functionalized membrane platform with reactive nanomaterials in different water applications, especially in toxic organic and metal removal (Figure 1.5). The specific objectives include:

- To develop and optimize membrane pore functionalization methods with polyelectrolytes (e.g. PAA) for metal capture and reactive particle in-situ synthesis;

- To study the synthesis of stabilized iron (Fe, Fe/Pd) and iron oxide (ferrihydrite, magnetite) nanoparticles in aqueous phase and in functionalized membranes (PVDF-PAA);
- To understand the effects of pore functionalization on membrane transport properties including membrane permeability, pH responsive behavior and ion exchange capacity;
- To establish the surface analysis methodologies for both polymeric membrane and iron related nanomaterial characterization, with a focus on understanding the role of surface oxidation and iron/iron oxide core-shell structure in enhancing the nanoparticle reactivity for free radical generation;
- To correlate the membrane pore and surface structure with membrane synthesis for scale-up formulation;
- To evaluate the reactivity of membrane supported iron and iron oxide nanoparticles in reductive/oxidative dechlorination of TCE and PCBs;
- To establish the reaction kinetics of TCE and PCBs with polymer stabilized and membrane supported iron and iron oxide naonparticles;
- To determine the reaction intermediates and understand the subsequent oxidation mechanism during the free radical oxidation of selected chloro-organics and related compounds (e.g. biphenyl) with iron and iron oxide as catalysts;
- To evaluate the reactivity of membrane supported particles for TCE removal in real groundwater and selenium oxyanion removal in coal-fired power plant scrubber water.

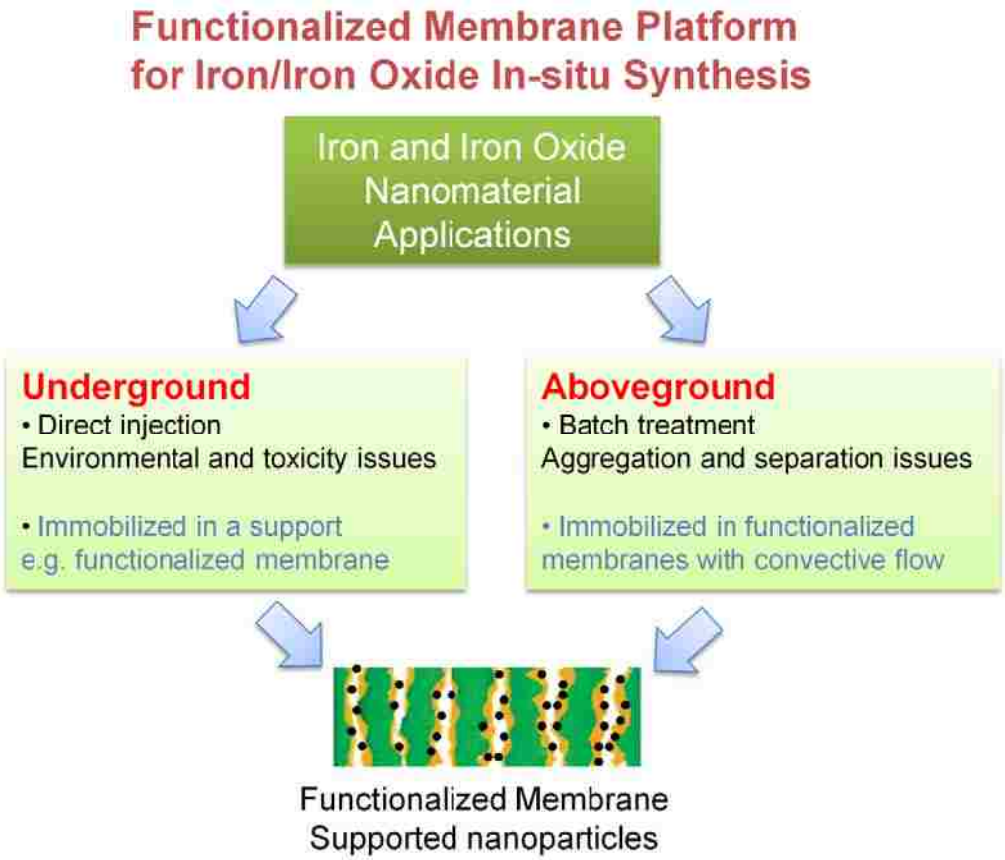

Figure 1.4. Functionalized membrane applications (underground and aboveground) in water treatment

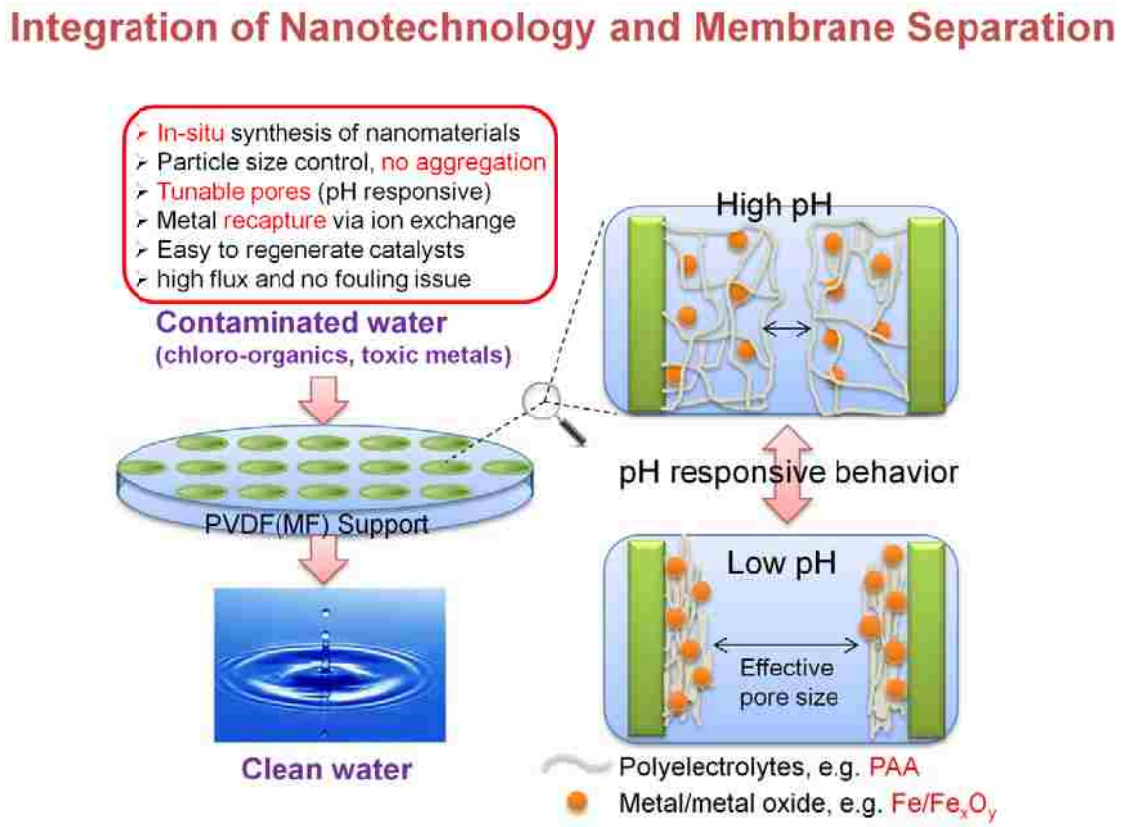

Figure 1.5. Overall research objective: integration of nanotechnology and membrane separation

Chapter Two Materials and Methods

This chapter gives the details of materials, experimental methods, equipment and set-up used, and analytical methods, with a focus on membrane pore functionalization, iron based nanoparticle synthesis in membranes, and dechlorination experiments.

2.1 Materials

All chemicals used in the study were reagent grade without further purification. Sodium borohydride, sodium carboxymethyl cellulose (MW=90000), γ-Fe_2O_3 nanoparticles, 1,2-dibromoethane (EDB), potassium tetrachloropalladate (II), titanium (IV) oxysulfate (15 wt% in dilute sulfuric acid) and selenium powder were purchased from Sigma-Aldrich. Hydrogen peroxide (30 wt%), sodium chloride, sodium sulfate, calcium chloride dihydrate, magnesium sulfate heptahydrate, sodium hydroxide, sulfuric acid, hydrochloric acid, nitric acid (trace metal grade), iron and selenium reference standard (1000 mg/L), pentane, trichloroethylene (TCE), and ferrous chloride tetrahydrate were obtained from Fisher Scientific. Acrylic acid, ammonium persulfate, N,N'-methylenebisacrylamide (NNMA), ethanol, and sodium selenite were purchased from Acros Organics. Sodium selenate was purchased from Alfa Aesar. Potassium persulfate was purchased from EM Science. Ethylene glycol (EG) was purchased from Mallinckrodt. Sodium nitrate (5 M) was obtained from LabChem Inc. PCB standards such as 2-chlorobiphenyl, biphenyl, and hydroxylated biphenyls were obtained from Ultra Scientific.

Hydrophilized PVDF microfiltration membranes (DVPP14250, average pore size: 0.65 μm, thickness: 125 μm, porosity: 70%, diameter: 142 mm) were obtained from EMD Millipore. Full-scale hydrophilized PVDF400HE and functionalized PVDF400HE-

PAA microfiltration membranes were synthesized in Ultura Inc. Membrane thickness is 200±5 μm, including PVDF (70±5 μm) and polyester fabric backing (125±5 μm). The average pore size from bubble point tests is 420 nm for non-functionalized membranes and 124 nm for functionalized membranes. Membrane porosity is 50±5%. The spiral wound module of PVDF400HE-PAA has an effective area of 5 ft^2. All solutions were prepared with Milli-Q ultrapure deionized (DI) water (18.2 MΩ•cm at 25 °C). Deoxygenated water was obtained by purging nitrogen gas into DI water for 30 min.

2.2 Experimental Methods

2.2.1 Membrane Functionalization

Lab-scale Membrane Synthesis

PVDF membrane was functionalized by in-situ polymerization of acrylic acid (AA) in aqueous phase (Figure 2.1). The polymerization solution contained the monomer acrylic acid (AA, 0.9-4.9 M), initiator ammonium persulfate (1 mol% of AA), cross-linker NNMA (1 mol% of AA), and deoxygenated water. PVDF membranes (diameter: 14.2 cm) were dipped into this solution for 5 min, sandwiched between two glass plates after removing the solution from top surface of membranes with nitrogen purging, and put in the oven at 70 °C for 1 h. The membrane was kept under an atmosphere of nitrogen to minimize the oxygen inhibition of polymerization. With thermal treatment, the cross-linked PAA was formed within 30 min. Membranes were rinsed with DI water to remove the unreacted monomers and byproducts before use.

PVDF membranes were also functionalized by PAA with ethylene glycol as a cross-linker. The polymerization solution consisted of monomer AA (2.9-4.8 M), initiator potassium persulfate (1 mol% of AA), cross-linker ethylene glycol (6 mol% of AA), and

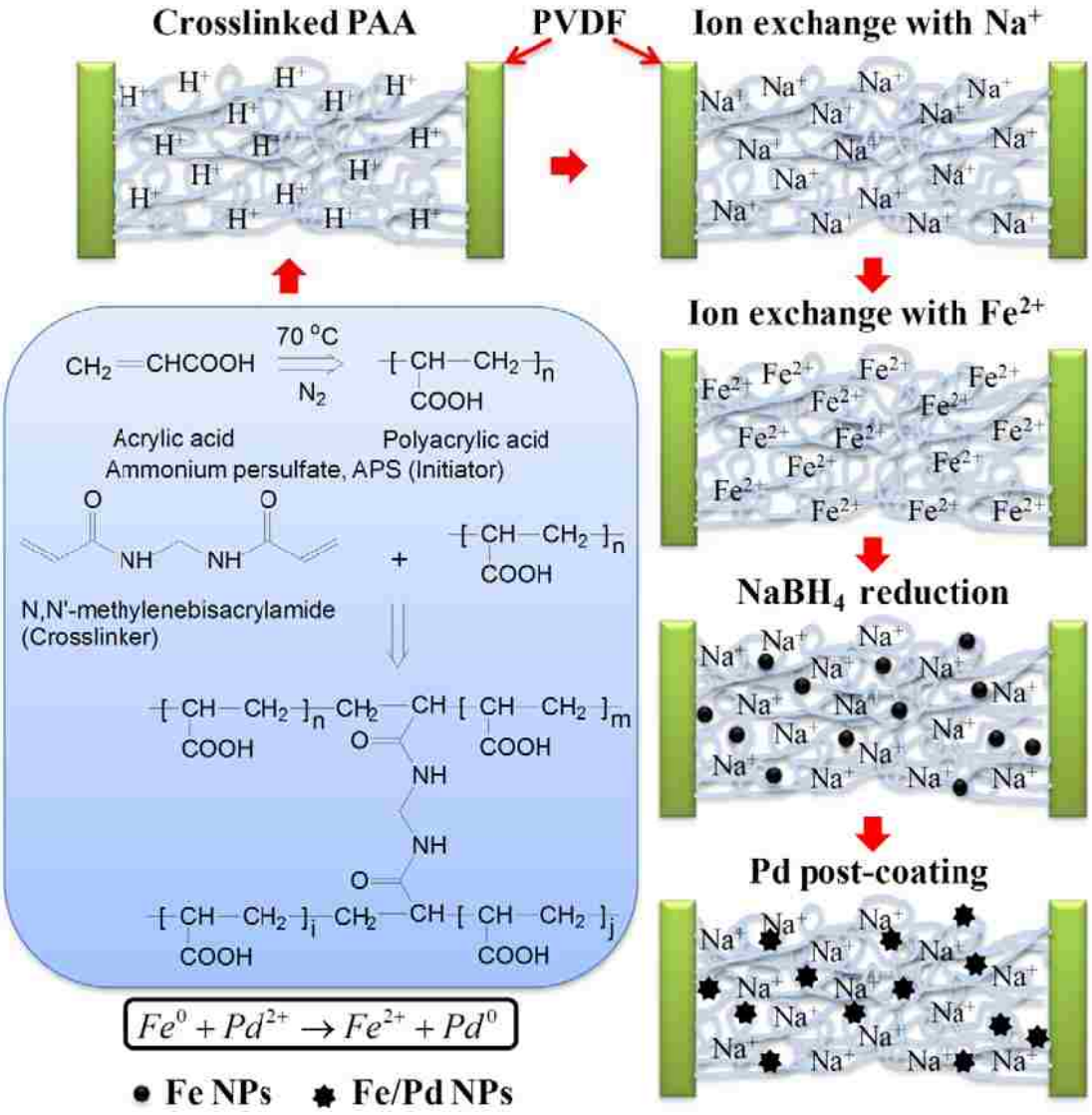

Figure 2.1. PVDF membrane pore functionalization by in-situ polymerization of acrylic acid (AA) and synthesis of Fe/Pd bimetallic nanoparticles.

deoxygenated water. After the same dip-coating in polymerization solution, membranes were put in the oven at 90 °C for 4 h. After polymerization, membranes were washed with ethanol (70 vol%) and DI water before use.

Full-scale Membrane Synthesis (Flat sheets and Modules)

To establish that functionalization steps could be scaled up, full-scale PVDF-PAA flat sheets (40 inches wide and 300 feet long) and spiral wound modules were developed by collaborating with Ultura Inc. in Oceanside, CA. The full-scale PVDF membranes were made with nonwoven polyester backing (highly open structure, thickness: 120 μm) to increase the material stability for ease of making spiral wound modules. The polymerization solution was similar as that used in lab-scale study except lower amount of acrylic acid to reduce the viscosity of solution. A small amount of PAA aqueous solution was also added to accelerate the formation of cross-linked PAA. During the manufacturing, the solution was pulled through PVDF membranes by applying vacuum from the backing side, followed by surface cleaning with air knife.

2.2.2 Membrane Permeability and pH Responsive Behavior Study

Water permeability of PVDF-PAA membranes was evaluated by using a stainless steel pressure cell (Sepa ST, GE Osmonics, effective membrane area: 13.2 cm^2) in dead-end mode (Figure 2.2) or a cross-flow setup in convective mode (Figure 2.3). Water flux was measured at three different pressures with three replicates at each pressure, and the average values were shown here. For pH responsive experiments, no buffer solution was used. DI water at different pH was passed through the membrane until the permeate pH was identical to feed pH. Water permeability was determined at this equilibrium.

2.2.3 Iron Based Nanoparticle Synthesis in Aqueous Phase

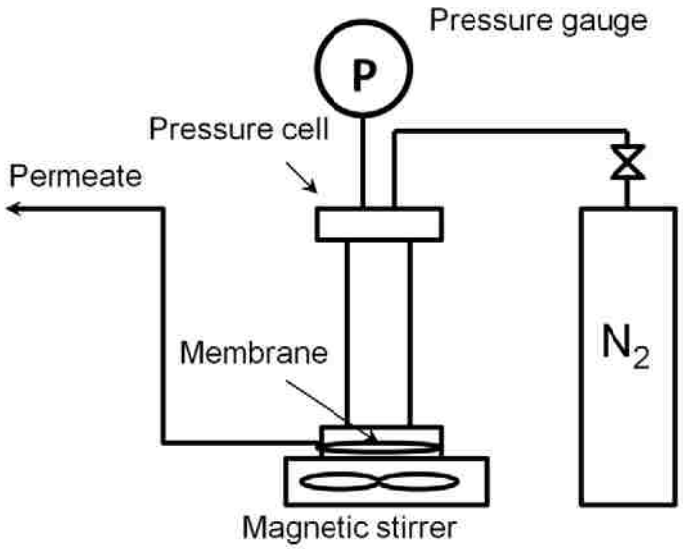

Figure 2.2. Lab-scale membrane evaluation system (dead-end) for water permeability test.

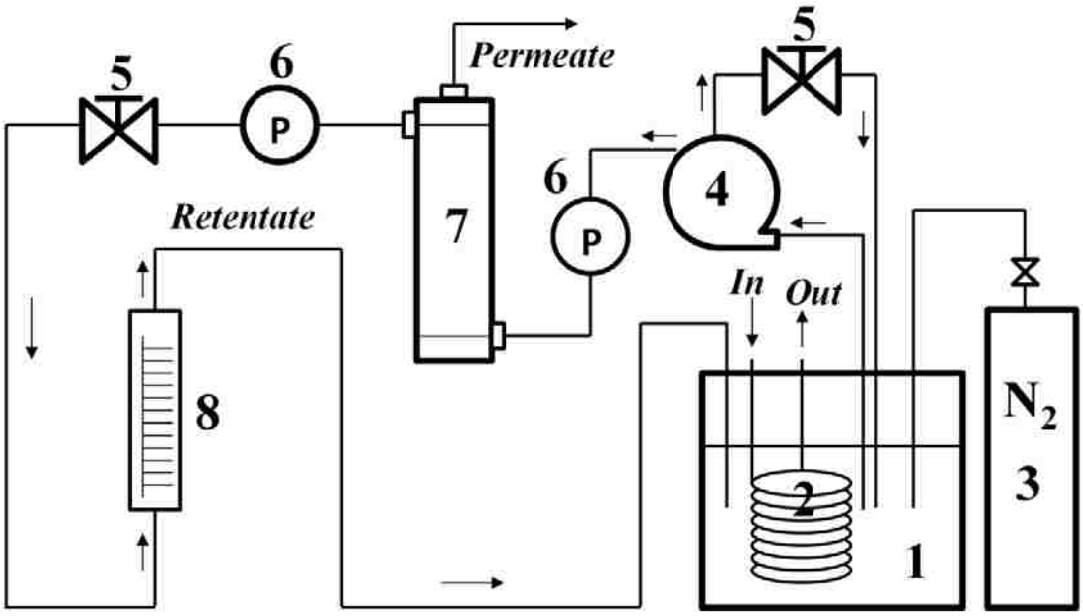

Figure 2.3. Full-scale functionalized membrane module (PVDF400HE-PAA) evaluation setup including water permeability test and iron nanoparticle immobilization.

1. Feed tank (NALGENE, HDPE tank, 10 Gallon)

2. Cooling coil

3. Nitrogen gas tank (to make the deoxygenated water for iron nanoparticle synthesis)

4. Pump (Procon SS 5 Series, ¾ HP, 3.8 GPM, 250 PSI max)

5. Globe valve (SHARPE, ½'')

6. Pressure gauge (ASHCROFT, stainless steel, 300 PSI max)

7. Functionalized membrane module (PVDF400HE-PAA spiral wound module)

8. Flowmeter (Blue-White Industries LTD, 2 GPM max)

All other tubes and fittings used were all purchased from McMaster Carr.

Unsupported Iron and Iron/Palladium (Fe/Pd) Bimetallic Nanoparticles

Fe and Fe/Pd nanoparticles were synthesized in aqueous phase via borohydride reduction and post-coating. $NaBH_4$ (90 mM, 5mL) was added into $FeCl_2$/$FeSO_4$ solution (12 mM, 15 mL) to form zero-valent iron. Those particles were separated with a magnet and washed with deoxygenated water twice. Pd was coated on iron surface by mixing freshly made iron nanoparticles with K_2PdCl_4 solution (153 μM, 20mL) for 30 min. A mixture of ethanol and water (9:1, v/v) was used as solvent, and K_2PdCl_4 was dissolved in deoxygenated water first.

CMC-Stabilized Iron and Iron Oxide Nanoparticles

With carboxymethyl cellulose (CMC) as a stabilizer, iron nanoparticles with small particle size can be synthesized (He and Zhao 2008). Typically, 0.5 g CMC was dissolved in deoxygenated water (100 mL) followed by the addition of $FeCl_2$ solution (0.2 M, 20 mL) with mixing for 15 min. Nitrogen gas was purged to prevent the oxidation of Fe^{2+} in complexes. $NaBH_4$ (0.2 M, 50 mL) was then added into this precursor solution dropwise (5 mL/min), and black iron nanoparticles were formed immediately (Figure 2.4). After reduction, the compressed air was blown in the solution at a flow rate of 40 mL/min. The oxidation time was varied from 15 min to 2 h to form partially and completely oxidized iron. Next, the particles obtained were centrifuged at 20000 rpm and washed with a mixture of deoxygenated water and ethanol twice. Finally, particles were redistributed in ethanol and dried in the oven under nitrogen atmosphere at 90 °C.

2.2.4 Iron Based Nanoparticle Synthesis in Functionalized Membranes

PVDF-PAA-Fe^0

To directly synthesize iron in membrane pores, iron precursors (e.g. Fe^{2+}) were

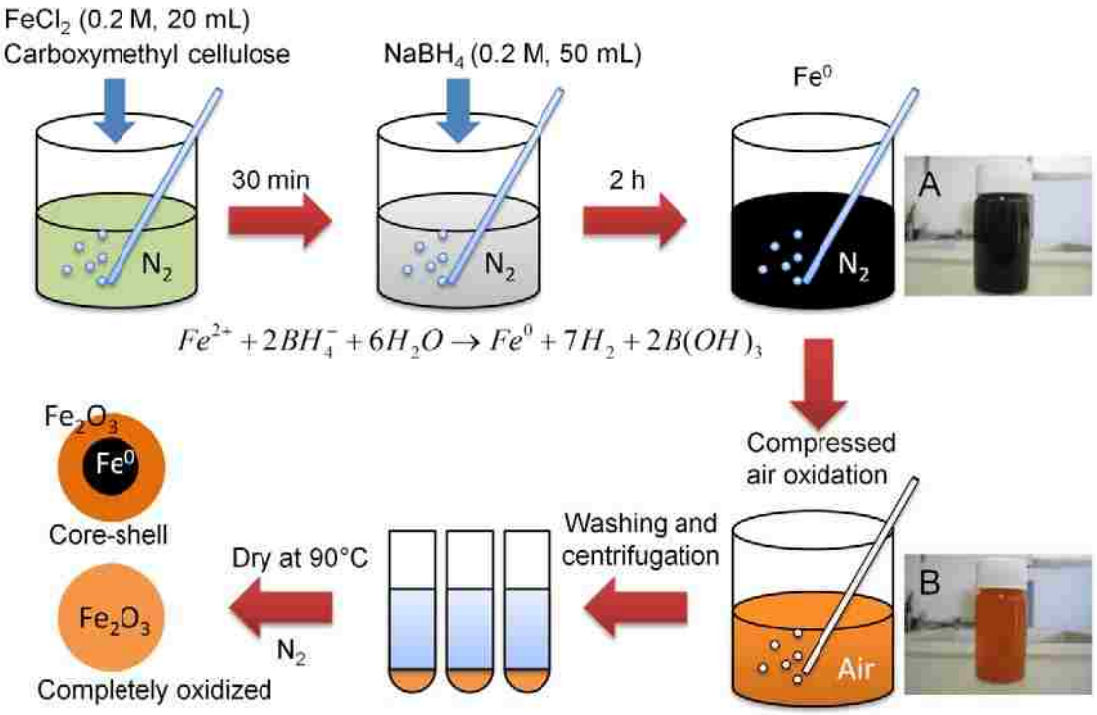

$$Fe^{2+} + 2BH_4^- + 6H_2O \rightarrow Fe^0 + 7H_2 + 2B(OH)_3$$

Figure 2.4. CMC-stabilized iron (A) and iron oxide (B) nanoparticle synthesis

immobilized in functionalized membranes first through two-step ion exchange. PVDF-PAA membranes were preloaded with Na^+ in NaCl solution (50 mM, pH 10-11), followed by a second ion exchange with Fe^{2+} in $FeCl_2$ solution (3.57 mM, pH 5.0-5.2) under an atmosphere of nitrogen. With the addition of $NaBH_4$, Fe^{2+} was reduced to Fe^0, and PAA in the membrane was reloaded with Na^+. The iron loading in membrane pores can be increased by repeated ion exchange and reduction.

PVDF-PAA-Fe/Pd

The post-coating of Pd on iron surfaces was conducted in a mixture of ethanol and water (9:1, v/v) to prevent the oxidation of iron. PVDF-PAA-Fe^0 membranes were soaked in K_2PdCl_4 solution (153 μM, 20mL) with mixing. After 2 h, membranes were rinsed with deoxygenated water, and stored in ethanol.

PVDF-PAA-Iron Oxide

Following the iron formation in PVDF-PAA membranes, the compressed air was purged at a flow rate of 20 mL/min. After 2 h, membranes were rinsed with deoxygenated water, and stored in ethanol.

2.2.5 Dechlorination Experiments

TCE Oxidative Degradation

All experiments were conducted in 20 mL EPA glass vials. Feed pH was adjusted to 6.9±0.1 before the reaction, and measured throughout the reaction. Iron oxide was sonicated for 30 s in DI water (15 mL) before use. TCE (1.08 mM, 5mL) and H_2O_2 (9.75 M, 85 μL) were added in sequence. Sample vials were wrapped with the lightproof paper and shaken at 300 rpm. Two control experiments were conducted to quantify the TCE loss due to volatilization and free radical oxidation via auto-decomposition of H_2O_2.

PCB Reductive Dechlorination

To determine the reactivity of Fe/Pd nanoparticles, 2-chlorobiphenyl (PCB1) was selected as a model compound, and both batch and convective flow experiments were conducted. To make the feed solution, 2-chlorobiphenyl powder was dissolved in deoxygenated water with heating (up to 60 °C) and vigorous stirring for one day. The solution was filtered through regenerated cellulose UF membrane (NMWL=100,000) to remove undissolved powder.

Batch experiments were conducted in 20 mL EPA glass vials. PVDF-PAA membranes (external area: 17.3 cm^2) containing Fe/Pd were soaked in feed solution with mixing at 300 rpm. Convective flow experiments were conducted in the solvent-resistant filtration cell (Sepa ST from GE Osmonics) with a nitrogen gas tank to supply the pressure. The feed solution was permeated through membranes (effective external area: 13.2 cm^2), and reacted with Fe/Pd in membranes. The residence time of 2-chlorobiphenyl can be varied by changing the pressure applied. The adsorption of model compounds in PVDF-PAA membranes was also studied.

Biphenyl Oxidation

The reactivity of membrane supported Fe/Pd (after PCB dechlorination), freshly made iron, and iron oxide nanoparticles with H_2O_2 for free radical generation was studied in batch mode. The same amount of biphenyl (26.5 μM) and H_2O_2 (10 mM) was added in each system, and pH was monitored through the reaction.

2.2.6 Selenium Removal by Iron Functionalized Membranes

Selenium removal was performed with iron nanoparticle suspension and iron functionalized membranes in both batch and convective modes. The effects of total

dissolved solids (TDS) on selenium reduction were studied in different water matrix, including DI water, synthetic water containing salts (e.g. $CaCl_2$, NaCl, Na_2SO_4 and $MgSO_4$) and power plant scrubber water. The scrubber water contained selenium between 0.6 and 1.4 mg/L, while selenium concentrations in DI water and synthetic water were made as 2 mg/L. The batch reaction was conducted in an incubator shaker with mixing (250 rpm). Temperature variation experiment was conducted in the same incubator shaker at 40 °C. In convective mode, feed solution was passed through membranes by applying pressure in cell with compressed nitrogen gas.

2.2.7 Full-scale Functionalized Membrane Module Study

Membranes in module were already functionalized by PAA, and thus can be used for ion exchange directly. To load iron nanoparticles in this module, NaCl solution (50 mM, pH 10) was permeated through the module for 30 min to convert the carboxyl groups in PAA to Na^+ form, followed by permeating $FeCl_2$ solution (3.57 mM, pH 4.9-5.2) through the module. After removing the residual solution from the system, $NaBH_4$ (12 mM) was passed through the membrane module for 15 min. To load more iron, repeated steps of ion exchange and reduction were conducted. To prevent the iron corrosion, the membrane module was stored in Fe^{2+}/ascorbic acid solution (3.57 mM, pH 3.5) after reduction.

2.3 Analytical Methods

2.3.1 Membrane and Nanoparticle Characterization

The hydrodynamic diameters and zeta-potentials of nanoparticles were determined by dynamic light scattering (DLS) and electrophoretic light scattering (ELS)

in Delsa™Nano submicron particle size and zeta potential analyzer, with DI water or ethanol as a solvent.

Brunauer-Emmett-Teller (BET) surface areas of nanoparticles were determined by N_2 adsorption-desorption results obtained in Micromeritics TriStar 3000 surface area and pore size analyzer. The samples were degassed in N_2 overnight at 120 °C before the analysis.

Hitachi S3200 and S4300 Scanning Electron Microscopes (SEM) coupled with an energy dispersive X-ray spectrometer (EDX) were used to study membrane surface and cross-section structure (pore size, porosity and thickness) as well as the aggregated particle size and elemental composition. The membrane cross-sectional samples were prepared via freezing and fracturing the membrane in liquid N_2. All samples were coated with gold and palladium via sputtering.

JEOL 2010F Transmission Electron Microscope (TEM) (accelerating voltage: 200 kV) coupled with an energy dispersive X-ray spectrometer (EDX, Oxford INCA) and an electron energy loss spectroscopy (EELS, Gatan GIF 2000) were utilized to study the morphology and composition of iron related nanoparticles. To understand the phase transformation and composition change on particle surface, line scan and elemental mapping were conducted on iron nanoparticles using either EDS or EELS in scanning TEM (STEM) mode. The crystal structure of iron/iron oxide nanoparticles was studied by using the selected area electron diffraction (SAED).

Mössbauer spectroscopy with ^{57}Co γ-ray source was also conducted to identify the composition of iron/iron oxide. ^{57}Fe spectra were collected over 1024 channels at 22 °C. The powder samples were directly filled in plastic holders with compression,

while the membrane samples were cut and stacked to fit in the same holders. The percentage of each form of iron was determined by peak area ratio after peak fitting.

The composition of membrane top surface was studied with X-ray photoelectron spectroscopy (XPS) (K-Alpha, Thermo-Scientific). Depth profile analysis with ion beam etching was also performed to study PAA functionalization in membrane pores.

X-ray diffraction (XRD) analysis was performed with Cu-Kα (1.5418 Å) radiation using a Bruker-AXS D8 Discovery diffractometer to study the iron oxidation products based on crystal structure change.

Fourier Transform Infrared spectroscopy (FTIR) with attenuated total reflectance (ATR) was used to verify the functional groups on membrane or particle surface. The samples were dried in the vacuum oven at 40 °C before test. Data were collected using 128 scans at a resolution of 4 cm^{-1}.

2.3.2 Chlorinated Organic and Degradation Product Analysis

For TCE analysis, 1, 2-dibromoethane (EDB) was used as an internal standard. EDB was premixed with pentane (1:10000, v/v), which was used for extracting TCE. Samples were extracted (euqi-volume) for 30 min to achieve the equilibrium. TCE concentration was determined by HP 5890 Series II GC-MS with a 60m×0.25mm×14μm film thickness Supelco SPB624 fused silica capillary column. The calibration curve was obtained via plotting the peak area ratios of TCE to EDB with standard concentrations from 0.027 mM to 0.270 mM (R^2=0.997). The average analytical error was less than 7%.

2-Chlorobiphenyl and biphenyl were analyzed by GC-MS (Varian CP3800 GC with DB-5 column and Saturn 2200 MS) with naphthalene-d8 as the internal standard (1:100, v/v). The calibration curve was made up of 12 points from 0.05 mg/L to 10 mg/L

with R^2=0.9999. Samples from reduction experiments were extracted with hexane (equi-volume, 2 h) twice before analysis, including membranes. The samples obtained in biphenyl oxidation were first acidified (pH 2) by sulfuric acid to make all organic acids in their unionized form, followed by extraction with hexane twice (equi-volume, 2 h per extraction). All liquids in hexane phase were combined and concentrated under nitrogen gas flow, followed by the derivatization with N,O-Bis(trimethylsilyl) trifluoroacetamide (BSTFA) and pyridine (1:1 v/v, 200 μL). The efficiency of hexane extraction was 95±3% for 2-chlorobiphenyl and biphenyl, and 90±2 % for hydroxylated biphenyls (2- and 2,2'-dihydroxylbiphenyl).

2.3.3 Metal Content Analysis

Total iron and palladium immobilized in the membranes during the ion exchange and post-coating were quantified via material balance by using a Varian SpectrAA 220 fast sequential atomic absorption spectrometer (AAS). Fe lamp was operated at the wavelength of 386.0 nm and the Pd lamp was at 247.6 nm. The amount of iron immobilized and ion exchange capacity (IEC) of membranes were determined by concentration change during the ion exchange. The results were checked by digesting the reacted membrane in nitric acid (35%) and analyzing the metal concentrations directly. The metal loss due to dissolution was also measured by AAS. The analytical error was less than 2%.

Calcium, magnesium and sodium in scrubber water were diluted and quantified by inductively coupled plasma optical emission spectrometry (ICP-OES, Varian VISTA-PRO) after acidification with 1% nitric acid. The wavelengths selected for analysis were

318.127 nm (Ca), 285.213 nm (Mg), and 568.821 nm (Na), respectively. Yttrium chloride (1 mg/L) was used as the internal standard. The analytical error was less than 1.5%.

2.3.4 Hydrogen Peroxide Analysis

The concentrations of H_2O_2 were determined by a colorimetric method developed by Clapp et al. (Clapp, Evans et al. 1989). Samples were filtered through 0.45 μm PVDF autovial syringeless filters (Whatman), and analyzed by Varian Cary Bio300 UV-Visible absorption spectrophotometer at the wavelength of 407 nm. Titanium oxysulfate was used as an indicator (10 μL/mL sample). The analytical error was less than 3%.

2.3.5 Chloride Analysis

The amount of chloride formed in the oxidation of TCE was measured using an Orion Chloride Electrode (Thermo-Scientific). The calibration curve was obtained by diluting the chloride standard (100 mg/L) with DI water and plotting the electrode potentials E (mV) as a function of $\log[Cl^-]$. Based on the Nernst equation, E has a linear relationship with $\log[Cl^-]$ (R^2=0.994). Sodium nitrate (2 vol%) was added as an ionic strength adjuster (ISA) to ensure that each sample had similar ionic strength. The results were checked by adding an aliquot of chloride standard to the samples. From the values after the addition, the chloride concentrations in original samples could be determined.

2.3.6 Selenium and Scrubber Water Anion Analysis

Selenium concentrations above 50 μg/L were quantified by ICP-OES at the wavelength of 196.026 nm after acidification with 1% nitric acid. Selenium concentrations below 50 μg/L were determined by graphite furnace atomic absorption spectrometer (GFAAS, Varian 880Z) after digesting the samples at 110 °C for 2 h. To reduce the interference of TDS in water, selenium standards were made with synthetic

salt water similar to water matrix in samples. Anions including chloride (0.4 to 200 mg/L), sulfate (0.4 to 200 mg/L), nitrate (0.2 to 100 mg/L as N) and nitrite (0.2 to 100 mg/L as N) were analyzed by DIONEX IC25 ion chromatograph (column: IonPac AS18 4x250 mm) with Na_2CO_3/$NaHCO_3$ buffer solution as mobile phase (1 mL/min, 2000 psi). For scrubber water used in combined nanofiltration and functionalized membrane treatment, selenium speciation analysis was performed by ion chromatography inductively coupled plasma collision reaction cell mass spectrometry (IC-ICP-CRC-MS). Total elemental analyses were performed via inductively coupled plasma dynamic reaction cell mass spectrometry (ICP-DRC-MS) in Applied Speciation and Consulting, WA.

Chapter Three Iron Oxide Nanoparticle Synthesis in Aqueous and Membrane Systems for Oxidative Degradation of Trichloroethylene from Water

In this chapter, the potential for using hydroxyl radical (OH•) reactions catalyzed by carboxymethyl cellulose (CMC) and membrane supported iron oxide nanoparticles to remediate toxic organic compounds was investigated. Iron oxide was synthesized by controlled oxidation of iron prior to their use for contaminant oxidation (by H_2O_2 addition) at near-neutral pH. Cross-linked polyacrylic acid (PAA) functionalized polyvinylidene fluoride (PVDF) microfiltration membranes were prepared by in situ polymerization of acrylic acid in membrane pores. Nanoscale iron and iron oxide (80±20 nm) were directly synthesized in the polymer matrix of functionalized membranes, which prevented the particle aggregation and controlled the particle size. The conversion of iron to iron oxide in aqueous solution with air oxidation was studied based on X-ray diffraction (XRD), Mössbauer spectroscopy, and BET surface area test methods. Trichloroethylene (TCE) was selected as the model contaminant because of its environmental importance. Degradations of TCE and H_2O_2 by iron oxide surface generated OH• were enhanced by nanoscale iron oxide catalysts synthesized in CMC and functionalized membrane support. Iron chelates formed between PAA and dissolved iron also improved the efficiency of H_2O_2 consumption. Depending on the ratio of iron and H_2O_2, TCE conversions as high as 100% (with about 91% dechlorination) was obtained. TCE dechlorination was also achieved in real groundwater samples from superfund site. The graphic abstract of Chapter Three is shown in Figure 3.1.

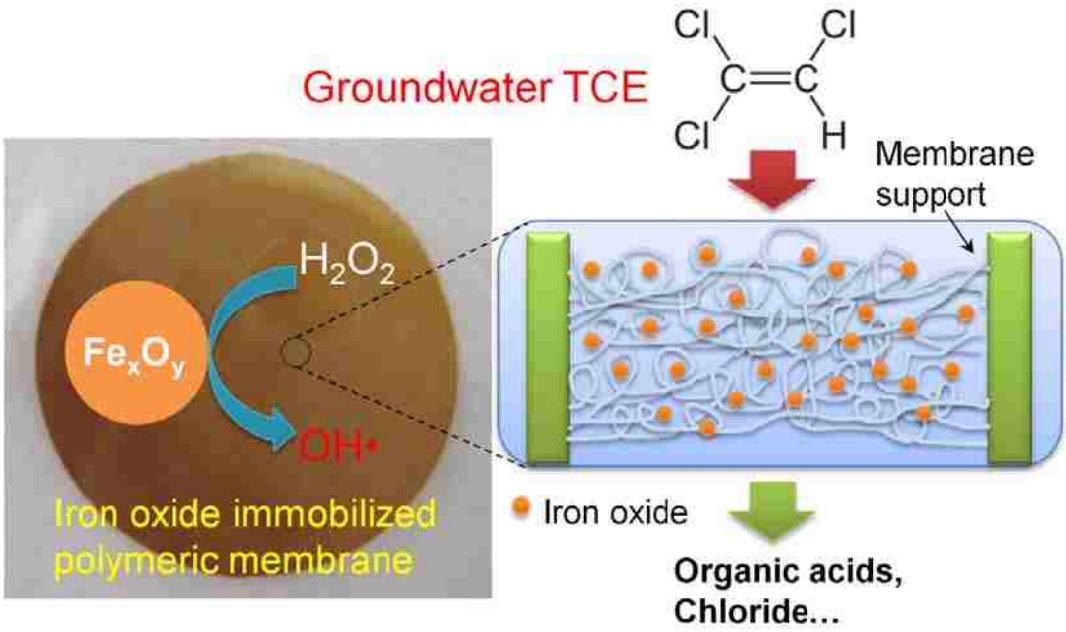

Figure 3.1. Graphic abstract of Chapter Three.

Although iron oxides have been extensively studied as catalysts in heterogeneous Fenton reaction, the efficiency of free radicals is lower than that obtained in the homogeneous reaction. Membrane supported iron oxide prevents the benefits of reducing the particle aggregation, controlling the particle size, and enhance the hydroxyl radical (OH•) generation. This chapter starts with a brief introduction to recent progress on iron oxide based free radical oxidation. This is followed by results and discussion on the performance of stabilized iron oxide in TCE oxidation. Next, it focuses on iron oxide in-situ synthesis in functionalized membranes. The reactivity of membrane supported iron oxide with H_2O_2 towards free radical generation is evaluated, with a highlight on successful TCE degradation in groundwater from a Superfund site in Paducah, KY. Finally, an adsorption-reaction-desorption model is developed to determine the TCE degradation kinetics.

3.1 Introduction

Nanoscale particles have been widely studied in environmental separations and catalytic reactions due to their unique physical and chemical properties (Bell 2003). Their high surface area to volume ratio provides more catalytic sites than bulk particles. In addition, more crystal defects are generated on particles via controlled synthesis, resulting in enhanced reactivity. Iron-based nanoparticles have attracted a growing attention in recent years due to their high reactivity in chlorinated organic dechlorination. TCE and PCBs can be degraded by reductive (Wang and Zhang 1997; Zhang 2003; Xu, Dozier et al. 2005; Savage and Diallo 2005; Tratnyek and Johnson 2006) and/or oxidative pathways (Gates and Siegrist 1995; Pignatello et al. 2006; Laine and Cheng 2007), depending on the state of iron.

In oxidative degradation, heterogeneous Fenton reaction using granular size iron oxides such as goethite, ferrihydrite, hematite and magnetite activated by H_2O_2 has been extensively studied for water remediation (Tyre et al. 1991; Ravikumar and Gurol 1994; Miller and Valentine 1995; Lin and Gurol 1998; Valentine and Wang 1998; Watts et al. 1999; Huang et al. 2001; Yeh et al. 2004; Costa et al. 2008). It takes place on iron oxide surfaces and very little iron is dissolved at near-neutral pH. Hydroxyl radicals (OH•) or ferryl ions (IV) can be formed based on different mechanisms (Keenan and Sedlak 2008). These oxidants further oxidize various recalcitrant organics. A recent study (Voinov et al. 2011) further proved that the free radical production in heterogeneous Fenton reaction was primarily attributed to the surface catalysis of iron oxide instead of the dissolved iron (Fe^{2+} or Fe^{3+}) released by the particles. The catalytic sites were much more effective than dissolved ferric ions in the production of OH•. The catalytic decomposition of H_2O_2 with goethite, ferrihydrite and hematite has similar surface area normalized rate constants (Valentine and Wang 1998; Huang et al. 2001; Kwan and Voelker 2003). Therefore, iron oxide nanomaterials with high specific surface area were employed to promote the production of intermediate oxidants (e.g. OH•) from H_2O_2 decomposition (Ai et al. 2007; Zelmanov and Semiat 2008; Giraldi et al. 2009; Sun and Lemley 2011). To obtain smaller particles, different stabilizers (Peng et al. 2006; Guo et al. 2006; He et al. 2007) and supports can be used in iron oxide synthesis, such as membranes (Xu and Bhattacharyya 2008; Smuleac et al. 2010; Lewis et al. 2011), copolymers (Dhananjeyan et al. 2001), silica (Meeks et al. 2012), and alumina (Lim et al. 2006; Pham, Lee et al. 2009).

The recent development of functionalized membrane provides an opportunity for in-situ catalyst synthesis. Membranes functionalized with ion exchange groups such as

carboxyl groups (Hu and Dickson 2007; Singh et al. 2008) and sulfonyl groups (Wycisk and Pintauro 1996; Wang et al. 1998) have been developed. Iron and Fe/Pd bimetallic nanoparticles were successfully synthesized in PAA functionalized PVDF and polyether sulfone (PES) membranes (Xu, Dozier et al. 2005; Xu and Bhattacharyya 2007; Smuleac et al. 2010). However, the direct oxidative synthesis of iron oxide nanoparticles in polymeric membranes for water treatment has not been explored.

3.2 Properties of CMC-Stabilized Iron Oxide Nanoparticles

The average particle size of CMC-stabilized iron oxide is 30±5 nm (Figure 3.2A). Mössbauer Spectra clearly show iron nanoparticles made in aqueous phase had a core-shell structure (Figure 3.2B), which was formed by a pure iron core and an iron oxide shell (Nurmi et al. 2005). After air oxidation (1 h), iron was completely converted to two-line ferrihydrite (Figure 3.2C). The Fe-B alloy compounds were also formed in borohydride reduction.

With CMC coating on particle surface, the hydrodynamic size of iron oxide increased, resulting in a larger z-average diameter (76 nm) in DLS (Figure 3.3).

The base particle size of iron obtained in high-resolution TEM (HRTEM) images was 10±2 nm with Fast Fourier Transform (FFT) filter treatment (Figure 3.4). After oxidation (1 h), iron oxide exhibited irregular shapes in the form of agglomerate (Figure 3.5A), and the base particle size decreased to 5±2 nm (Figure 3.5D). SAED pattern (Figure 3.5C) shows that iron oxide contained mainly two-line ferrihydrite (Miller indices: 110 and 300; d-spacing: 0.252 nm and 0.151 nm) as well as some magnetite or wüstite (Sun, Li et al. 2006). As expected, the atomic ratio of oxygen and iron (O/Fe) increases from 1.07 (Figure 3.4B) to 1.94 (Figure 3.5B) during the oxidation. The digestion of

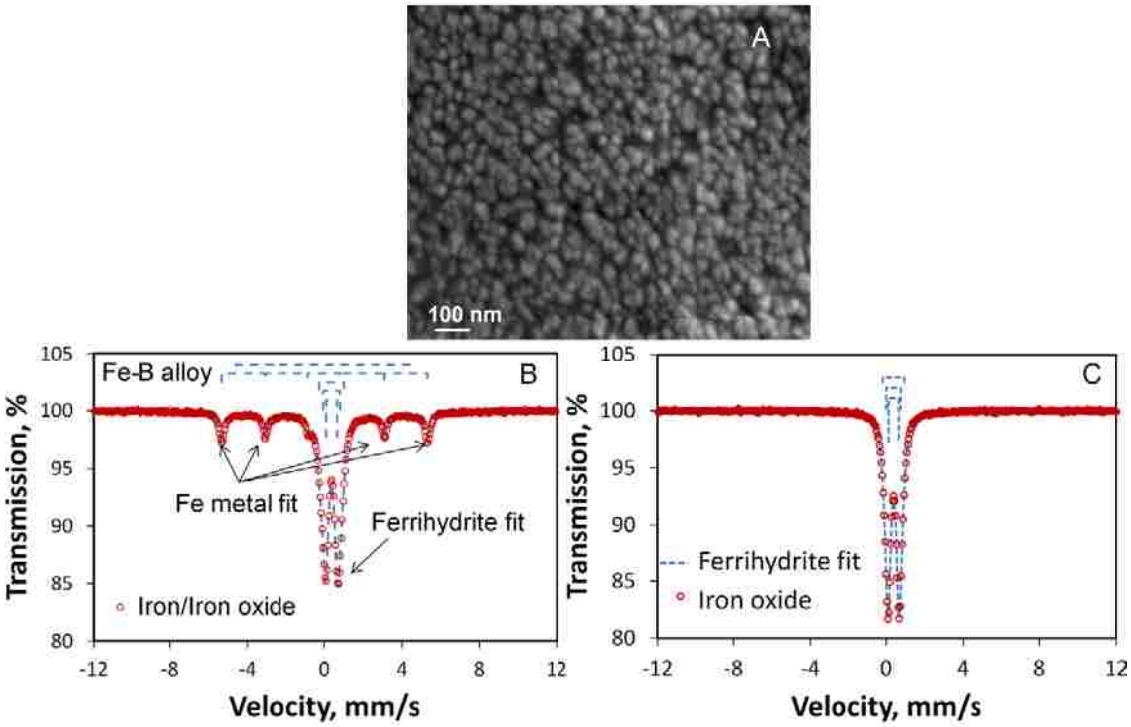

Figure 3.2. SEM and Mössbauer spectra of iron/iron oxide synthesized by air oxidation of iron suspension for 1 h. (A) SEM image of iron oxide; (B) ^{57}Fe Mössbauer spectrum of freshly made iron; (C) ^{57}Fe Mössbauer spectrum of iron oxide.

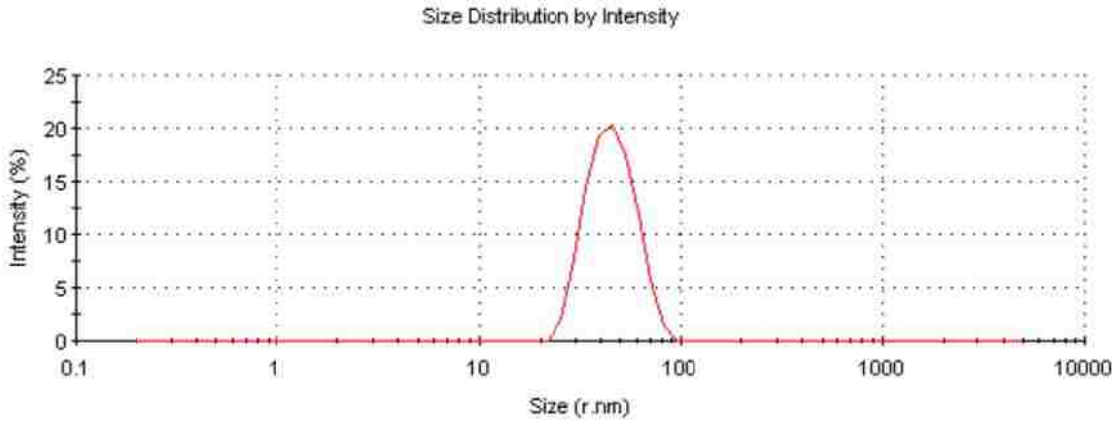

Figure 3.3. Size distribution of iron oxide nanoparticles (synthesized by air oxidation of iron suspension for 1 h). DLS spectrum shows a single peak at the size of 46.19 nm (width: 12.16 nm), and the z-average diameter is 75.33 nm (PDI: 0.323).

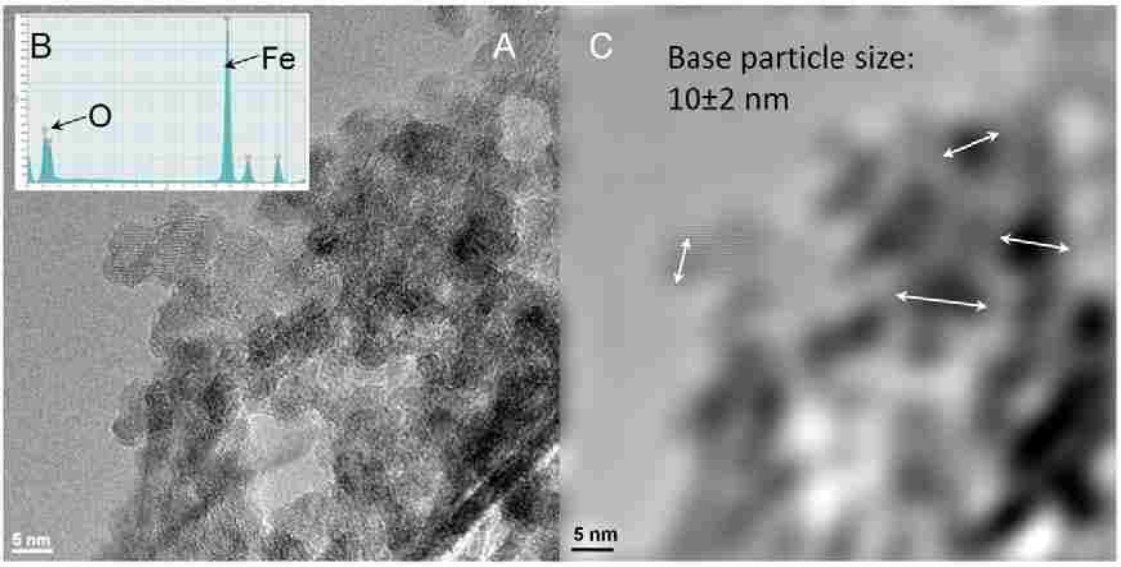

Figure 3.4. HRTEM images of iron nanoparticles before (A) and after (C) FFT filter treatment. EDX result is shown in (B). White arrows show the base iron particles.

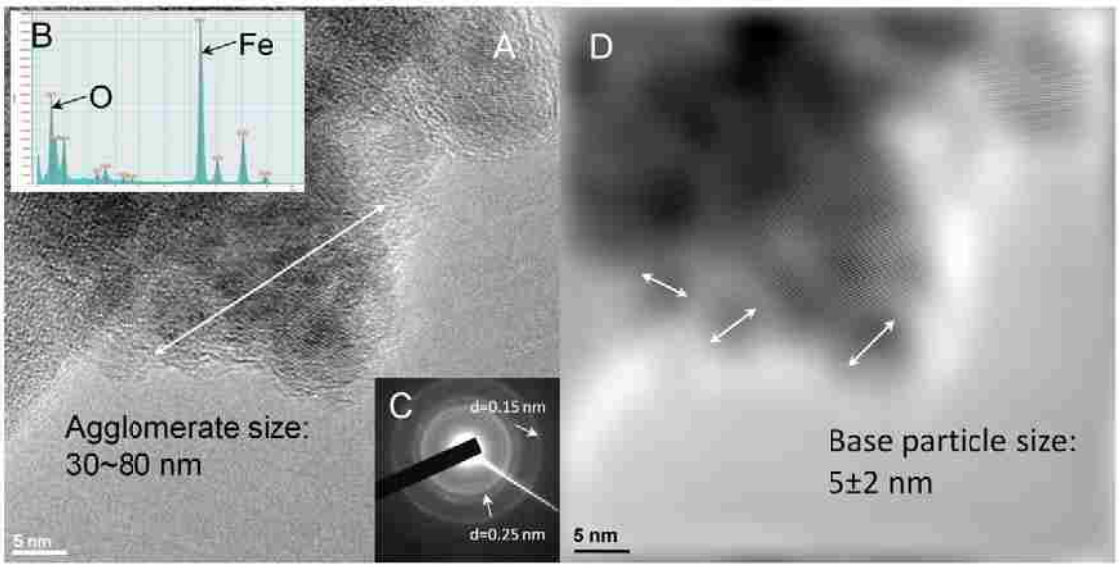

Figure 3.5. HRTEM images of iron oxide nanoparticles (synthesized by air oxidation of iron suspension for 1 h) before (A) and after (D) FFT filter treatment. EDX and SAED pattern results are shown in (B) and (C). White arrows show the agglomerate and base iron oxide particles.

particles shows the iron content in iron oxide was 0.49, suggesting the existence of hydrated iron oxide.

BET surface area of freshly made iron nanoparticles was 37.8 m^2/g. It increased to 253.4 m^2/g after 2 h air oxidation (Figure 3.6). Both iron and iron oxide had the type IV isotherms, showing the formation of porous particles. With the increase of oxidation time, the pore volume also increased while the average pore size decreased (Figure 3.7), resulting in high specific surface area. Those are consistent with the formation of ferrihydrite, which is a naturally existing, highly porous and defective material. The nonporous commercial γ-Fe_2O_3 nanoparticles had a different isotherm (type II) compared to ferrihydrite (Figure 3.6F), and the specific surface area was much smaller (28.4 m^2/g). By controlled oxidation, porous iron oxide nanoparticles were synthesized, which can provide more reactive sites than bulk or nonporous iron oxides for subsequent adsorption and catalysis.

XRD spectra show that the freshly made iron nanoparticles were mainly made of body centered cubic α-Fe crystals, and they were transformed to two-line ferrihydrite via air oxidation (Figure 3.8). Some other iron oxide phases such as lepidocrocite and wüstite were formed as evidenced by new peaks in Figure 3.8d (Furukawa et al. 2002; Hwang et al. 2010). Iron aged for 120 d in a sealed 20 mL vial had both α-Fe and iron oxide characteristic peaks (Figure 3.8e), which originated from its core-shell structure. The particle size calculated from XRD patterns by Scherrer's formula (Cullity and Stock 2001) were 7.8 nm for iron and 3.1 nm for iron oxide, which were consistent with those obtained in TEM.

ATR-FTIR spectrum of CMC-stabilized iron oxide shows that the O-H stretching

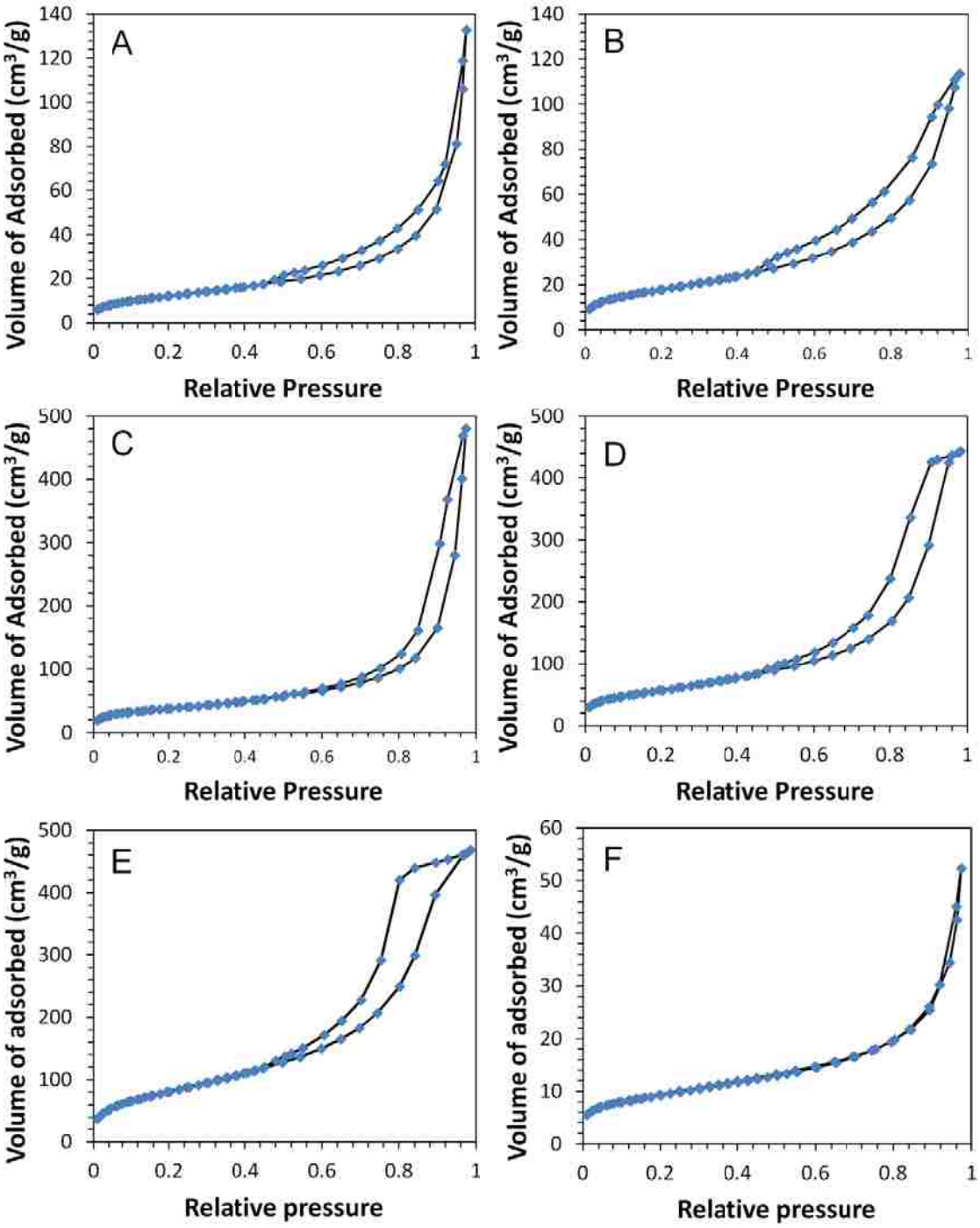

Figure 3.6. N_2 adsorption-desorption isotherms of iron (A), iron oxide synthesized by air oxidation of iron suspension for: (B) 0.25 h, (C) 0.5 h, (D) 1 h, (E) 2 h, and (F) commercial γ-Fe_2O_3. BET surface area (m^2/g): (A) 37.8; (B) 54.9; (C) 117.3; (D)175.5; (E) 253.4; (F): 28.4.

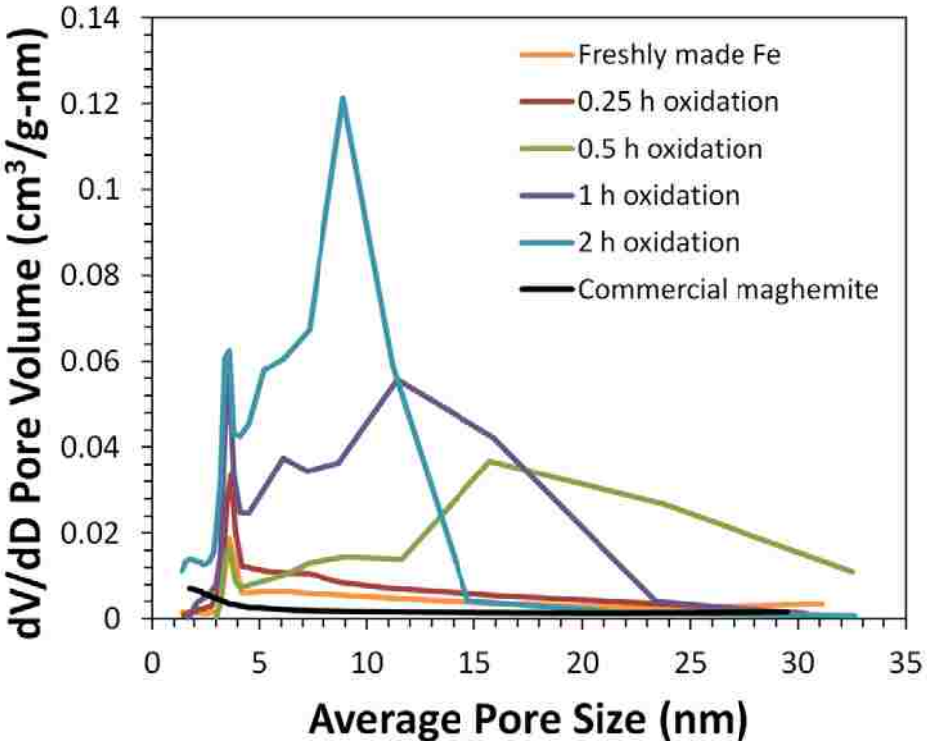

Figure 3.7. Average pore size distribution and pore volume change of iron/iron oxide nanoparticles with air oxidation.

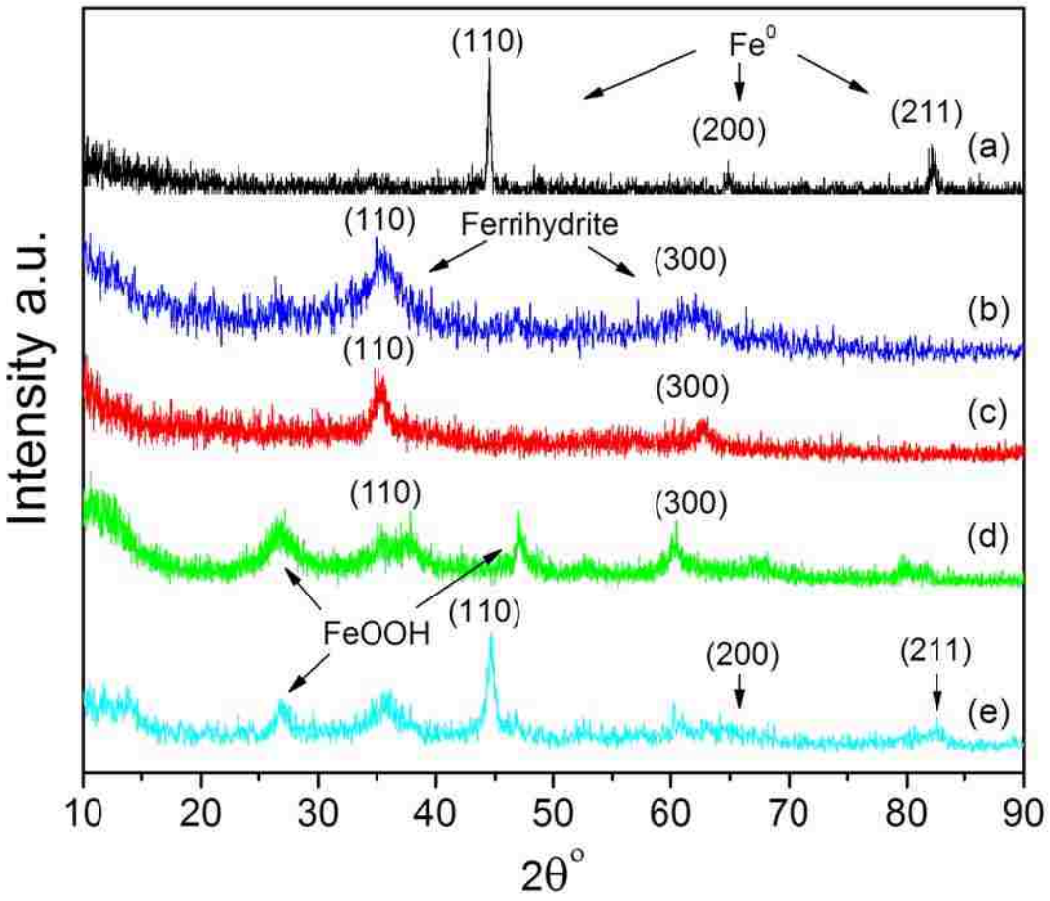

Figure 3.8. XRD spectra of iron (a), iron oxide synthesized by air oxidation of iron suspension for (b) 0.25 h, (c) 0.5 h, (d) 1 h, and aged iron (120 d) (e). The peaks shown in diffraction pattern correspond as following: for (a) and (e), miller indices (110), (200) and (211) of α-Fe (Powder Diffraction File No., PDF#: 00-006-0696); for (b), (c) and (e), miller indices (110) and (300) of two-line ferrihydrite (PDF#: 01-073-8408). For the rest of the peaks, other iron oxides such as lepidocrocite (PDF#: 00-003-0079) and wüstite (PDF#: 00-006-0615).

was shifted significantly, and the asymmetric CH_2 stretching was missing compared to pure CMC (Figure 3.9). Both of them indicate an enhanced intermolecular hydrogen bond was formed between CMC and the particle surfaces (He et al. 2007) to enhance the stability of nanoparticles. The point of zero charge (PZC, pH_{PZC}) of iron was reported to be around 7.80 (Kanel et al. 2005), which suggests the iron surface is positively charged. Therefore, negatively charged CMC can also be adsorbed on iron surface through electrostatic interaction. Zeta-potential results show CMC stabilized iron had a lower PZC than unstabilized one (Figure 3.10). After aging for 120 d, PZC of CMC stabilized iron decreased to 7.05, suggesting the formation of negatively charged materials after oxidation. PZC of natural ferrihydrite is between 5.30 and 7.50 (Schwertmann and Fechter 1982) while the freshly-made and Si-free ferrihydrite is around 7.60 (Saleh and Jones 1984), which is slightly lower than that of iron due to the existing of hydroxyl groups. Therefore, CMC can stay on the particle surfaces during the oxidation.

3.3 H_2O_2 Decomposition with CMC-Stabilized Iron Oxide

The decomposition of H_2O_2 with iron oxide catalysts is highly pH-dependent, and can be described by a modified Haber-Weiss mechanism (Kitajima et al. 1978; Lin and Gurol 1998).

$$\equiv Fe(II) + H_2O_2 \rightarrow \equiv Fe(III) + OH^- + OH\bullet \quad (E3.1)$$

$$\equiv Fe(III) + H_2O_2 \rightarrow \equiv Fe(II) + H^+ + HO_2\bullet \quad (E3.2)$$

$$H_2O_2 + OH\bullet \rightarrow H_2O + HO_2\bullet \quad (E3.3)$$

where ≡Fe(II) and ≡Fe(III) stand for two different valence states on iron oxide surfaces. At the neutral pH, it has been established that H_2O_2 decomposition in the presence of iron oxide can often be approximated by pseudo-first-order reaction.

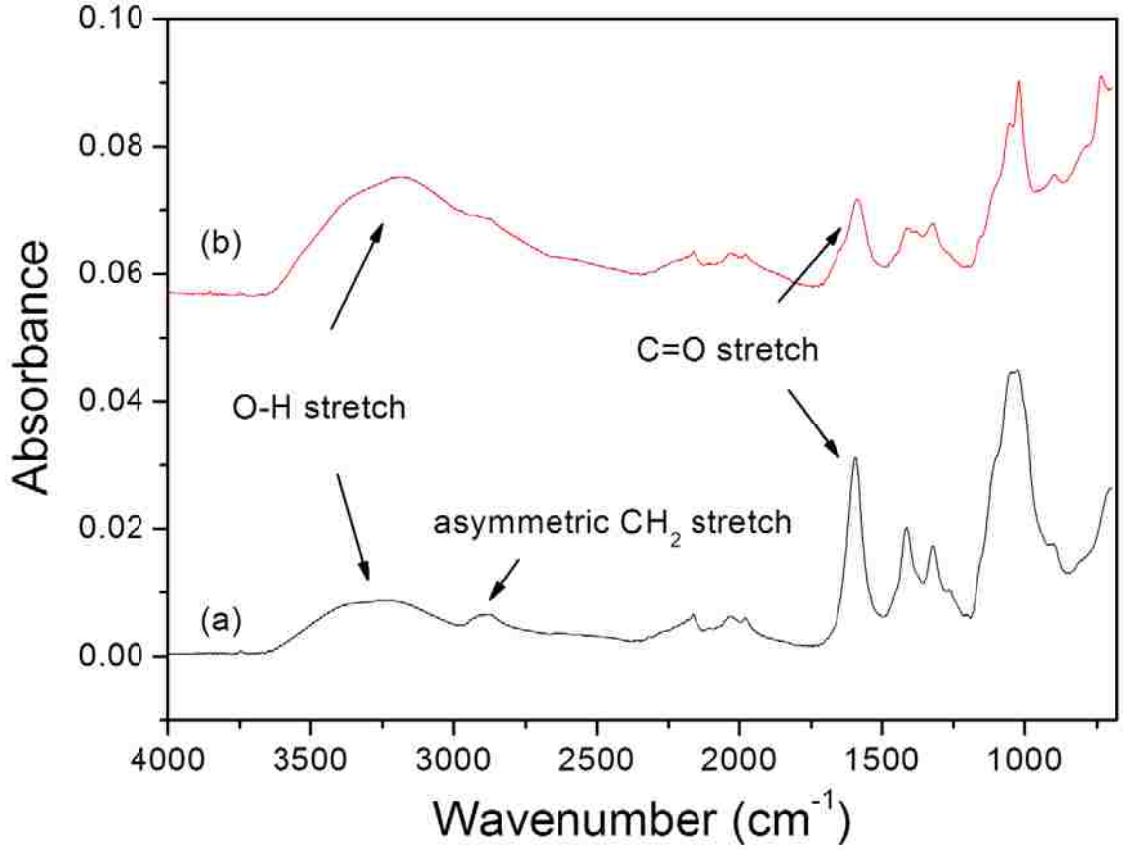

Figure 3.9. ATR-FTIR spectra of (a) CMC and (b) CMC-stabilized iron oxide.

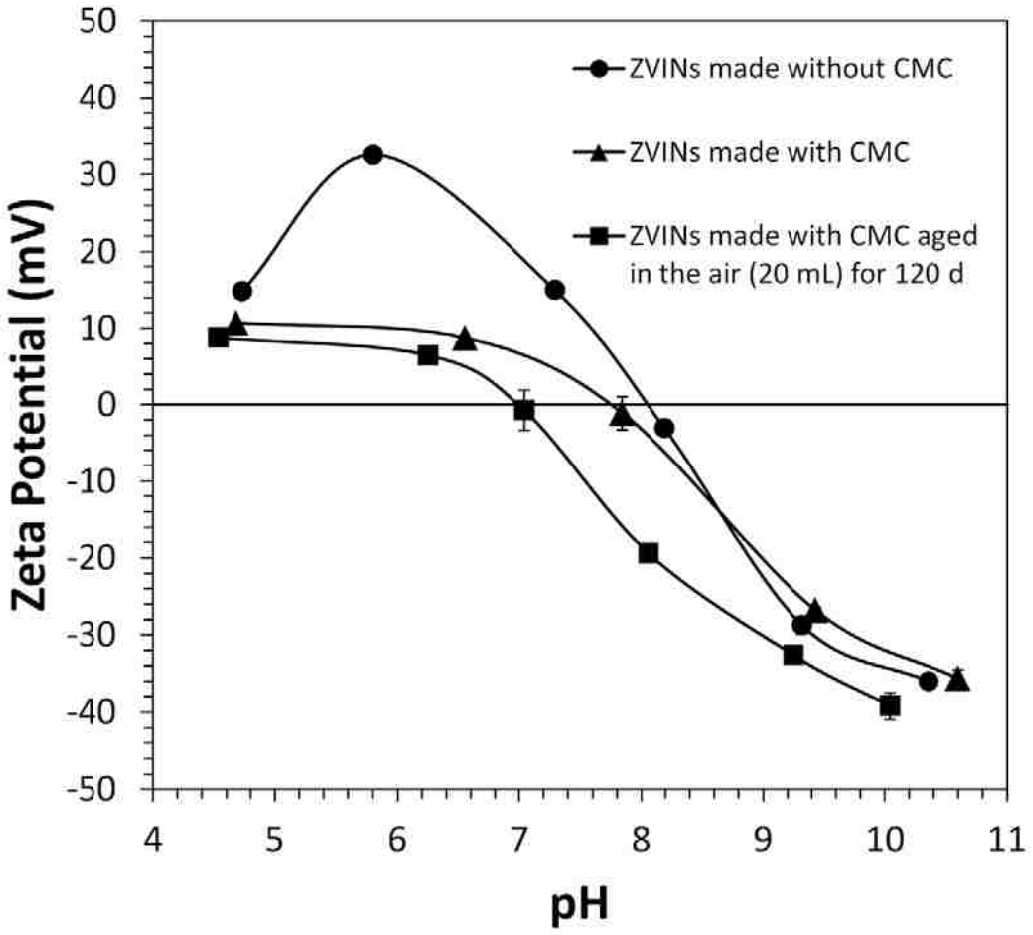

Figure 3.10. Zeta-potentials of iron nanoparticles at pH between 4.0 and 11.0. $[Fe]_0$=0.1 g/L; V=10 mL (deoxygenated water). (●) without CMC; (▲) With CMC; (■) with CMC and aged for 120 d.

$$-\frac{dC_{H_2O_2}}{dt} = k_{obs} C_{H_2O_2} \quad \text{(E3.4)}$$

Where C_{H2O2} is the concentration of H_2O_2 in bulk solution, and k_{obs} is the observed first-order reaction rate for H_2O_2 decomposition. In the absence of TCE, H_2O_2 decomposition with different loadings of iron oxide could fit the pseudo-first-order approximation (Figure 3.11A), with the values of k_{obs} as 0.0170 h^{-1} (0.67 g/L) and 0.0421 h^{-1} (1.33 g/L) for different loadings. k_{obs} is proportional to the specific surface area and loading of iron oxide as well as reaction conditions such as pH and temperature. Therefore, E3.4 can be expanded as

$$-\frac{dC_{H_2O_2}}{dt} = k_{SA} \rho_m a_S C_{H_2O_2} \quad \text{(E3.5)}$$

where a_s is the specific surface area of particles, ρ_m is the loading in the system, and k_{SA} is the surface-area-normalized rate for H_2O_2 decomposition. As expected, k_{SA} values obtained for two different iron oxide loadings (1.46×10^{-4} L/(h·m^2) and 1.80×10^{-4} L/(h·m^2)) were almost identical. This shows that iron oxide catalyzed H_2O_2 decomposition is a surface-initiated reaction, and a high specific surface area will result in high reactivity. The dissolved iron concentration was less than 60 μM. Control experiments show that less than 2% H_2O_2 was lost via auto-decomposition.

3.4 TCE Oxidation with Iron Oxide/H_2O_2

TCE (0.27 mM) oxidative degradation was conducted in iron oxide (1.33 g/L)/H_2O_2 (41.4 mM) system. TCE conversion was 98.3% after 24 h reaction, with the consumption of H_2O_2 around 83.7% (Figure 3.11). The solution pH decreased to 4.60 from 6.95. TCE degradation rate was not affected as its concentration decreased, which is consistent with the previous report of phenol oxidation (Miller and Valentine 1999; Pham,

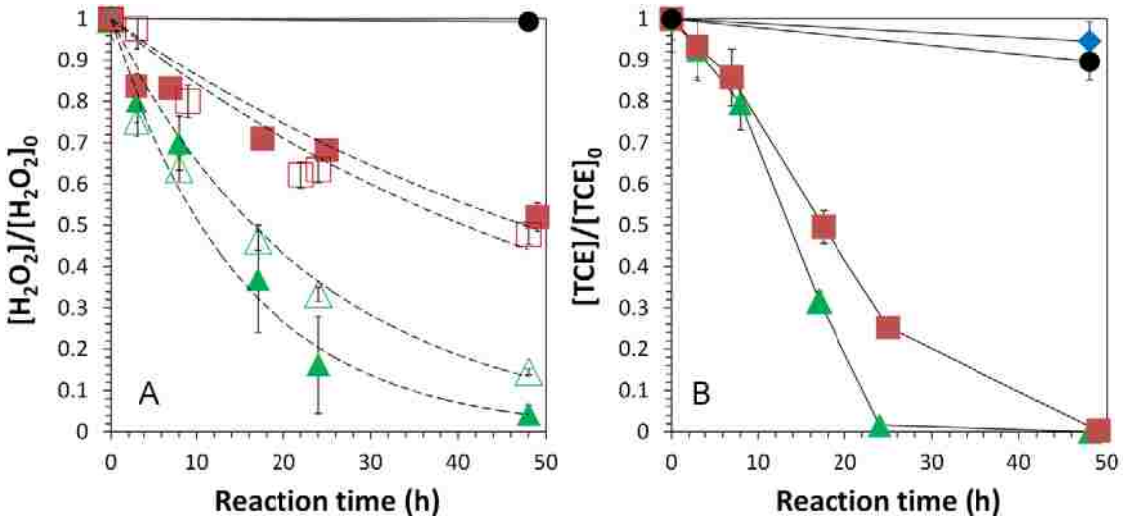

Figure 3.11. TCE and H_2O_2 degradation in the iron oxide/H_2O_2 system. (A) The decomposition of H_2O_2 in the absence (hollow symbols) and presence (solid symbols) of TCE, and the pseudo-first-order approximation by E3.4 (dashed lines); (B) TCE oxidation with iron oxide nanoparticles (synthesized by air oxidation of iron for 1 h). $[TCE]_0$=0.27 mM; $[H_2O_2]_0$=41.4 mM; V=20 mL. pH=6.95 at t=0 and pH=4.60 at t=48 h. (▲) [Iron oxide]=1.33 g/L; (■) [Iron oxide]=0.67 g/L; (◆) Control (no H_2O_2 added); (●) Control (no iron oxide added); (△) [Iron oxide]=1.33 g/L; (□) [Iron oxide]=0.67 g/L.

Lee et al. 2009). The control group shows that less than 6% TCE was lost due to the volatilization. TCE loss due to H_2O_2 auto-decomposition could be neglected. Those results show that the reactive oxidants (e.g. OH•) were indeed formed in this system.

Generally, TCE oxidation by OH• forms chloroacetic acids, which are further oxidized to generate the hydrochloric acid, formic acid and carbon dioxide (Watts and Teel 2005; Huling and Pivetz 2006; Pignatello et al. 2006; Li, Stefan et al. 2007; Lewis, Lynch et al. 2009). Chlorine atoms are removed during the free radical oxidation. Three moles of chloride will be formed in the complete oxidation of one mole of TCE. The chloride yield ($[Cl^-]_{obtained}/[Cl^-]_{max}$) in TCE oxidation was 80.7% after 24 h, and 91.5% after 48 h (Figure 3.12). As each mole of TCE was oxidized, 2.74 moles of chloride was obtained. Chloride concentration changed faster than TCE concentration, and their ratio increased with reaction time (Figure 3.13). It could be explained by the formation of chlorinated intermediates in the initial period of TCE oxidation, followed by continuous release of chloride from those intermediates.

When iron oxide loading was halved (0.67 g/L), TCE conversion was 74.7% after 24 h (Figure 3.11). The total consumption of H_2O_2 was reduced by 45.6%. The chloride yield was 80.5% after 24 h, and 83.2% after 48 h. Therefore, as each mole of TCE was degraded, 2.50 moles of Cl^- was obtained in solution. H_2O_2 decomposition was nearly unaffected in the presence of TCE.

3.5 H_2O_2 Efficiency of Heterogeneous Fenton Reaction

The efficiency of H_2O_2 consumption in TCE oxidation can be defined as the amount of TCE degraded per mole of H_2O_2 consumed.

$$E = \frac{\Delta[TCE]}{\Delta[H_2O_2]} \times 100\% \qquad \text{(E3.6)}$$

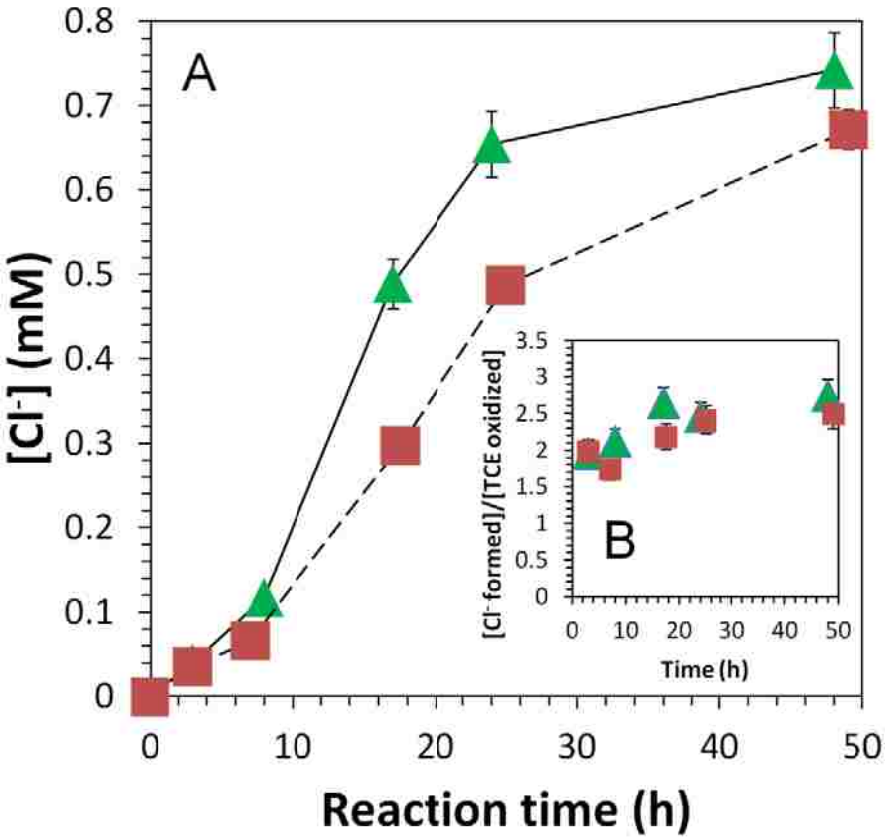

Figure 3.12. Chloride formation in iron oxide/H_2O_2 system. (A) Chloride concentrations; (B) Cl^- formed per TCE degraded or (mmol Cl^- formed)/(mmol TCE degraded). $[TCE]_0$=0.27 mM; $[H_2O_2]_0$=41.4 mM; V=20 mL. pH=6.95 at t=0 and pH=4.6 at t=48 h. $([Cl^- \text{ formed}]/[\text{TCE oxidized}])_{max}$=3 (When TCE is completely degraded). (▲) [Iron oxide]=1.33 g/L; (■) [Iron oxide]=0.67 g/L.

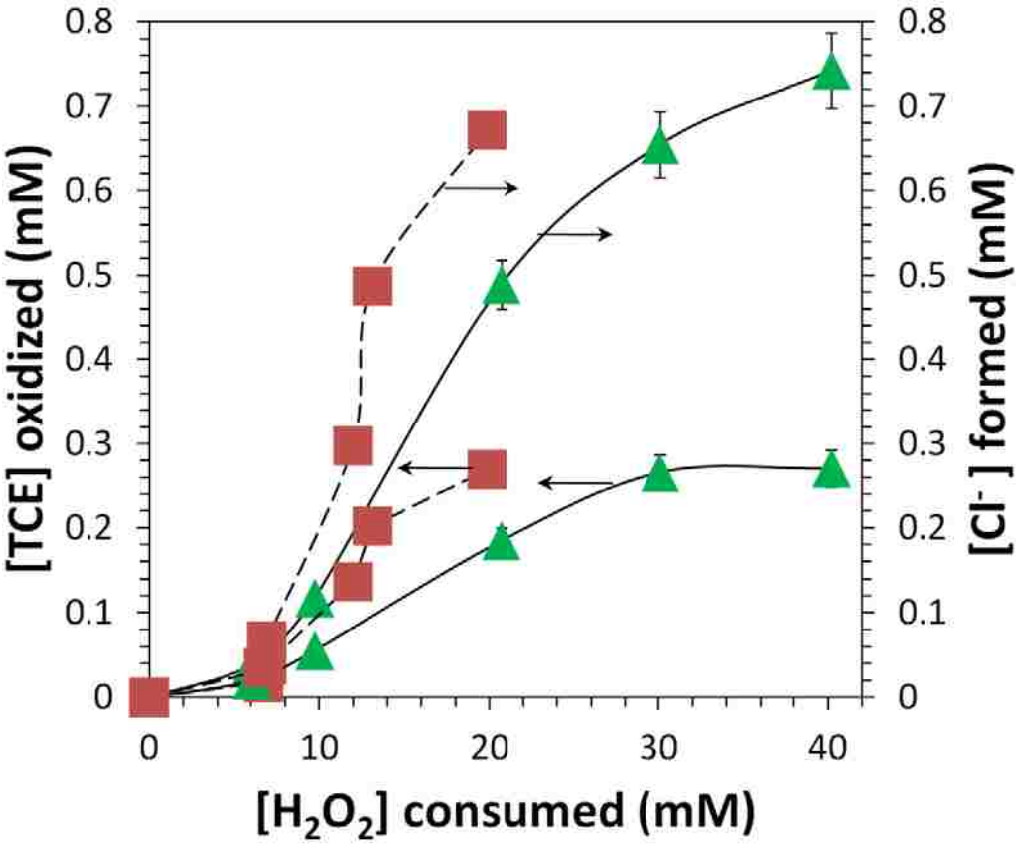

Figure 3.13. TCE degradation and chloride formation with H_2O_2 consumption in iron oxide/H_2O_2 system. $[TCE]_0$=0.27 mM; $[H_2O_2]_0$=41.4 mM; V=20 mL. pH=6.95 at t=0 and pH=4.6 at t=48 h. $[Cl^-$ formed$]_{max}$=0.810 mM). (▲) [Iron oxide]=1.33 g/L; (■) [Iron oxide]=0.67 g/L.

This efficiency was reported to be below 0.1% in the oxidation of phenol (Pham, Doyle et al. 2012), and between 0.19% and 0.95% in the oxidation of quinoline with unstabilized iron oxides at the near neutral pH (Valentine and Wang 1998), depending on the reactivity of model compounds and the ratio of those compounds to H_2O_2 in the system. Low efficiency was mainly attributed to the conversion of H_2O_2 to oxygen and water based on a non-radical electron transfer mechanism as well as the free radical scavenging by iron oxide surfaces (Lee et al. 2001; Pham, Lee et al. 2009; Xue et al. 2009). The formation of ferryl ions (IV) could result in a lower production of OH•. Ferryl ions are less reactive than OH•, and may unable to oxidize the recalcitrant organics such as TCE. Alternatively, OH• could be partially quenched by H_2O_2 or other free radicals. It should be noted that those parallel reactions have the rates slightly lower or in the same order of magnitude as that of TCE with OH• ($k=4\times10^9$ $M^{-1}s^{-1}$). E was 1.21±0.19% for CMC-stabilized iron oxide nanoparticles (0.67 g/L). A higher catalyst loading (1.33 g/L) gave a lower efficiency due to the scavenging of free radicals on iron oxide surfaces (Figure 3.13).

3.6 Reuse of Iron Oxide Nanoparticles

After the first use, the particles were washed with deoxygenated water and ethanol, and dried in the oven under nitrogen atmosphere at 90 °C. They were reused in TCE oxidation after sonication (1.33 g/L) with the same amount of TCE (0.27 mM) and H_2O_2 (41.4 mM). TCE conversion was 98.0% after 24 h, while the consumption of H_2O_2 increased to 99.7%. Therefore, the efficiency of H_2O_2 consumption went down to 0.74±0.09%. The chloride yield was 73.9% (i.e. 2.22 moles of Cl^- were obtained as each mole of TCE was oxidized). In this surface-catalyzed reaction, iron oxide exists in the forms of ≡Fe(II) and ≡Fe(III), which were interconverted by reacting with H_2O_2. Iron

hydroxides are formed due to the precipitation of Fe^{2+}/Fe^{3+} released from particle surfaces. The composition of iron oxide has been changing through this catalytic reaction, and it will affect the specific surface area of iron oxide and its reactive sites. This is indeed the case, since BET surface area of iron oxide decreased from 175.5 m^2/g to 142.0 m^2/g after TCE oxidation. Iron oxide could also agglomerate due to the degradation of CMC coating with free radicals. Therefore, the change of particle size and composition was attributed to the decline of oxidation efficiency.

3.7 Properties of Functionalzied Membrane Supported Iron Oxide Nanoparticles

PVDF microfiltration membranes were used as a support here due to its excellent thermal stability and solvent resistance. When PVDF was functionalized by in situ polymerization of acrylic acid, cross-linked PAA was formed inside the membrane pores. The cross-linker (i.e. ethylene glycol) reacted with carboxyl groups on PAA, forming the ester bonds. The free carboxyl groups captured the dissolved ferrous ions via ion exchange (Figure 3.14). To prevent the pH drop during the direct iron capture, functionalized membranes were preloaded with Na^+, followed by ion exchange with Fe^{2+}. Both AAS and ICP-OES results show great material balance (Table 3.1). The atomic ratio of Na^+ released from the membrane over Fe^{2+} bound to the membranes was 1.9 ± 0.05, close to the maximum ratio 2. Nitric acid digestion further proves that iron picked up by PAA was completely converted into iron/iron oxide.

SEM images show that iron oxide was also formed on the membrane top surface due to the formation of PAA there in dip-coating process. The resulting particles agglomerated with each other (Figure 3.15A), compared to uniformly distributed particles in membrane pores (Figure 3.15B). This shows that the entangled PAA network indeed

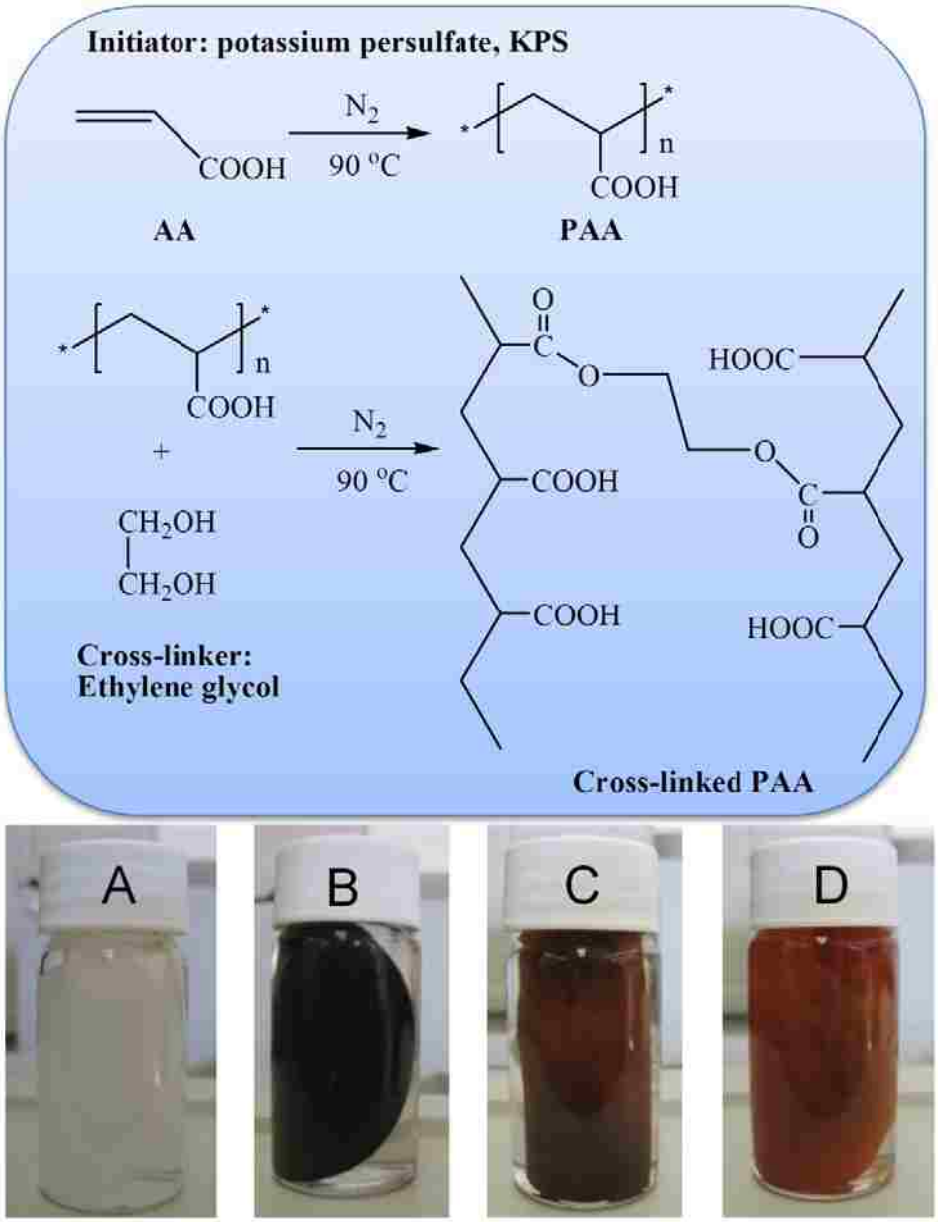

Figure 3.14. Cross-linked PAA synthesis with ethylene glycol as the cross-linker and pictures of functionalized membranes during nanoparticle synthesis. (A) PVDF-PAA; (B) PVDF-PAA-Fe^0; (C) PVDF-PAA-iron oxide synthesized by air oxidation of (B) for 1 h; (D) PVDF-PAA-iron oxide after reacting with H_2O_2 (48 h).

Table 3.1. Iron capture and sodium release by PVDF-PAA membranes during the ion exchange. The concentrations of metal ions were measured by atomic absorption spectrometer (AAS) and inductively coupled plasma atomic emission spectroscopy (ICP-OES).

	AAS	ICP-OES	
	Fe: 386 nm	Fe: 238.204 nm	Na: 568.821 nm
Metal concentration before ion exchange (mM)	3.480	3.700	0.037
Metal concentration after ion exchange (mM)	2.810	3.021	1.353
Metal in PVDF-PAA by mass balance (mmol)	0.134	0.136	0.263
Atomic ratio (Na/Fe)		1.937	
Blank nitric acid (35 wt%) (mM)	0	0.018	0.136
Digested metal in nitric acid (35 wt%) (mM)	3.340	3.461	6.657
Metal in PVDF-PAA by digestion (mmol)	0.134	0.138	0.261
Atomic ratio (Na/Fe)		1.894	

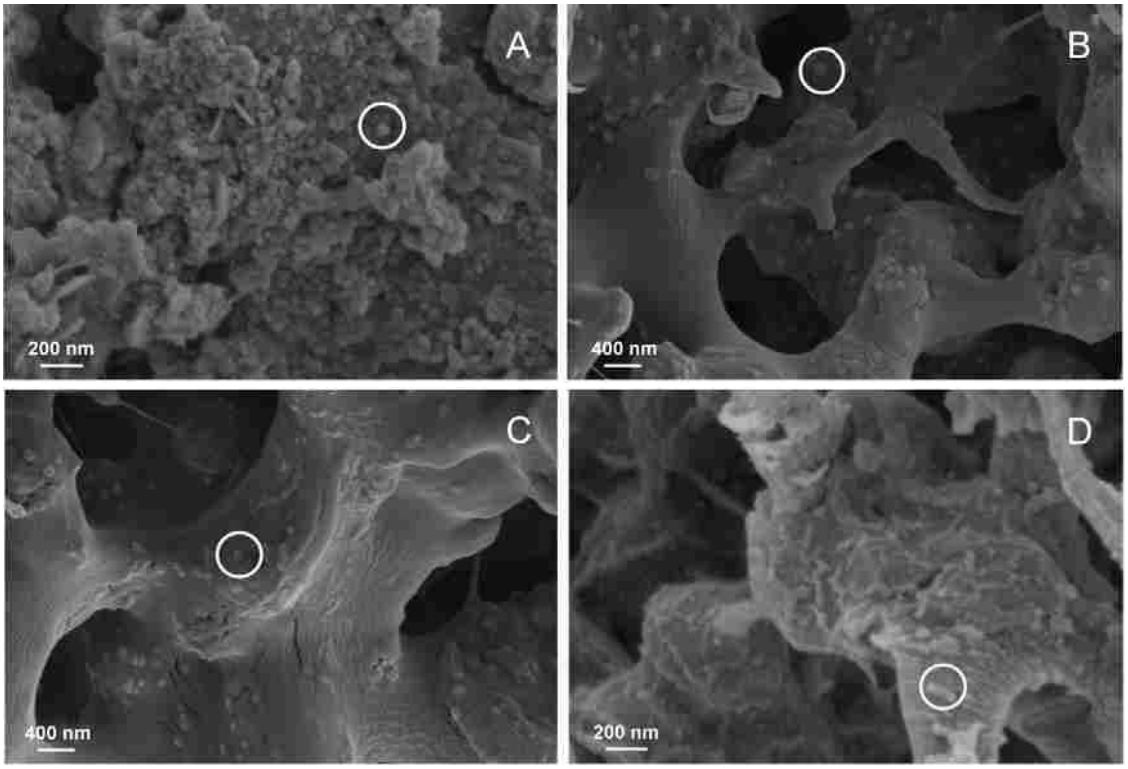

Figure 3.15. SEM images of iron and iron oxide functionalized membranes: (A) iron on membrane top surface; (B) iron in membrane pores (cross section); (C) iron oxide in membrane pores (cross section); (D) iron oxide after reacting with H_2O_2 (48 h, cross section). White circles highlight the particles.

prevented the particle aggregation. The iron oxide particle size after 1 h air oxidation was 80±20 nm (Figure 3.15C). However, the near-spherical iron oxide was transformed into nano-aggregates after reacting with H_2O_2 (Figure 3.15D). It could be explained by the formation of iron hydroxide precipitates from the dissolved iron.

ATR-FTIR spectra of PVDF-PAA membranes show the C=O bond stretching in carboxyl groups at 1710 cm^{-1} compared to pristine PVDF membranes (Figure 3.16). This proves the successful functionalized of PVDF membranes. When iron oxide was immobilized in functionalized membranes, this peak shifted to 1560 cm^{-1} due to the interaction of carboxyl groups with particle surfaces. The strong C-F bond stretching from PVDF has been shown at 1000-1360 cm^{-1}, and didn't shift during the in-situ polymerization and particle synthesis. It again shows that PVDF is a stable supporting material.

3.8 TCE Oxidation in PVDF-PAA-Iron oxide/H_2O_2 system

TCE (0.27 mM) oxidation was conducted in functionalized membrane system through activation of H_2O_2 (41.4 mM). Iron oxide loading in the membrane was 0.88 g/L as iron. After 48 h, TCE concentration decreased by 74.7% (Figure 3.17). The conversion of H_2O_2 was 86.6% after 24 h, and 96.7% after 48 h. H_2O_2 decomposition could be fit in pseudo-first-order reaction law with k_{obs}=0.0842 h^{-1}. The chloride yield was 40.9%, and the ratio of [Cl^- formed] to [TCE degraded] was 1.23 (Figure 3.18). The concentration changes of TCE and chloride with H_2O_2 consumption were almost identical (Figure 3.19). The ion exchange capacity of functionalized membrane makes it as a buffer during TCE oxidation, and the solution pH only decreased from 7.0 to 6.8 after 48 h. Less than 20 μM of iron was dissolved in the reaction. Without the pH drop, the rate of TCE degradation

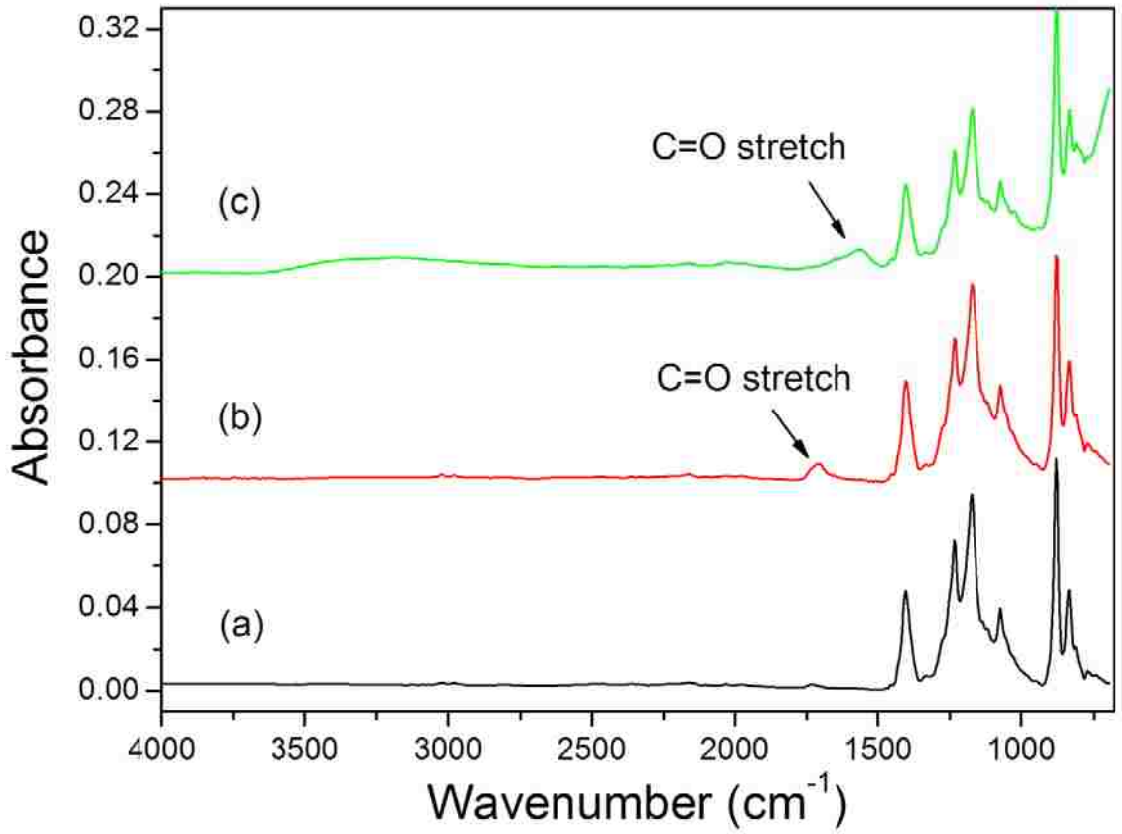

Figure 3.16. ATR-FTIR spectra of (a) pristine hydrophilized PVDF membrane (EMD Millipore DVPP14250), (b) PAA functionalized PVDF membrane, and (c) PVDF-PAA-iron oxide membrane.

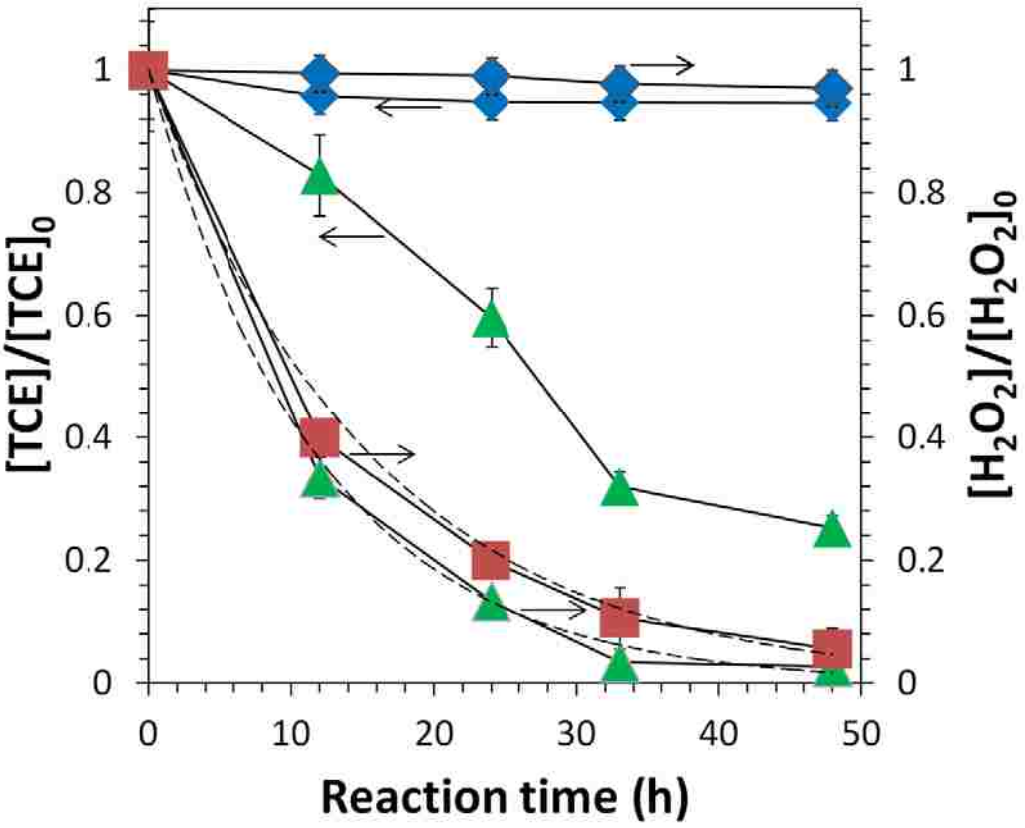

Figure 3.17. TCE and H_2O_2 degradation in PVDF-PAA-iron oxide membrane system (solid line). Dash lines show the pseudo-first-order model fit of H_2O_2 decomposition (E3.4). $[Fe]_0$=0.88 g/L as iron oxide; $[TCE]_0$=0.27 mM; $[H_2O_2]_0$=41.4 mM; V=20 mL. pH=7.0 at t=0 and pH=6.8 at t=48 h. (▲) PVDF-PAA-iron oxide; (◆) Control (PVDF-PAA); (■) Control (no TCE added). TCE was partially extracted by PVDF-PAA membrane during the reaction (14.8% after 48 h). The data used in this figure has been modified.

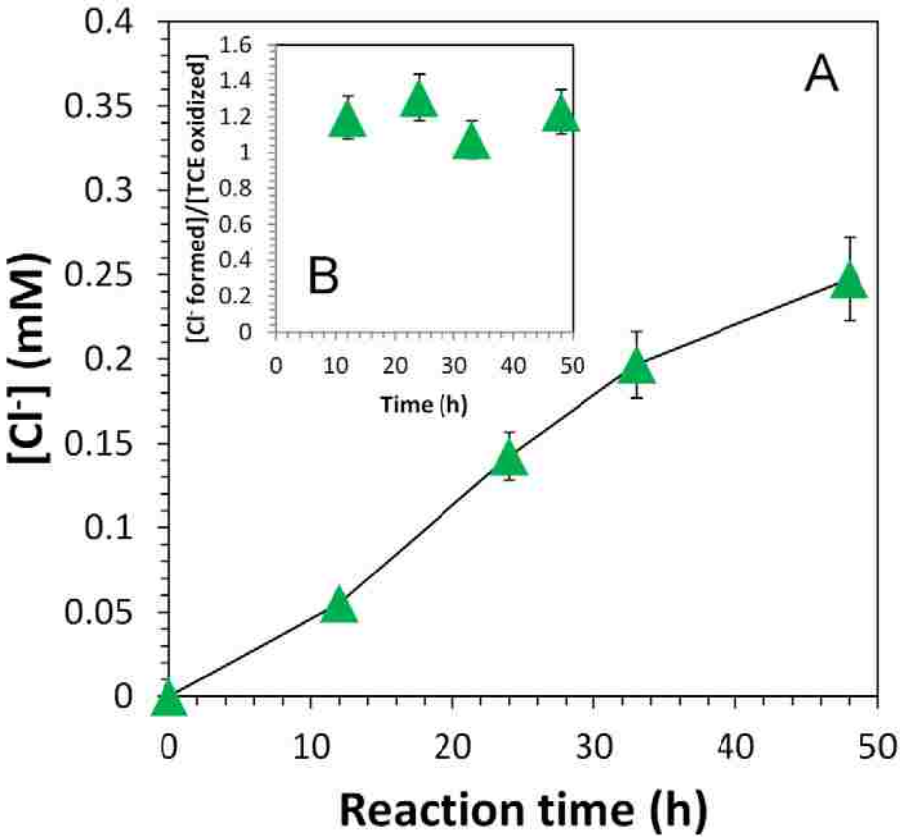

Figure 3.18. Chloride formation in PVDF-PAA-iron oxide membrane system. (A) Chloride concentration (mM); (B) Cl^- formed per TCE degraded or (mmol Cl^- formed)/(mmol TCE degraded). $[Fe]_0$=0.88 g/L as iron oxide; $[TCE]_0$=0.27 mM; $[H_2O_2]_0$=41.4 mM; V=20 mL. pH=7.0 at t=0 and pH=6.8 at t=48 h. ($[Cl^-$ formed]/[TCE oxidized])$_{max}$=3.

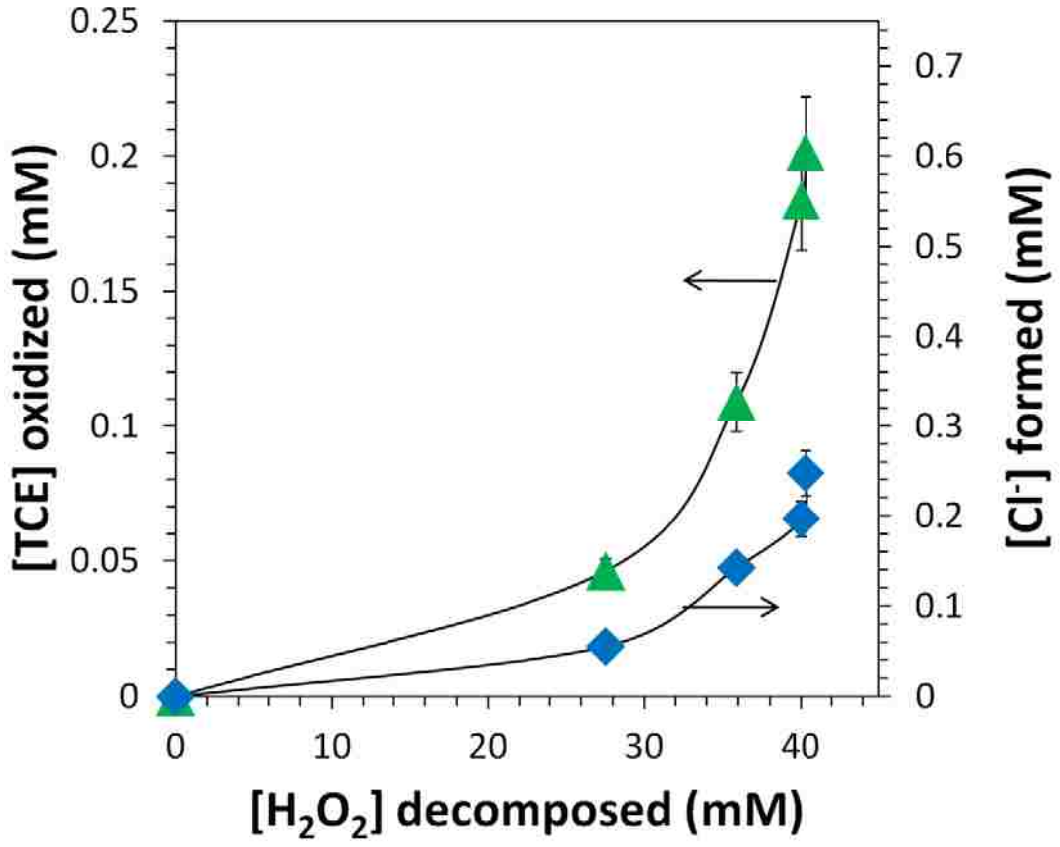

Figure 3.19. TCE degradation and chloride formation with H_2O_2 consumption in PVDF-PAA-iron oxide membrane system. $[Fe]_0$=0.88 g/L as iron oxide; $[TCE]_0$=0.27 mM; $[H_2O_2]_0$=41.4 mM; V=20 mL. pH=7.0 at t=0 and pH=6.8 at t=48 h. $[Cl^-\ formed]_{max}$=0.81 mM.

was slower, and some chlorinated intermediates might not release the chloride completely. Some chloride could also be adsorbed in the polymer matrix. The efficiency of H_2O_2 consumption was 0.36±0.08%, which was much higher than that obtained with unstabilized iron oxide catalysts (Pham, Lee et al. 2009). TCE was partially extracted (up to 14.8%) by PVDF-PAA membranes.

3.9 Reuse of Membranes

After reaction, membranes were washed with deoxygenated water, and dried in vacuum oven for a second use. The same amount of TCE and H_2O_2 was used. After 48 h, TCE conversion was 60.4%, and H_2O_2 consumption increased to 98.4%. The chloride yield was 38.9%. The efficiency of H_2O_2 consumption went down to 0.32±0.07%.

3.10 Real Groundwater Study with PVDF-PAA-Iron oxide

To demonstrate that membrane supported iron oxide could be used in the chloro-organic treatment in groundwater, a batch experiment was conducted using the real groundwater taken from Paducah Gaseous Diffusion Plant Superfund Site in Western Kentucky. It should be noted that this water contains a small amount of Fe^{2+}/Fe^{3+} (5.36 μM), Ca^{2+} (600 μM) and Cl^- (1.55 mM) with pH at 7.4. After 33 h, TCE conversion was 53.5% with H_2O_2 consumption as 93.4%. The chloride yield was 66.7%, and the efficiency of H_2O_2 consumption was 0.22±0.07%. Iron oxide loading in this system was lower (0.435 g/L as iron), which explained the lower TCE conversion than that obtained in DI water. The groundwater may also contain the free radical scavengers such as carbonate, bicarbonate and other chloro-organics with less chlorine atoms, which reduced the oxidation efficiency, but resulted in a higher chloride yield.

3.11 Benefits of Functionalized Membrane Platform

Both CMC-stabilized and membrane supported iron oxide show the promising reactivity in groundwater remediation. Nonaggregated particles with uniform size were obtained. Complete degradation of TCE was achieved via the continuous addition of H_2O_2. However, CMC coating was not stable in free radical oxidation, and could detach from particle surfaces. The cleanup of dissolved CMC will require extra separation steps. Although PAA is also soluble in water, the addition of cross-linker creates an entangled polymer network, which has an enhanced stability. The functionalized membrane can also retain the dissolved metal ions via carboxyl groups in PAA, and maintain the solution pH as a buffer. After iron oxide synthesis, the functionalized membrane still had the ion exchange capacity due to the existence of carboxyl groups. However, as the amount of immobilized particle increased, the diffusivity of ferrous ions from the bulk phase to membrane pore area would become more difficult, especially for a dense membrane with small pore size. The ion exchange capacity of membrane would decline, and this was indeed the case (Figure 3.20).

3.12 Reaction Mechanism and Modeling

The oxidative degradation of TCE is attributed to the highly reactive OH•, and an adsorption-desorption effect of reactants on iron oxide surfaces (Pignatello et al. 2006). The first step in TCE oxidation was considered as the fast addition of OH• to the double bond of TCE (Li, Stefan et al. 2007). It produces the intermediates which are further oxidized into organic acids and chloride by OH•. The adsorption of TCE on iron oxide surface is critical, since the free radicals may only appear and react with the contaminants near the reactive surfaces where they are generated (Huling and Pivetz 2006). Xue et al reported the adsorption and oxidation of pentachlorophenol (PCP) on the surface of

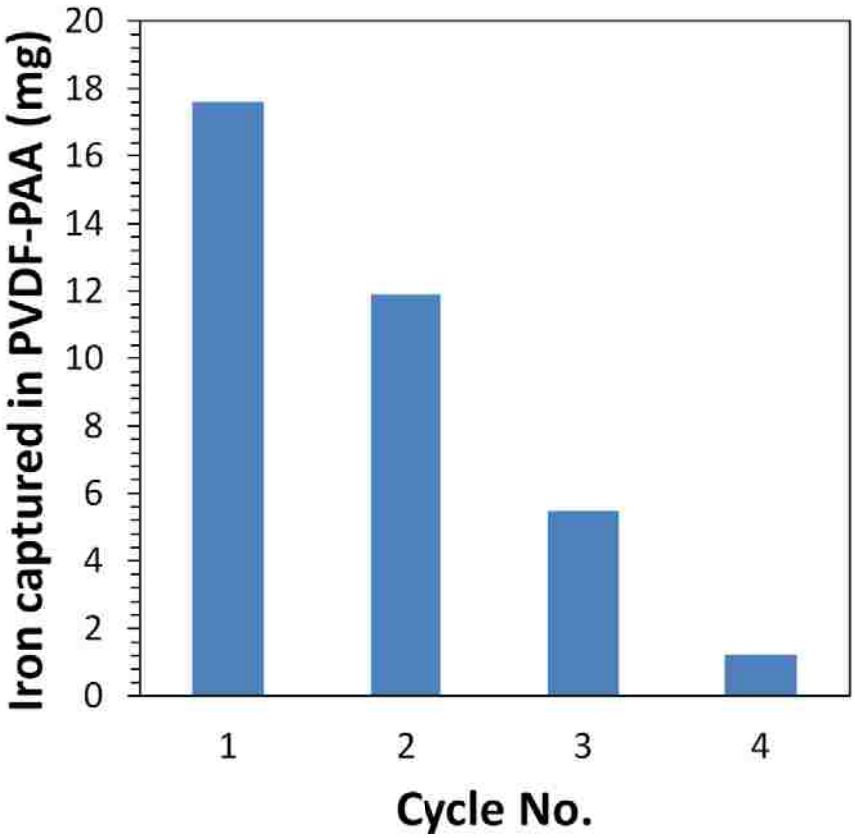

Figure 3.20. Iron captured by PVDF-PAA membranes during the ion exchange with $FeCl_2$ (4 cycles). $[FeCl_2]_0$= 3.57 mM, V=200 mL, pH=5.0-5.3.

magnetite. The interaction between iron oxide surfaces and PCP was expressed by the equilibrium reaction of sorbed and aqueous species (Xue et al. 2009).

At high pollutant concentrations, free radicals are mostly scavenged by the model contaminants (k=2 to 5×10^9 $M^{-1}s^{-1}$). At low pollutant concentrations, OH• can also be scavenged by H_2O_2 (k=3.3×10^7 $M^{-1}s^{-1}$) or iron oxide surfaces near the catalytic sites. As H_2O_2 concentration increases, this scavenging effect is expected to be enhanced. The oxidation rate of TCE could be estimated by second-order reaction kinetics at high H_2O_2 concentrations,

$$-\frac{dC_{TCE}}{dt} = k'' C_{OH\bullet} C_{TCE} \tag{E3.7}$$

where C_{TCE} is the TCE concentration in water, $C_{OH\bullet}$ is the concentration of OH• near the reactive sites, and k" is the second-order reaction rate. The pseudo-first-order kinetics can be obtained at the steady state ($C_{OH\bullet}$ is constant),

$$-\frac{dC_{TCE}}{dt} = k_{obs(TCE)} C_{TCE} \tag{E3.8}$$

where $k_{obs(TCE)}$ is the observed pseudo-first-order reaction rate of TCE oxidation ($k_{obs(TCE)}= k_1 C_{OH\bullet}$). In this system, TCE concentration could not be fit in the pseudo-first-order approximation over the full range. The adsorption has to be considered here since H_2O_2 concentration is low (0.13 vol%) and the iron oxide loading is relatively high (0.67-1.33 g/L). With the assumption that only TCE adsorbed on iron oxide surfaces can react with OH•, the following reaction pathway was proposed,

$$TCE \equiv S \xrightarrow{OH\bullet} I \equiv S + Cl^- \xrightarrow{OH\bullet} P \equiv S + Cl^- \tag{E3.9}$$

where ≡S represents the reactive sites on iron oxide surfaces, I is the intermediate formed during TCE oxidation, and P is the final products. TCE oxidation rate depends on the iron

oxide loading, the equilibrium constant for TCE adsorption, and the amount of OH• generated from H_2O_2 decomposition.

(E3.9) includes the following reactions:

$$TCE+ \equiv S \xrightarrow{k_{TCE,a}} TCE \equiv S \quad \text{(E3.10)}$$

$$TCE \equiv S \xrightarrow{k_{TCE,d}} TCE+ \equiv S \quad \text{(E3.11)}$$

$$TCE \equiv S + OH\bullet \xrightarrow{k_{TCE}} I \equiv S + mCl^- \quad \text{(E3.12)}$$

$$I \equiv S \xrightarrow{k_{in,d}} I+ \equiv S \quad \text{(E3.13)}$$

$$I+ \equiv S \xrightarrow{k_{in,a}} I \equiv S \quad \text{(E3.14)}$$

$$I \equiv S + OH\bullet \xrightarrow{k_{in}} P \equiv S + nCl^- \quad \text{(E3.15)}$$

$$P \equiv S \xrightarrow{k_{P,d}} P + S \quad \text{(E3.16)}$$

$$P + S \xrightarrow{k_{P,a}} P \equiv S \quad \text{(E3.17)}$$

where k_{TCE} and k_{in} are the oxidation rate of adsorbed TCE and reaction intermediate I with OH• respectively, and $k_{TCE,a}/k_{TCE,d}$ and $k_{in,a}/k_{in,d}$ are the corresponding adsorption and desorption rates on iron oxide surfaces. The number of chloride from the oxidative degradation (m and n) varies between one and three, depending on the reaction mechanism. At the steady state, the concentration of adsorbed TCE ($C_{TCE\equiv S}$) is constant, and thus the following relations can be obtained.

$$\frac{dC_{TCE\equiv S}}{dt} = k_{TCE,a}C_{TCE}C_S - k_{TCE,d}C_{TCE\equiv S} - k_{TCE}C_{TCE\equiv S}C_{OH\bullet}$$

$$= k_{TCE,a}C_{TCE}C_{S0}(1-\theta) - k_{TCE,d}\theta C_{S0} - k_{TCE}\theta C_{S0}C_{OH\bullet} = 0 \quad \text{(E3.18)}$$

$$\theta = \frac{C_{TCE}}{C_{TCE} + (k_{TCE,d} + k_{TCE}C_{OH\bullet})/k_{TCE,a}} \quad \text{(E3.19)}$$

$$\frac{dC_{TCE}}{dt} = -k_{TCE,a}C_{TCE}C_S + k_{TCE,d}C_{TCE\equiv S} = -k_{TCE,a}C_{TCE}C_{S0}(1-\theta) + k_{TCE,d}\theta C_{S0}$$

$$= -\frac{k_{TCE}C_{OH\bullet}C_{S0}C_{TCE}}{C_{TCE} + (k_{TCE,d} + k_{TCE}C_{OH\bullet})/k_{TCE,a}} = -\frac{k_1 C_{TCE}}{C_{TCE} + k_2} \quad \text{(E3.20)}$$

where $C_{OH\bullet}$ is constant at the steady state. C_{S0} and C_S are the concentrations of total reactive sites and unoccupied reactive sites, respectively. θ is defined as the fraction of occupied reactive sites ($\theta=C_{TCE\equiv S}/C_{S0}$). k_1 represents the reactivity of OH• with TCE in this system, and is proportional to the loading of catalysts ($k_1=k_{TCE}C_{OH\bullet}C_{S0}$). k_2 reflects the adsorption and desorption equilibrium of TCE on iron oxide surfaces ($k_2=(k_{TCE,d}+k_{TCE}C_{OH\bullet})/k_{TCE,a}$). By using the nonlinear least-square approximation in Matlab, the values of k_1 and k_2 were obtained. k_1 was 0.92×10^{-5} M/h with the catalyst loading as 0.67 g/L, and as expected it increased to 1.24×10^{-5} M/h when the loading was doubled (1.33 g/L). k_2 maintained at 3.15×10^{-5} M, suggesting the adsorption and desorption equilibrium of TCE was not affected by the amount of iron oxide. For the membrane supported iron oxide, the diffusion resistance from the bulk solution to the particles in the membrane pores resulted in a smaller k_1 value (0.7×10^{-5} M/h). Iron oxide nanoparticles were partially embedded in the PAA network, and some reactive sites might not be accessible to TCE. Therefore, the adsorption process was slowed down, and k_2 increased to 5.43×10^{-5} M. As shown in Figure 3.21, the experimental data fit the model fairly well. At a high concentration ($C_{TCE}>>k_2$), the oxidation of TCE was almost a zero-order reaction ($dC_{TCE}/dt=-k_1$). While at a low concentration ($C_{TCE}<<k_2$), it could be approximated as a first-order reaction ($dC_{TCE}/dt=-k_1C_{TCE}/k_2$).

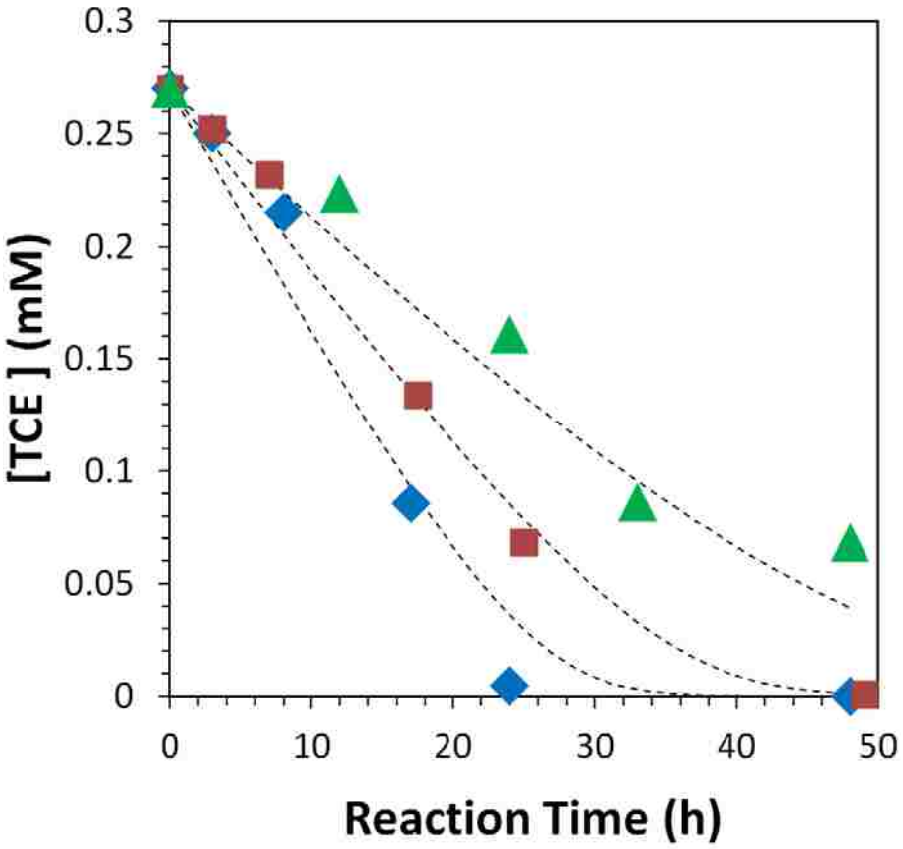

Figure 3.21. TCE concentrations predicted by the adsorption and desorption model (E3.20, dash lines) in CMC-stabilized and membrane supported iron oxide catalyzed free radical oxidation. Iron oxide suspension (■) 0.67 g/L, (◆) 1.33 g/L; (▲) PVDF-PAA-iron oxide.

Chapter Four Reactive Functionalized Membranes for Polychlorinated Biphenyl Degradation

Membranes have been widely used in water remediation (e.g. desalination, heavy metal removal and selective separations) because of the ability to control membrane pore size, thickness, and surface charge. The incorporation of nanomaterials (particularly in microfiltration type membranes) into the membranes provides added benefits through increased reactivity with different functionality. In this chapter, the dechlorination of 2-chlorobiphenyl in the aqueous phase by nanoparticle-based reactive membrane systems was investigated. Fe/Pd bimetallic nanoparticles were synthesized (in-situ) within polyacrylic acid (PAA) functionalized polyvinylidene fluoride (PVDF) membranes for degradation of polychlorinated biphenyls (PCBs). Biphenyl formed in the reduction was further oxidized into hydroxylated biphenyls and benzoic acid by an iron-catalyzed hydroxyl radical (OH•) reaction. The formation of magnetite on Fe surface was observed. This combined pathway (reductive/oxidative) could reduce the toxicity of PCBs effectively while eliminating the formation of chlorinated degradation byproducts. The successful manufacturing of full-scale functionalized membranes demonstrated the possibility of applying reactive membranes in the practical water treatment. The graphic abstract of Chapter Four is shown in Figure 4.1.

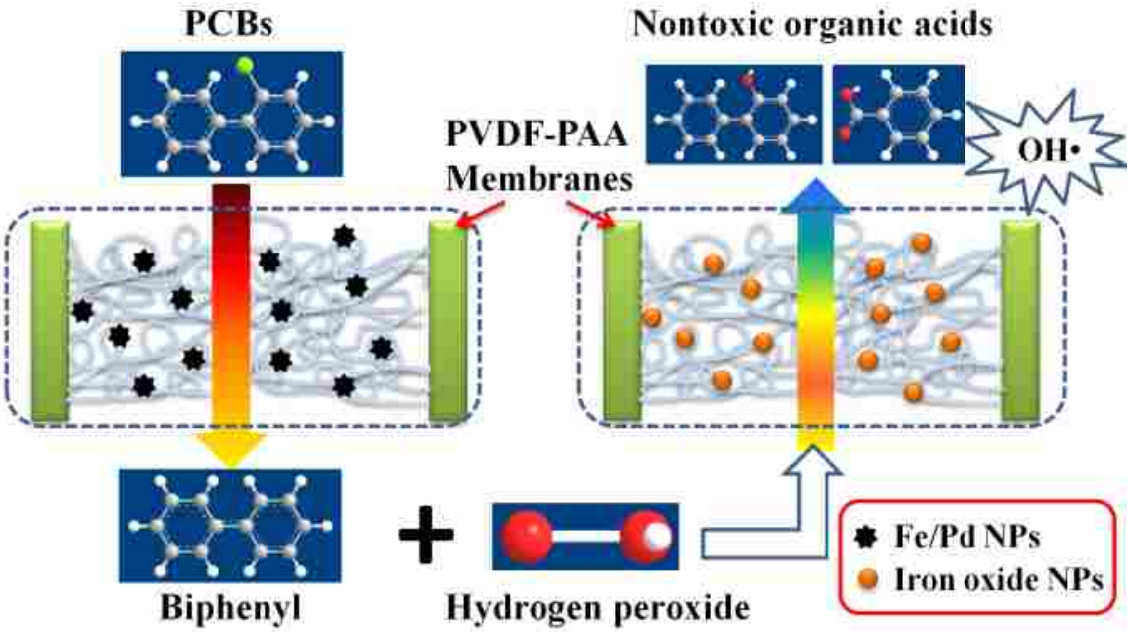

Figure 4.1. Graphic abstract of Chapter Four.

In Chapter Three, membrane supported iron oxide nanoparticles have shown high reactivity in the catalytic decomposition of H_2O_2 for free radical generation. TCE is degraded with chloride as a final product. However, toxic chlorinated organic acids can also be formed during the oxidation step. To eliminate the formation of those toxic intermediates, chlorine atoms can be removed through reductive dechlorination before the oxidative treatment. This chapter mainly focuses on using a combined chemical treatment to reduce the toxicity of polychlorinated biphenyls (PCBs). It starts with a short review of challenges presented in reductive and oxidative pathways. Next, the dechlorination of 2-chlorobiphenyl with functionalized membrane supported Fe/Pd nanoparticles is studied in convective mode, which eliminates the diffusion resistance in batch mode. It is followed by the analysis of products in biphenyl oxidation with free radicals. Then the free radical reaction mechanism is discussed based on the identified products. XRD and TEM-EELS shows the transformation of iron to magnetite during H_2O_2 treatment.

4.1 Introduction

Membranes have been used as selective barriers for fluid separation based on size exclusion (sieving), charge (Donnan exclusion) and diffusion (solution-diffusion). In recent years, membrane functionalization (such as surface and pore modification with functional groups) provides us an opportunity to incorporate catalytic particles and enzymes in the membrane pores for in-situ reaction (Dai and Bruening 2002; Ulbricht 2006; Datta, Cecil et al. 2008; Kim and Van der Bruggen 2010). Iron-related particles such as iron and iron oxide have drawn more and more attention in the detoxification of chlorinated organic compounds. Those compounds can be degraded into less toxic or

nontoxic products by reductive (Johnson, Scherer et al. 1996; Wang and Zhang 1997; Zhang 2003; Lien and Zhang 2007; He and Zhao 2008; Tee, Bachas et al. 2009) or oxidative pathway (Watts, Udell et al. 1999; Pignatello, Oliveros et al. 2006; Costa, Moura et al. 2008; Pham, Lee et al. 2009; Sun and Lemley 2011), depending on the valence state of iron.

Zero-valent bulk iron and nanoscale iron particles have been extensively studied to reduce chloro-organics in water by electron transfer reaction (Johnson, Scherer et al. 1996; Lowry and Johnson 2004). However, a second metal such as Pd or Ni is necessary to form bimetallic Fe/Pd or Fe/Ni to accomplish the complete removal of chlorine atoms from polychlorinated biphenyls (PCBs). The corrosion of iron in water generates the hydrogen gas (H_2), which is activated by Pd catalyst (H•) for hydrodechlorination (He and Zhao 2008). On the other hand, iron oxides are effective free radical catalysts in a heterogeneous Fenton reaction. The addition of hydrogen peroxide (H_2O_2) is required to produce the hydroxyl radicals (OH•).

Both reductive and oxidative pathways present challenges in the dechlorination of PCBs. The reductive method can only remove the chlorine atoms from the aromatic ring resulting in a biphenyl product, which is mildly toxic. The oxidative method is able to convert PCBs into the hydroxylated PCBs (Sedlak and Andren 1991), followed by the aromatic ring cleavage (Pignatello and Chapa 1994), eventually forming carboxylic acids or even carbon dioxide (Ahmad, Simon et al. 2011). However, the chlorinated degradation byproducts formed by hydroxylation and the ring-opening reaction are still toxic and have higher water solubility than PCBs. Therefore, a combined pathway is more beneficial in terms of first converting PCBs into biphenyl by Fe/Pd reduction,

followed by an oxidative treatment involving the free radical generation (Figure 4.2). The toxicity of biphenyl is expected to be reduced without forming any chlorinated byproduct. We reported the synthesis of Fe (Smuleac, Varma et al. 2011), Fe/Pd (Xu and Bhattacharyya 2007; Smuleac, Bachas et al. 2010), Fe/Ni (Xu, Dozier et al. 2005), and iron oxide (Gui, Smuleac et al. 2012) immobilized polyvinylidene fluoride (PVDF)/polyacrylic acid (PAA) membranes for trichloroethylene (TCE) and PCB dechlorination. These functionalized membranes have been used as the porous support to control NP synthesis (size, loading), to recapture the dissolved metal ions (ion exchange), to minimize the particle agglomeration (in-situ synthesis) and to allow the convective flow studies through pores (conversion control by the residence time) (Xu and Bhattacharyya 2007; Wang, Chen et al. 2008; Wu and Ritchie 2008). Besides, they can be made into modules for on-site applications, and it's relatively easy to replace and regenerate the modules.

However, the possibility of using a combined pathway with iron immobilized membranes for PCB degradation has not been studied. The performance of membranes on the reduction of PCBs in aqueous phase and the byproducts formed during the oxidation of biphenyl are also unknown.

4.2 Functionalized PVDF-PAA Membrane and Fe/Pd Nanoparticle Properties

The in-situ polymerization of acrylic acid inside PVDF membrane pores was conducted in the aqueous phase with no organic solvent involved. The cross-linking reaction between PAA chains via NNMA bonding created a very stable polymer network, which would not collapse under acidic or alkaline environment. PVDF is well-known for its excellent chemical resistance to most acids, weak alkalis and oxidizing agents. Both

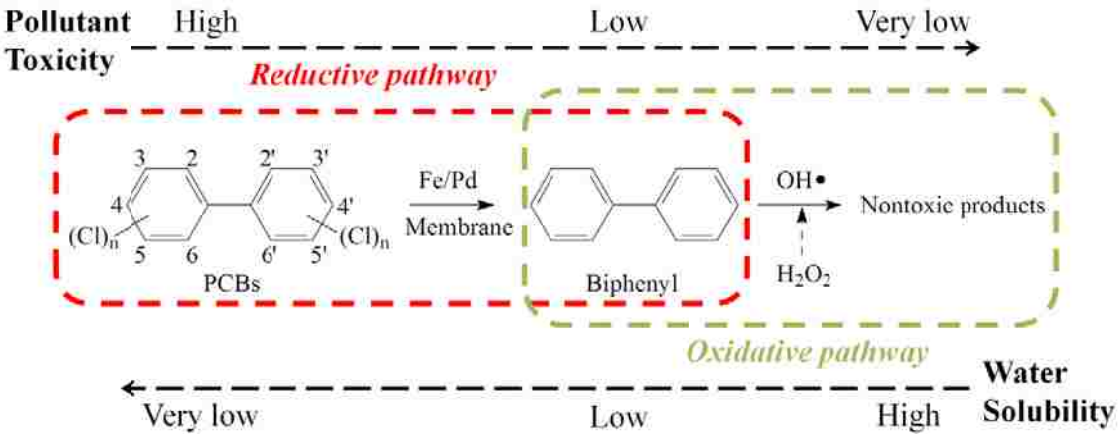

Figure 4.2. Combined (reductive and oxidative) pathway for PCB detoxification.

PVDF and PAA can withstand the thermal treatment in this polymerization.

As expected, the pore size of PVDF membrane decreased to 300±80 nm due to the formation of PAA domain inside the pores after polymerization (Figure 4.3). PAA is a non-toxic polyelectrolyte with high ion exchange capacity. At a neutral pH, the negatively charged carboxylate ions are intended to capture the positively charged metal ions such as Fe^{2+}, which is the precursor of iron nanoparticles (Lewis, Datta et al. 2011).

Based on the weight gain of membranes after polymerization and the amount of iron captured by ion exchange, the ratio of carboxyl groups and Fe^{2+} inside the membrane was calculated to be 1.8, which was close to the theoretical ratio 2. After the reduction and post-coating, the core (Fe)-shell (Pd) particles were uniformly distributed on the membrane surface and inside the pores with the size of 80±20 nm (Figure 4.3). EDX spectrum also shows the successful coating of Pd on the surface of Fe, which activates the hydrogen gas from iron corrosion for chloro-organic hydrodechlorination. The particle size is dependent on the molar ratio of reducing agent ($NaBH_4$) to the precursor (Fe^{2+}). Thus the excessive reductant is needed to make small and uniform particles (Zhang 2003). The particle loading can be increased by multi-cycle ion exchange since the carboxyl groups stay in the membranes during the particle synthesis with Na^+ as counterions. However, the repeated ion exchange and reduction may result in the agglomerated particles, and also cause a significant increase of pressure drop through a dense membrane in the convective flow operation.

The water permeability reduced significantly after Fe/Pd synthesis as the membrane pore volume decreased. PVDF membrane pores become more uniform after incorporating PAA. To study the membrane reactivity, PVDF-PAA membrane pores are

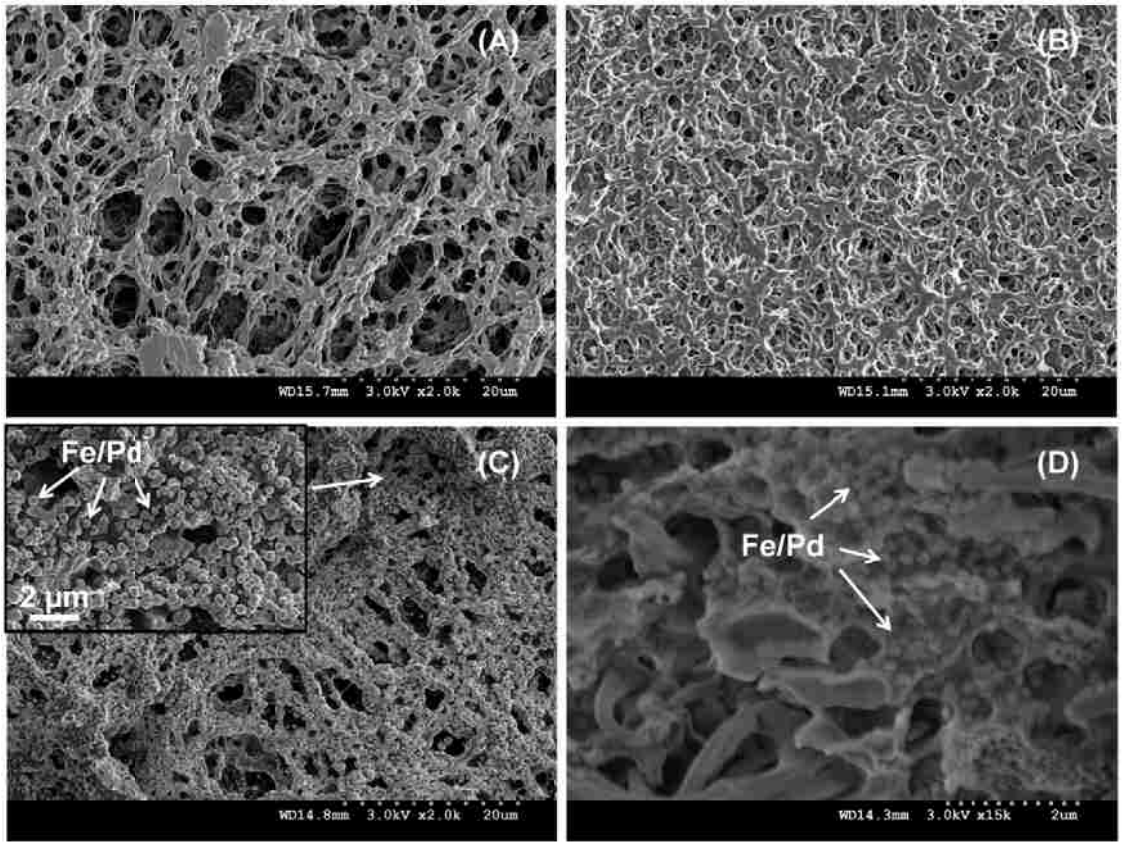

Figure 4.3. SEM images of hydrophilized Millipore PVDF membrane (A), PAA functionalized PVDF membrane (B), and PVDF-PAA-Fe/Pd membrane top surface (C) and cross section (D). White arrows indicate Fe/Pd nanoparticles.

assumed to be cylindrical for calculation purpose, and PAA is uniformly distributed in the pores without changing the porosity. The equivalent diameters of PAA functionalized and Fe/Pd immobilized membranes can be estimated via the Hagen-Poisseuille equation.

$$\Delta P = \frac{128\eta LQ}{\pi D^4} \tag{E4.1}$$

$$A = J_w / \Delta P = Q/(A_m \Delta P) \tag{E4.2}$$

$$\frac{D}{D_0} = \left(\frac{A}{A_0}\right)^{1/4} \tag{E4.3}$$

where η is the dynamic water viscosity, L is the membrane thickness, Q is the volume flow rate, J_w is the water flux, A_m is the membrane external area, and ΔP is the transmembrane pressure. D_0 and A_0 are the equivalent diameter (650 nm) and water permeability (4400 L/(m^2·h·bar)) of PVDF membrane support. D and A are the equivalent diameter and water permeability of pore functionalized membranes. After the functionalization, A was 8.38 L/(m^2·h·bar) at pH=7.7, and D was 110 nm. After immobilizing the particles, A decreased to 1.02 L/(m^2·h·bar) at pH=7.5, and the corresponding pore size was 80 nm. The pore size discrepancies between those calculated and observed (PVDF-PAA: 300±80 nm; PVDF-PAA-Fe/Pd: 130±50 nm from SEM images) may be due to the fracture of membrane surface during the sample preparation (e.g. liquid nitrogen treatment).

The full-scale PVDF membranes had a uniform pore size distribution based on bubble point test, and the average pore size decreased to 124 nm after PAA functionalization with ethylene glycol as the cross-linker. The ester bonds were formed between ethylene glycol and carboxyl groups (molar ratio 1:2) to prevent the leaching of PAA from the membrane (Smuleac, Bachas et al. 2010). The membrane surface was

highly negatively charged based on the zeta-potential result (-46.8 mV in 1.7 mM NaCl at pH 5), suggesting the successful incorporation of PAA polymer in PVDF membranes.

4.3 Membrane pH Responsive Behavior

Polyelectrolytes with weak acid or alkali groups were reported to have the pH responsive behavior (Stuart, Huck et al. 2010; Wandera, Wickramasinghe et al. 2010). PAA functionalized PVDF membranes were also found to exhibit this interesting property. Depending on the environmental pH, carboxyl groups of PAA can be in a compact state (low pH) or an ionized state (high pH), which results in different water permeability through membranes. The dissociation of carboxyl groups and the elongation of PAA network result in the decrease of water permeability as pH increases above the pKa of PAA (4.3-4.9). Therefore, when PAA fills in PVDF membrane pores, the pore size can be tuned by varying the solution pH. Hu and Dickson have studied the effects of mass gain and cross-linking degree on the pH responsive behavior of PVDF-PAA membrane (Hu and Dickson 2007). They found that a lower mass gain always resulted in higher water permeability and flux ratio at pH 2.5 to that at pH 7.4. To obtain more carboxyl groups for particle synthesis while maintaining the water permeability, a monomer solution at low AA concentration (1.6 M) was used with 1 mol% cross-linker. The water flux of membranes at different pH is shown in Figure 4.4. The ratio of water permeability at pH 3.1 to that at 7.7 was 8.6, and the transition pH was between 4.3 and 5.3. The flux modulation results also proved the pH reversibility of functionalized membranes. However, only 85±7% of original water flux was rejuvenated due to the change of polymer configuration under the applied pressures.

The water flux of full-scale functionalized membranes was also reproducible with

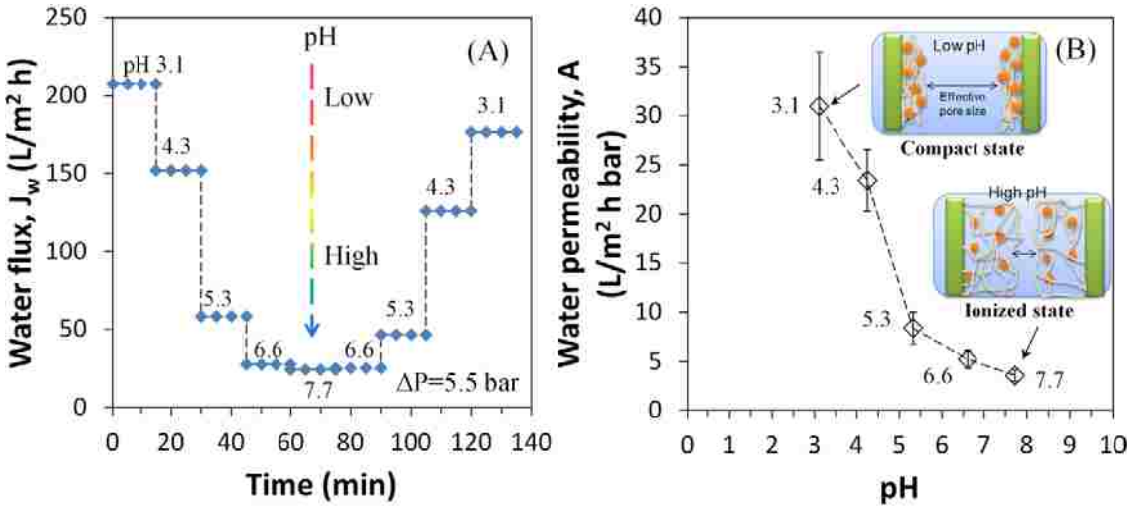

Figure 4.4. Flux modulation of lab-scale PVDF-PAA membranes by pH (12% PAA weight gain). (A) Water flux at 5.5 bar; (B) water permeability. At each pH, three samples were collected after the permeate pH became the same as the feed. Thickness of PVDF membranes: 125 μm.

pH variation (Figure 4.5). The water permeability decreased from 1355 L/(m^2·h·bar) to 383 L/(m^2·h·bar) as the solution pH was increased from 3.0 to 7.3, showing that the membrane pores were highly tunable. The full-scale functionalized membrane has a thickness of 70 μm compared to 125 μm for functionalized Millipore membranes. With less PAA incorporated, its average pore size was larger (124 nm compared to 80 nm). The water permeability is proportional to the reciprocal of membrane thickness and fourth power of pore size (E4.3). Both factors resulted in higher water permeability for full-scale membranes.

4.4 PCB Reductive Dechlorination

The functionalized membrane provides an opportunity to study the PCB dechlorination in both batch and convective mode. Depending on the pore size and mixing method, the resulting mass transfer could be critical in PCB dechlorination.

4.4.1 Batch Study with Longevity Test

To eliminate the effects of solvent and pH on the dechlorination rate (Fang and Al-Abed 2008a; Fang and Al-Abed 2008b), all of the experiments were conducted in the deoxygenated water at pH=7.5-8.0. 2-Chlorobiphenyl (PCB1) was selected as a model compound due to its relatively high solubility (31.3 μM) in water. After the reduction of $NaBH_4$ and post coating of Pd, membranes turned black and were washed with the deoxygenated water until the washing solution pH was near neutral. For each vial, two pieces of membranes were immersed in the feed solution, giving a total loading of 0.65 g/L for Fe and 5.85 mg/L for Pd (0.9 wt% as Fe). The conversion of PCB was 93% after 2 h, and the biphenyl yield was 91% (Figure 4.6). The total carbon balance was 95±3%.

The membrane surface turned brown after dechlorination, which could be

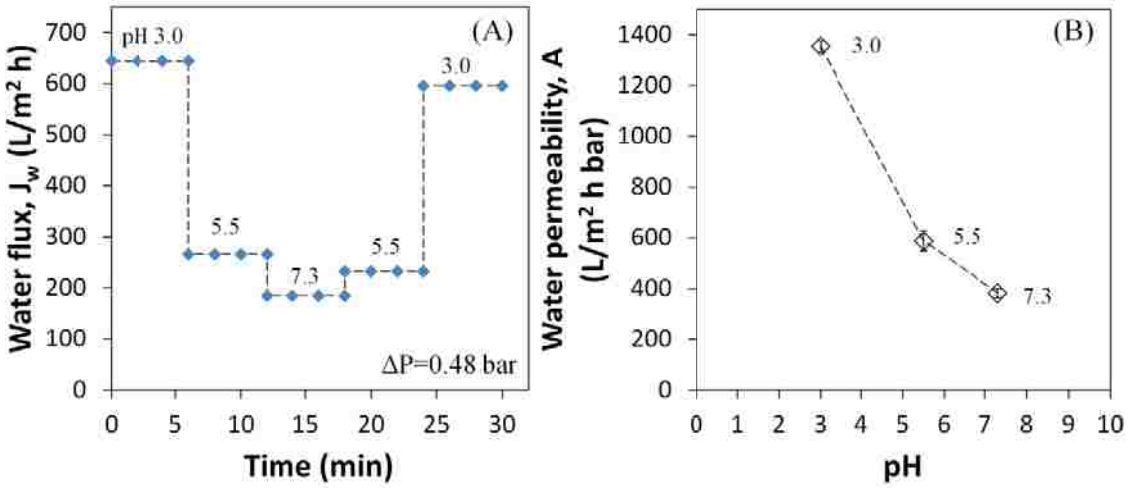

Figure 4.5. Flux modulation of full-scale PVDF-PAA membranes by pH. (A) Water flux at 0.48 bar and (B) water permeability. At each pH, three samples were collected after the permeate pH became the same as the feed. Thickness of PVDF layer: 70 μm.

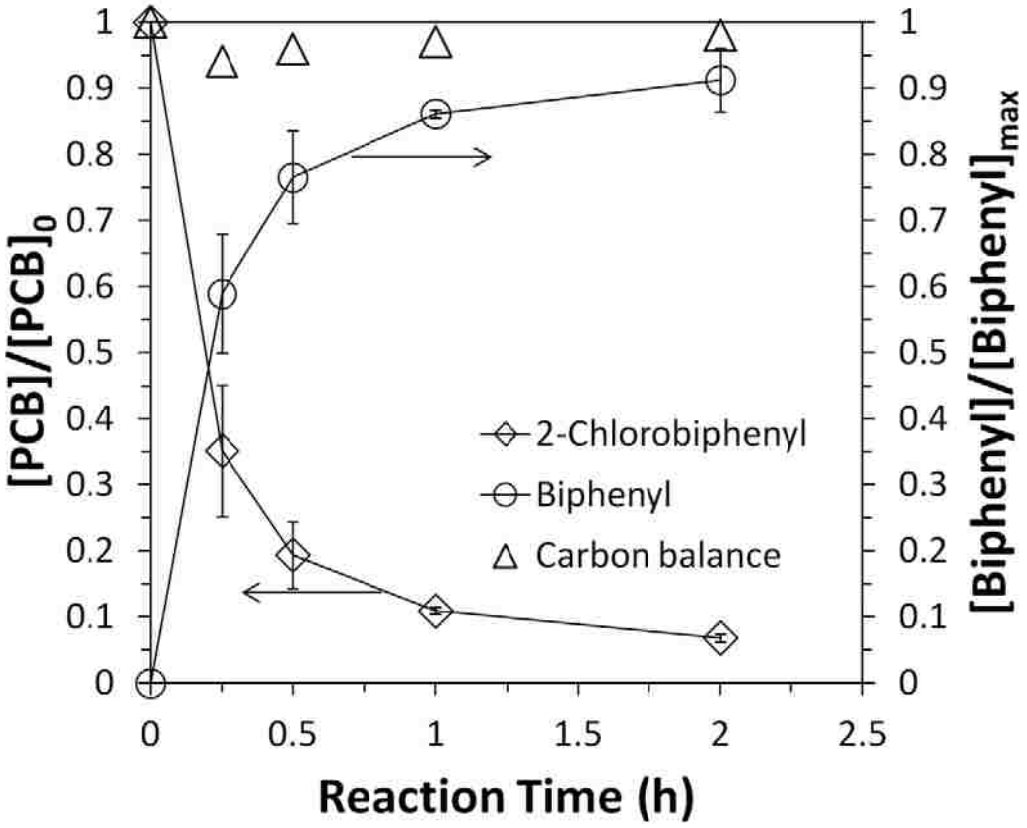

Figure 4.6. Batch study (no convective flow through pores) of 2-chlorobiphenyl dechlorination and biphenyl formation by Fe/Pd immobilized PVDF-PAA membranes. $[PCB]_0$=31μM, $[Fe]_0$=0.65 g/L (average particle size: 80 nm), [Pd]=0.9 wt% as Fe, pH=7.5-8.0.

explained by the corrosion of iron. The dissolved Fe(II) could either be captured by carboxyl groups of functionalized membranes, or precipitate on iron particles as iron hydroxide at the experimental pH. Less than 0.6 μM of Fe (0.005 wt% of total Fe) and 0.7 μM of Pd (1.1 wt% of total Pd) were released.

Membranes were reused for dechlorination after washing (with deoxygenated water) and drying (with nitrogen gas flow) steps. The conversion of PCB was 56% after 2 h. The reactivity loss was mainly due to the formation of iron oxide through iron corrosion and oxidation. Iron could be regenerated by the acid treatment followed by reduction, but the reactivity was restored only partially (Zhu and Lim 2007).

4.4.2 Convective Flow Study

The diffusion resistance through a membrane barrier usually made the observed reaction rate smaller than the intrinsic rate. To obtain the intrinsic rate of PCB dechlorination and to evaluate the stability of membrane supported Fe/Pd nanoparticles under the applied pressure, the reduction was conducted in convective mode.

Functionalized membranes with bimetallic nanoparticles (6.1 mg Fe loading and 0.9 wt% Pd as Fe) were mounted in a dead-end filtration cell. To eliminate the loss of biphenyl product due to the polymer adsorption, the biphenyl solution (26.5 μM) was first permeated through the membrane until the adsorption equilibrium ($C_{feed}=C_{permeate}$) was achieved. The feed solution (31 μM) was then passed through the cell. It should be noted that biphenyl doesn't react with Fe/Pd.

The residence time of 2-chlorobiphenyl (τ) in the functionalized membrane was varied by changing the pressure applied to the cell (5-11 bar). It was calculated as $\tau=V_m/(J_wA_m)$, where V_m is the membrane pore volume ($V_m=\varepsilon_sA_mL$), J_w is the water flux

at a specific pressure, A_m is the external area of membrane (13.2 cm^2), ε_s is the membrane porosity (70%) and L is the membrane thickness (125 μm). However, both the polymer and particles formed inside membranes occupied some pore volume. Therefore, the pore volume after functionalization can be obtained as $V= \varepsilon_s A_m d - V_{GEL} - V_{NP}$, where V_{GEL} is the PAA gel volume in the dried state (based on PAA weight gain) and V_{NP} is the volume occupied by Fe/Pd particles (calculated from the particle loading and density).

Each sample was collected after 5 min equilibration flow and one duplicate was examined to reduce the error from catalyst deactivation. The water flux was shown in Figure 4.7. The presence of PAA on the membrane top surface could cause the particle formation. Therefore, the feed concentration was analyzed throughout the reaction and the conversion of 2-chlorobiphenyl was normalized. At residence times of 25.7 s, 34.6 s, and 50.2 s, the conversions of PCB were 66.3%, 74.2%, and 80.6% respectively (Figure 4.8). The corresponding biphenyl yields ([biphenyl]/$[biphenyl]_{max}$) were 59.0%, 65.1%, and 69.6%. By increasing the residence time, the complete dechlorination could be achieved. The total carbon balance was 90±3%.

4.4.3 Modeling of PCB Dechlorination in Membrane Pores

PCB dechlroination by Fe/Pd followed a pseudo-first-order rate law (Lien and Zhang 2007),

$$r = \frac{dC_{PCB}}{dt} = -k_{obs,PCB} C_{PCB} = -k_{SA,PCB} \alpha_S \rho_m C_{0,PCB} (1 - X) \qquad \text{(E4.4)}$$

where r is the reaction rate (M/h), $C_{0,PCB}$ and C_{PCB} are the concentrations of 2-chlorobiphenyl in the feed (M) and at time t (h), $k_{obs,PCB}$ is the observed rate constant (h^{-1}), $k_{SA,PCB}$ is the surface-area-normalized rate constant ($L/m^2 \cdot h$), α_s is the specific surface area of Fe/Pd particles (m^2/g), ρ_m is the loading of particles (58.5 g/L), and X is the

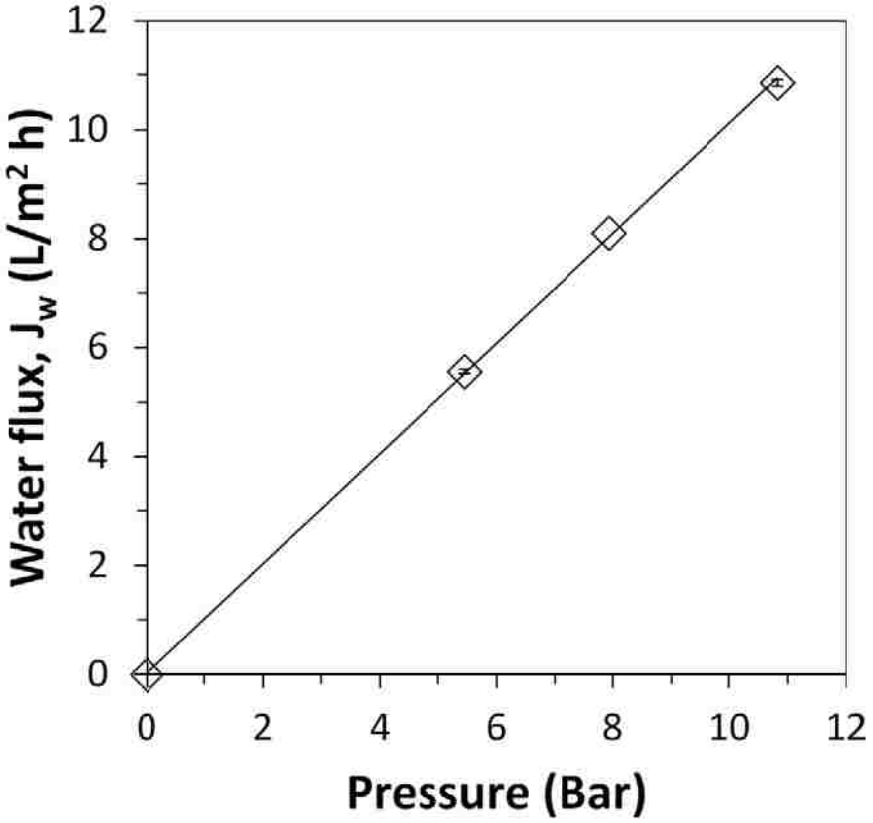

Figure 4.7. Water flux of Fe/Pd immobilized PVDF-PAA membranes in 2-chlorobiphenyl dechlorination (convective flow). $[PCB]_0$=31μM, mass (Fe)=6.1 mg (average particle size: 80 nm, ρ_m=58.5 g/L), [Pd]=0.9 wt% as Fe, pH=7.5-8.0. Membrane external area: 13.2 cm^2.

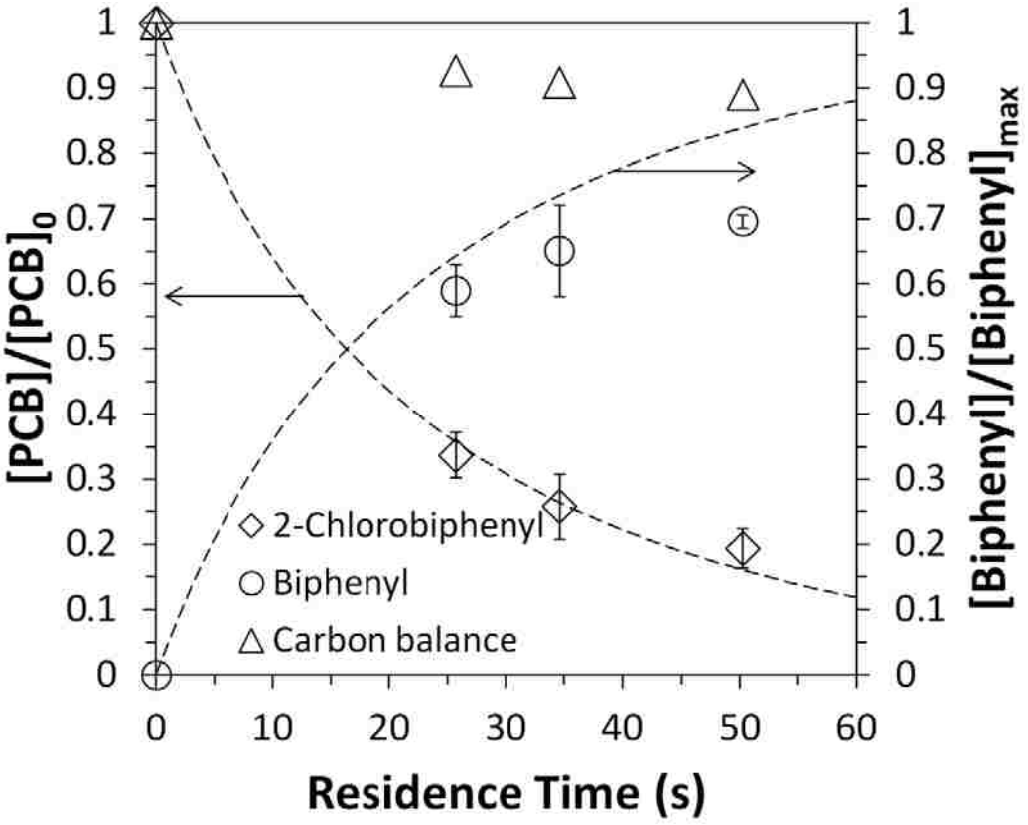

Figure 4.8. Convective flow study of 2-chlorobiphenyl dechlorination and biphenyl formation by Fe/Pd immobilized PVDF-PAA membranes. $[PCB]_0$=31μM, mass (Fe)=6.1 mg (average particle size: 80 nm, ρ_m=58.5 g/L), [Pd]=0.9 wt% as Fe, pH=7.5-8.0. Pressure varied between 5 and 11 bar. Membrane external area: 13.2 cm^2. Dash lines are concentrations of 2-chlorobiphenyl and biphenyl predicted by laminar flow reactor model and the average $k_{SA,PCB}$ obtained (0.32±0.04 L/m^2h).

conversion of 2-chlorobiphenyl. If assuming that the particles are spherical with an average diameter as 80 nm, the specific surface area is 9.5 m^2/g.

With PAA incorporated in PVDF membrane pores, the heterogeneity of PVDF membrane decreases, and the whole membrane can be considered as a packed bed reactor with catalysts uniformly distributed inside. It can be further simplified that each membrane pore is a packed bed reactor with the same pore size and particle loading. Therefore, the overall conversion of 2-chlorobiphenyl is equal to that in a single pore. Hence, each membrane pore can be considered as a laminar flow reactor (LFR) due to the small Reynolds number (Re<2000) (Chen 1983). Compared to plug flow reactor (PFR) and continuous stirred-tank reactor (CSTR), the water flow in LFR has a fully developed parabolic velocity profile (Figure 4.9), and is closer to the real situation. The velocity distribution is,

$$u_r = u_0(1-\frac{r^2}{R^2}) \tag{E4.5}$$

$$u_{ave} = \frac{\int_0^R u_r 2\pi r dr}{\int_0^R 2\pi r dr} = \frac{u_0}{2} \tag{E4.6}$$

where u_r and u_0 are the velocities at radius r and pore center, and u_{ave} is the average velocity in the pore. R is the equivalent pore radius. The volume flow rate (Q_r) through an annular element of radius r is,

$$Q_r = 2\pi r u_r dr = \frac{2\pi r L dr}{\tau} \tag{E4.7}$$

where L is the thickness of membrane, and τ is the residence time at radius r. The average conversion can be expressed as,

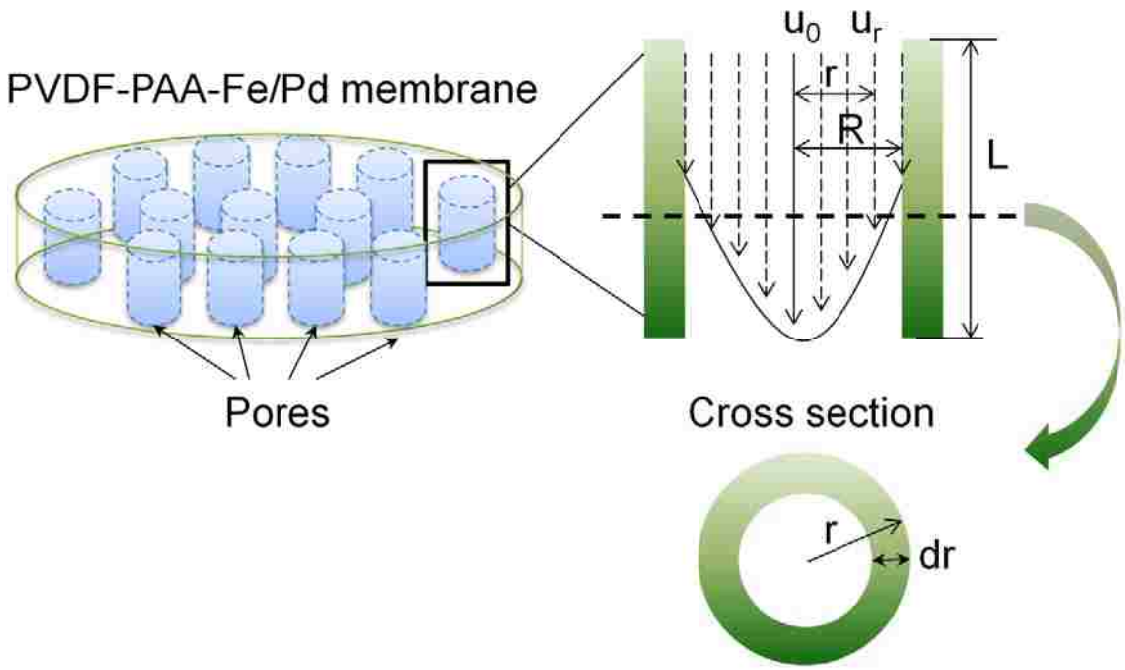

Figure 4.9. Schematic diagram of laminar flow profile in functionalized membranes (PVDF-PAA-Fe/Pd).

$$X_{ave} = \frac{\int_0^R X 2\pi \cdot r \cdot L \cdot dr / \tau}{\int_0^R 2\pi \cdot r \cdot u_r \cdot dr} \tag{E4.8}$$

$$\tau = \frac{L}{u_r} = \frac{L}{u_0[1-(r/R)^2]} \tag{E4.9}$$

where X_{ave} and X are the average and fractional conversion. Differentiating E4.9 with r gives,

$$rdr = \frac{LR^2 d\tau}{2u_0 \tau^2} \tag{E4.10}$$

$$X_{ave} = \frac{2L^2}{u_0{}^2} \int_{\tau_0}^{\tau_\infty} \frac{X}{\tau^3} d\tau \tag{E4.11}$$

where τ_0 and τ_∞ are the residence time of 2-chlorobiphenyl at the pore center and wall (h). The boundary conditions are,

$$\tau_0 = \frac{L}{u_0} \quad \text{at r=0}$$

$$\tau_\infty = \infty \quad \text{at r=R}$$

For the first-order reaction,

$$X = 1 - e^{-k_{obs,PCB}\tau} \tag{E4.12}$$

Therefore, the conversion of reactants with residence time in LFR is,

$$X_{ave} = 2\tau_0^2 \int_{\tau_0}^{\tau_\infty} (\frac{1}{\tau^3} - \frac{e^{-k_{obs,PCB}\tau}}{\tau^3}) d\tau = 1 - 2\tau_0^2 \int_{\tau_0}^{\tau_\infty} \frac{e^{-k_{obs,PCB}\tau}}{\tau^3} d\tau \tag{E4.13}$$

The integral term can be estimated through integration by parts. The Hilder's approximation gives an approximated solution (Fogler 2005),

$$X_{ave} = 1 - \frac{1}{(1+0.25\tau k_{obs,PCB}) e^{0.5\tau k_{obs,PCB}} + 0.25\tau k_{obs,PCB}} \tag{E4.14}$$

where $\tau k_{obs,PCB}$ is the Damköhler number. With the known values of X_{ave}, $k_{obs,PCB}$ can be obtained by solving the nonlinear equation with Matlab. Therefore, $k_{SA,PCB}$ is 0.32±0.04 L/m^2h under the convective flow condition, which increased by 1.3 times than that obtained in batch study (0.26 L/m^2h). The result shows that the convective mode operation indeed eliminated the diffusion resistance from bulk solution to pore region.

The dechlorination rate obtained with Fe/Pd nanoparticle suspension ($k_{SA,PCB}$=0.18 L/m^2h) was close to the previous results (0.13±0.03 L/m^2h) (Fang and Al-Abed 2008b), but lower than that obtained in membranes phase (Figure 4.10). The functionalized membrane structure could play an important role in enhancing the dechlorination by preventing the particle aggregation. Alternatively, the cross-linker NNMA might create hydrophobic microdomains inside the polymer, which have strong affinity to hydrophobic compounds (Wang and Engberts 1994). PCB partitioning in the membrane was also studied, and less than 10% of PCB in feed solution was adsorbed. For long term water treatment with full-scale membrane modules, the adsorption and desorption process of PCB in the membrane can be negligible since the feed concentration is much lower (μg/L level) than that used in this study (5.9 mg/L), and the equilibrium is achieved fast with the solution circulating through membranes.

By increasing the metal loading, the dechlorinaton rate can be enhanced (Smuleac, Bachas et al. 2010). During the ion exchange, the carboxyl groups were deprotonated, forming chelates with Na^+ and Fe^{2+}. After reduction, the carboxyl groups were back to Na^+ form, and the membrane still had the ion exchange capacity. The functionalized membranes could retain the metal ions with PAA by ion exchange while maintaining the solution pH. However, the ion exchange capacity might drop as the iron loading

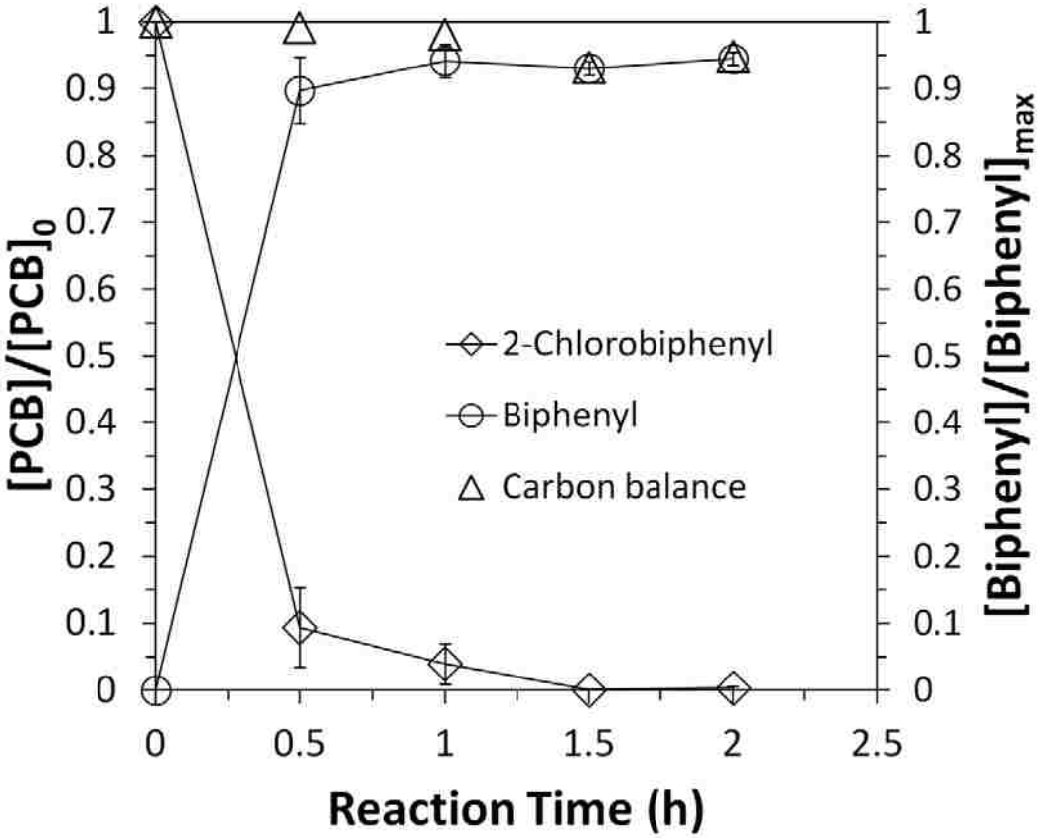

Figure 4.10. Batch study of 2-chlorobiphenyl dechlorination and biphenyl formation in Fe/Pd nanoparticle suspension. $[PCB]_0$=31 μM, $[Fe]_0$=0.5 g/L (BET surface area:37.8 m^2/g), [Pd]=0.9 wt% as Fe, pH=7.3-7.5.

increased by each cycle. The amount of Pd coating can also vary the reaction rate. The percentage of reactive sites decreased when there was more than one layer of Pd on the surface of Fe (Xu and Bhattacharyya 2007).

4.5 Biphenyl Oxidative Degradation

After the reductive dechlorination, PCB was converted to biphenyl, which required further treatment to reduce the mild toxicity. Although there were studies showing biphenyl could be decomposed by some bacteria or fungi (Schwartz, Williams et al. 1980; Mohn, Westerberg et al. 1997; Yang, Yoshida et al. 2008), the biological metabolism was a time-consuming process, and usually required a moderate condition to maintain the microorganism activity. Instead, the free radical Fenton reaction was used here to degrade biphenyl.

Iron was partially oxidized after PCB dechlorination. A layer of iron hydroxid/oxide was deposited on the surface of Fe/Pd. In the presence of iron oxides, OH• is generated in the decomposition of H_2O_2, and can oxidize the most recalcitrant organics at near diffusion-controlled rates. Additionally, iron below the iron oxide layer can also react with H_2O_2, producing OH•. Both dissolved iron and highly reactive iron oxide formed in iron oxidation with H_2O_2 can enhance the free radical generation (Keenan and Sedlak 2008).

The biphenyl oxidation with the membrane supported Fe/Pd (after dechlorination), freshly made Fe, and unstabilized iron oxide synthesized via air oxidation of iron (Gui, Smuleac et al. 2012) was studied. The same amount of H_2O_2 was added in each system. A small temperature rise (3 °C) was observed. Biphenyl was completely degraded within 15 min in batch mode by membrane supported Fe/Pd and Fe (Figure 4.11A). The solution

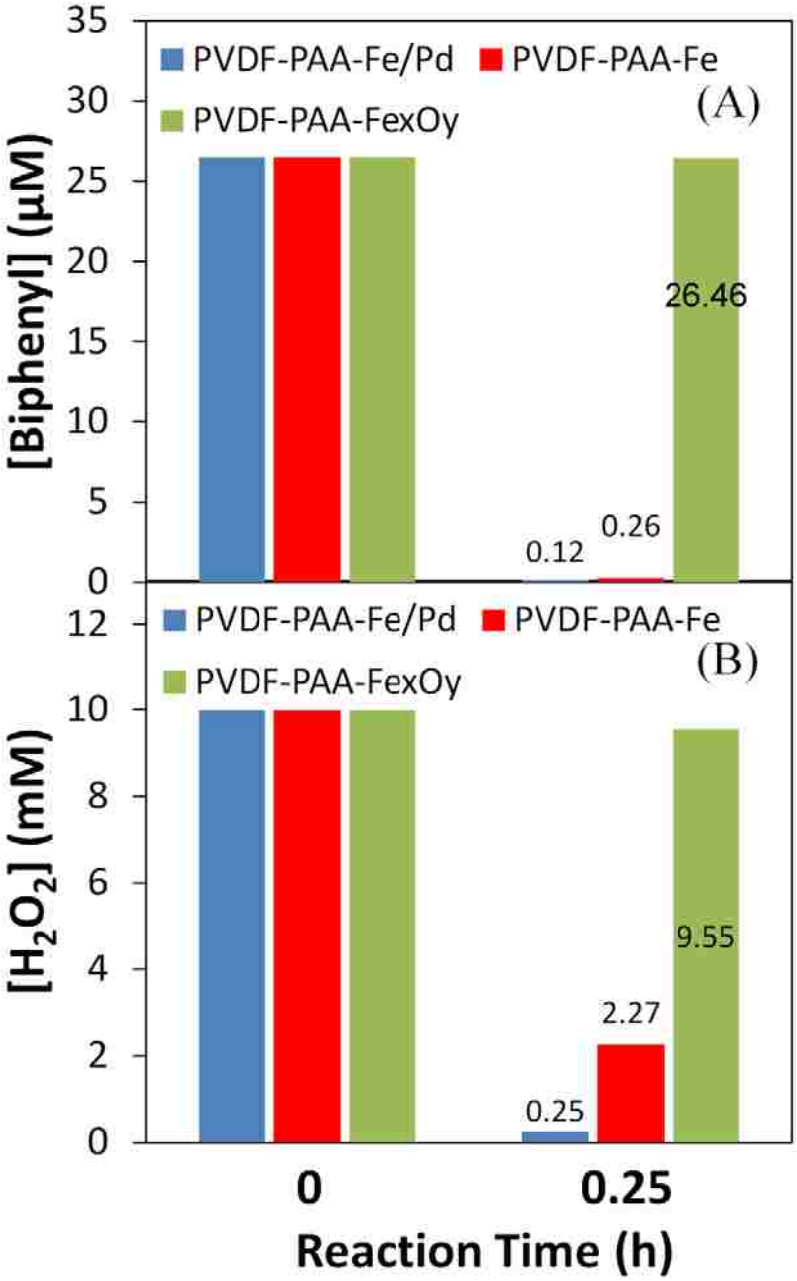

Figure 4.11. Batch study of (A) biphenyl oxidation and (B) H_2O_2 consumption with Fe/Pd, Fe, and Fe_xO_y (iron oxide) immobilized PVDF-PAA membranes. $[Biphenyl]_0$=26.5 μM, $[H_2O_2]_0$=10 mM, $[Fe]_0$=0.65 g/L, [Pd]=0.9 wt% as Fe. pH changes during the reaction: PVDF-PAA-Fe/Pd (7.2→4.0), PVDF-PAA-Fe (6.6 →5.0), PVDF-PAA-iron oxide (6.6 →6.5).

pH dropped significantly, and less than 70 μM of Fe (0.6 wt% of total Fe) and 2.3 μM of Pd (4.2 wt% of total Pd) were dissolved in the solution. With Pd doping, more H_2O_2 was consumed (Figure 4.11B). It could be explained by hydrogenation and/or decomposition of H_2O_2 to water by catalysis of Pd (Okada, Mori et al. 2011). Hence, Pd doping was not preferred in the oxidative step. Both H_2O_2 and biphenyl were degraded slowly with iron oxide, since the rate of free radical generation was highly dependent on the regeneration of Fe (II) from Fe (III) (Pignatello, Oliveros et al. 2006). Iron oxide releases less iron during the decomposition of H_2O_2, and thus will not result in a significant pH drop from dissolved iron. OH• is produced slowly on iron oxide surfaces with less consumption of H_2O_2, and it will benefit the remediation of pollutants in low concentrations such as chloro-organics in contaminated groundwater.

4.6 Intermediates and Byproducts in Biphenyl Oxidation

The direct products in biphenyl oxidation with OH• are hydroxylated biphenyls including 2-, 3- and 4-hydroxybiphenyl (Chen and Schuler 1993). These intermediates can be further oxidized by OH•, forming the secondary products such as dihydroxybiphenyls. Sedlak and Andren detected hydroxychlorobiphenyls and dihydroxylated chlorobiphenyls in aqueous oxidation of 2-chlorobiphenyl by Fenton reaction (Sedlak and Andren 1991). Li et al. reported that biphenyl was successfully oxidized by OH• in chelate-modified Fenton reaction (Li, Bachas et al. 2007). Several intermediates were determined including the aromatic ring cleavage products such as benzoic acid and hydroxybenzoic acid. Therefore, the biphenyl oxidation started with the hydroxylation of aromatic rings, followed by the ring cleavage. If enough oxidants are

provided, the carboxylic acids or even carbon dioxide are expected to be obtained. However, that may not be cost-effective or necessary.

Phenolic compounds usually have low response in GC due to their polarity. The derivatizing agent converts the hydroxyl groups to nonpolar and more volatile groups, allowing the GC analysis. The main peaks shown in Figure 4.12 and Figure 4.13 represent 2-, 3- and 4-hydroxybiphenyl, respectively. 2,2'-Dihydroxybiphenyl (Figure 4.14) and benzoic acid (Figure 4.15) were also identified. The existence of more polar products (such as short chain organic acids) from ring cleavage was not disproven, since they might not be amenable to the solvent extraction and/or GC/MS analysis used in this study. Another four dihydroxybiphenyls and eight trihydroxybiphenyls were tentatively identified (without standards) based on their mass spectra. A typical trihydroxybiphenyl spectrum is shown in Figure 4.16. Those results are consistent with that reported by Halpaap et al (Halpaap, Horning et al. 1978). They detected mono-, di- and trihydroxybiphenyl products during the metabolism of biphenyl in vivo, which were mainly due to the oxidative stress.

Free radicals produced in iron/H_2O_2 system can degrade biphenyl and its oxidation products simultaneously. The intermediates detected in the oxidation are more soluble than biphenyl, and normally have a higher reaction rate with OH• than biphenyl. This results in only a trace amount existing in the solution. To understand the evolution of intermediates during the oxidation, 2-hydroxybiphenyl (0.431 mM), one of the direct products in biphenyl oxidation, was used as the model compound in iron oxide/H_2O_2 system. The oxidation of 2-hycroxybiphenyl with free radicals can be described as a second-order reaction (Valentine and Wang 1998).

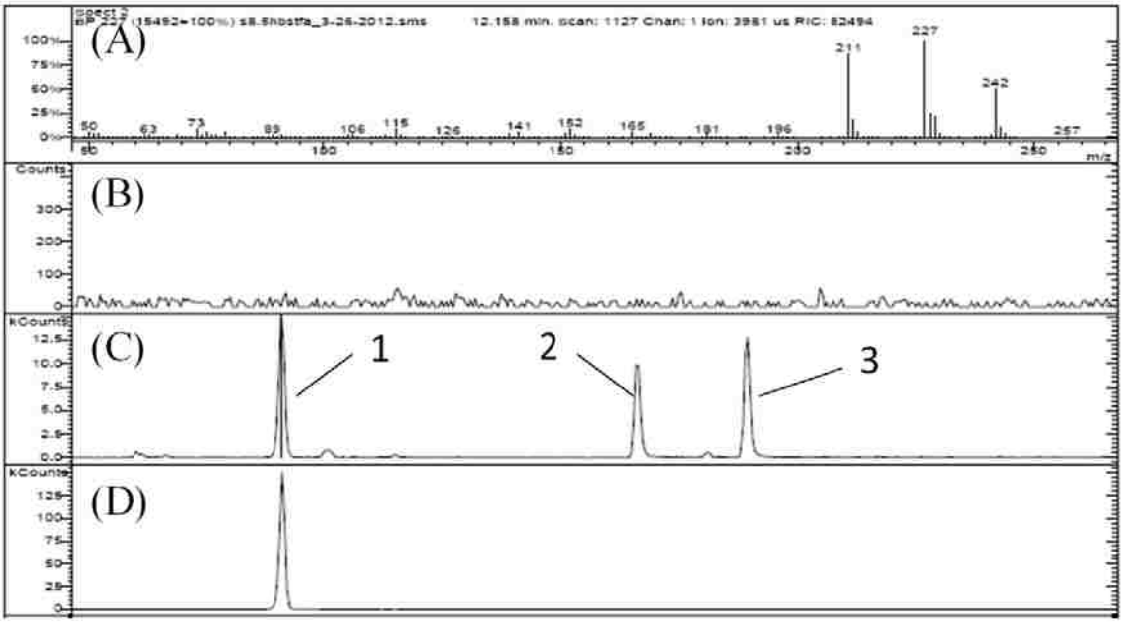

Figure 4.12. 2-Hydroxybiphenyl (BSTFA derivatized) detected in biphenyl oxidation by Fe/Pd immobilized PVDF-PAA membranes (peak 1). (A) Mass spectrum (Selected ion: 227); (B) Chromatograph of BSTFA/Pyridine; (C) Chromatograph of sample; (D) Chromatograph of 2-hydroxybiphenyl standard. Peak 2 and 3 indicate 3- and 4-hydroxybiphenyl, respectively.

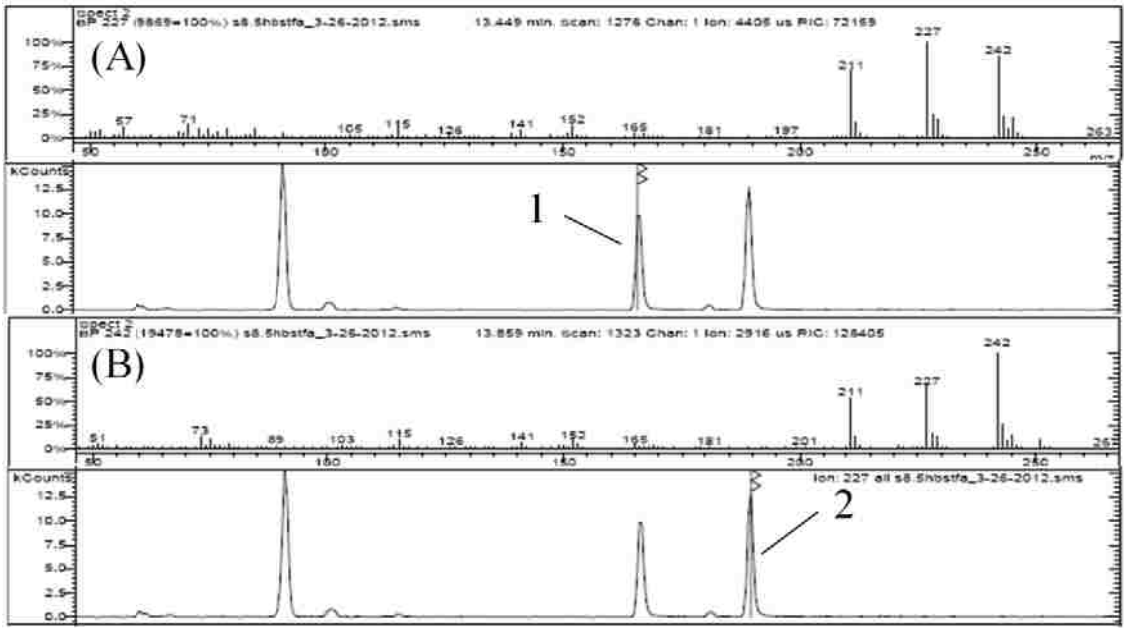

Figure 4.13. Mass spectrum (Selected ion: 227) and chromatograph of tentatively identified (A) 3-hydroxybiphenyl (derivatized, peak 1); (B) 4-hydroxybiphenyl (derivatized, peak 2).

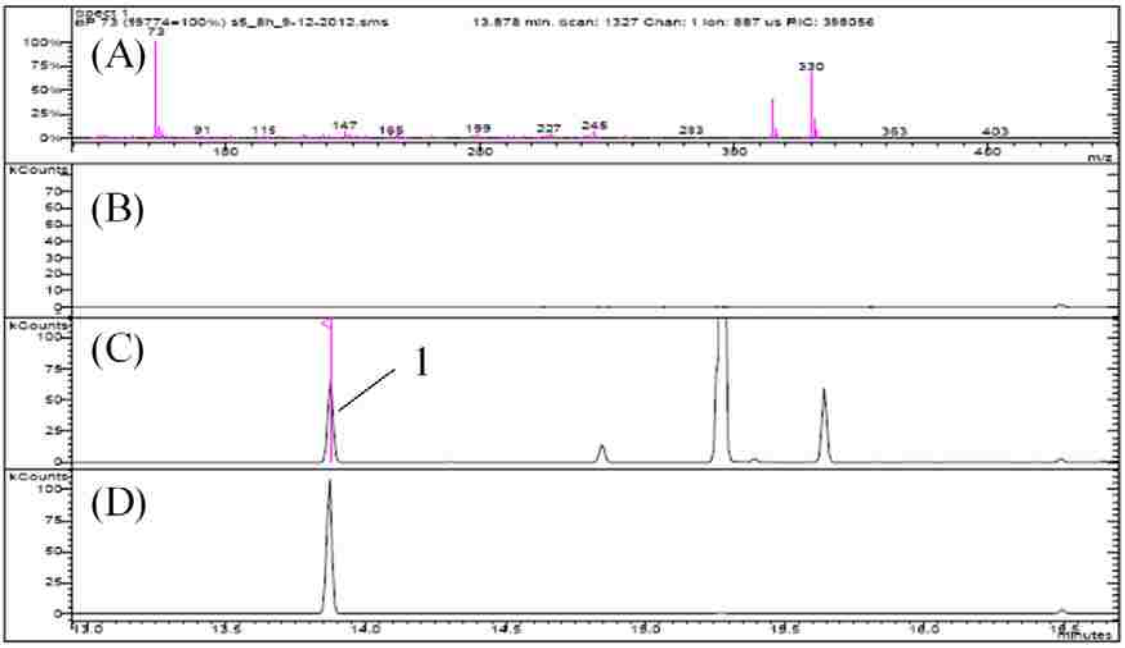

Figure 4.14. 2,2'-Dihydroxybiphenyl (derivatized) detected in biphenyl oxidation by Fe/Pd immobilized PVDF-PAA membranes (peak 1). (A) Mass spectrum (Selected ion: 330); (B) Chromatograph of BSTFA/Pyridine; (C) Chromatograph of sample; (D) Chromatograph of 2,2'-dihydroxybiphenyl standard.

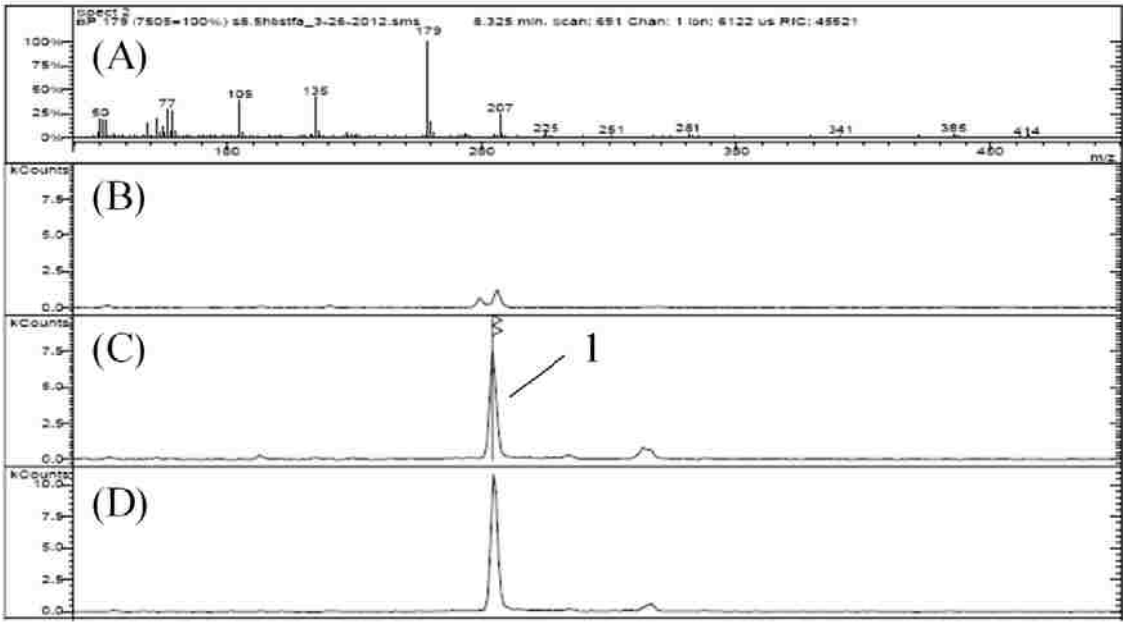

Figure 4.15. Benzoic acid (derivatized) detected in biphenyl oxidation by Fe/Pd immobilized PVDF-PAA membranes (peak 1). (A) Mass spectrum (Selected ion: 179); (B) Chromatograph of BSTFA/Pyridine; (C) Chromatograph of sample; (D) Chromatograph of benzoic acid standard.

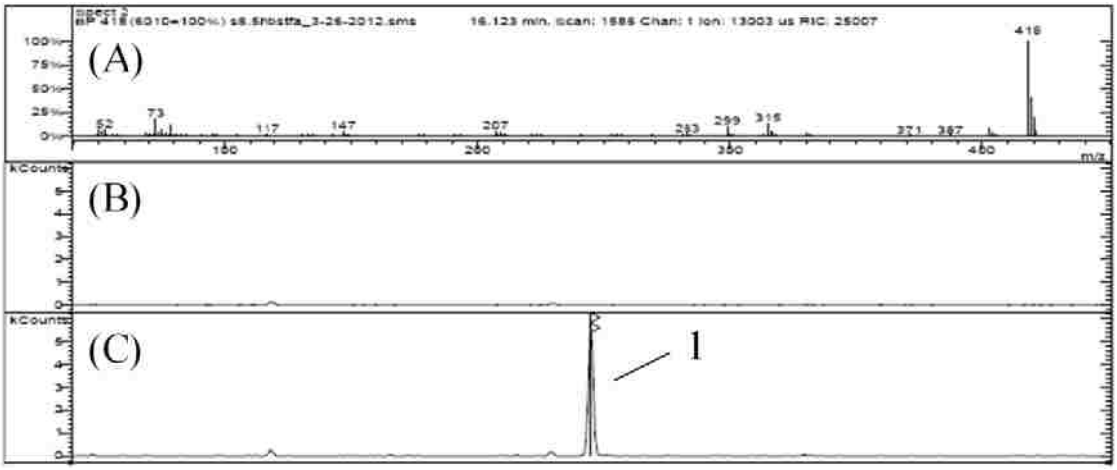

Figure 4.16. Tentatively identified trihydroxybiphenyl (derivatized) detected in biphenyl oxidation by Fe/Pd immobilized PVDF-PAA membranes (peak 1). (A) Mass spectrum (Selected ion: 418); (B) Chromatograph of BSTFA/Pyridine; (C) Chromatograph of sample.

$$-\frac{dC_{2OHBP}}{dt} = k''C_{2OHBP}C_{OH\bullet} \quad \text{(E4.15)}$$

where C_{2OHBP} is the concentration of 2-hydroxybiphenyl in the solution, $C_{OH\bullet}$ is the concentration of OH•, and k''_{2OHBP} is the second-order rate constant. Since H_2O_2 was maintained at a constant concentration (50±7 mM), $C_{OH\bullet}$ could be assumed constant. Therefore, a pseudo-first-order reaction model was obtained.

$$-\frac{dC_{2OHBP}}{dt} = k'C_{2OHBP} \quad \text{(E4.16)}$$

where k'_{2OHBP} is the first-order rate constant ($k'_{2OHBP} = k''_{2OHBP} C_{OH\bullet}$). As shown in Figure 4.17, the oxidation of 2-hydroxybiphenyl fits the pseudo-first-order approximation well (R^2=0.96), and k'_{2OHBP}=0.0504 /h.

All samples were analyzed with the same protocol, and the peak areas of different components were compared. For most compounds, the peak areas increased fast at the beginning, and maintained constant afterwards. This trend again shows that the hydroxylated biphenyls and benzoic acid were indeed the reaction products.

4.7 Free Radical Oxidation Mechanism

Both membrane supported Fe/Pd and Fe show high reactivity with H_2O_2 in free radical generation. A significant pH drop was observed due to the formation of dissolved iron. Similar results were reported in the degradation of bromothymol blue and methyl tert-butyl ether (MTBE) with iron particles (Valentine and Wang 1998; Bergendahl and Thies 2004; Hoag, Collins et al. 2009). Ferrous ions were released at acidic condition (pH=4-7) via iron oxidation with H_2O_2, resulting in the enhanced generation of OH•.

$$Fe + H_2O_2 \rightarrow Fe^{2+} + 2OH^- \quad \text{(E4.17)}$$

$$Fe^{2+} + H_2O_2 \rightarrow Fe^{3+} + OH\bullet + OH^- \quad \text{(E4.18)}$$

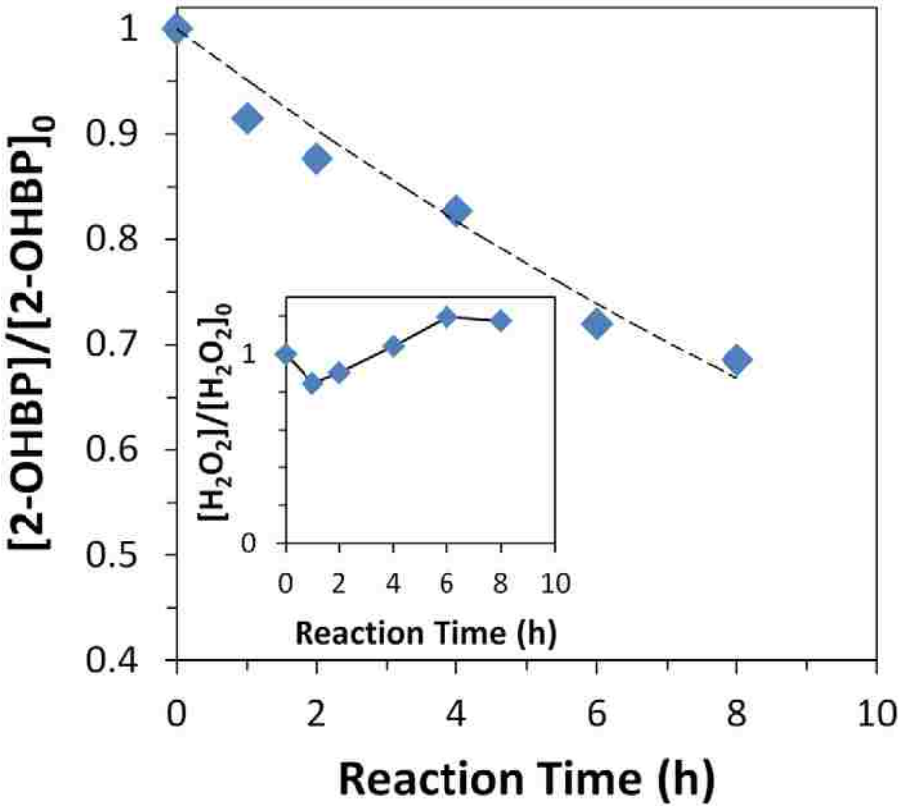

Figure 4.17. 2-Hydroxybiphenyl (2-OHBP) oxidation in iron oxide/H_2O_2 system. The inset was the H_2O_2 concentration during the reaction (maintained constant). [Iron oxide]$_0$=0.5 g/L (BET surface area: 235 m^2/g), [2-OHBP]$_0$=0.43 mM, and [H_2O_2]$_0$=50 mM. pH decreased from 6.9 to 5.1. Dash line shows the pseudo-first-order model fit.

$$Fe(II) + H_2O_2 \rightarrow Fe(III) + OH \bullet + OH^- \quad \text{(E4.19)}$$

$$Fe + O_2 + 2H^+ \rightarrow Fe^{2+} / Fe(II) + H_2O_2 \quad \text{(E4.20)}$$

As ferrous ions released from the iron surface precipitates as iron hydroxides (II, III), heterogeneous Fenton reaction will take place on the iron oxide surfaces (E4.19). The reactive sites on iron oxide surfaces were more efficient than dissolved iron (e.g. Fe^{2+} and Fe^{3+}) in the production of OH• (Bergendahl and Thies 2004; Voinov, Pagan et al. 2011). H_2O_2 can also be generated from iron surfaces directly in oxygenated water (E4.20), and it further reacts with iron/iron oxide to degrade the pollutants via free radical oxidation (Joo, Feitz et al. 2004; Keenan and Sedlak 2008).

To understand the iron/iron oxide transformation during the oxidation, H_2O_2 was continuously added into the freshly made iron suspension under the anaerobic condition (blowing nitrogen gas). The oxidative transformation of iron was monitored with XRD. For freshly made iron, H_2O_2 was consumed instantly with the formation of Fe(II) from iron surfaces. As more H_2O_2 was added, the reaction slowed down (Figure 4.18A). XRD spectra of iron before and after H_2O_2 treatment shows that some iron oxides were formed on iron surfaces (Figure 4.18B). The body-centered cubic α-Fe was mainly converted into magnetite Fe_3O_4, which is one of most reactive iron oxides known in nature. By utilizing the STEM-EELS (line scan and elemental mapping), the morphology and composition changes of iron nanoparticles during H_2O_2 treatment were studied. For freshly made iron, there was an oxide shell about 3-5 nm (Figure 4.19A), which is consistent with the previous report (Nurmi, Tratnyek et al. 2005). After first cycle treatment, the thickness of oxide layer increased to 20-30 nm (Figure 4.19B), and the oxide formed had an amorphous structure, which was mainly nano-aggregates of magnetite based on XRD

results. After six cycle treatment, iron were completely oxidized (Figure 4.19C), and it was hard to differentiate the iron core from iron oxide shell. This shows that anaerobic treatment with H_2O_2 resulted in a transformation from iron to magnetite. Iron oxidation caused the decline of OH• production, but magnetite formed in the oxidation also performed as a catalyst for long-term free radical generation (Watts, Udell et al. 1999; Sun and Lemley 2011). For a full-scale process, membrane modules with exhausted catalysts can be directly replaced by new modules, or regenerated via acid treatment to dissolve iron oxides, followed by ion exchange and reduction to load iron again.

4.8 Functionalized Membrane Applications

Iron/iron oxide embedded microfiltration membranes have the potential to enhance the degradation efficiency of contaminant in water with a combined reductive and oxidative treatment. In real applications, membrane modules such as spiral wound and hollow fiber modules can be used. PCBs are reduced to biphenyl when passing through the first membrane module (PVDF-PAA-Fe/Pd), followed by mixing with H_2O_2 and subsequent oxidation of biphenyl in the second module (PVDF-PAA-Fe or Fe_xO_y). Each module is accompanied by a circulating device to achieve high conversions. H_2O_2 can be continuously supplied by another module with enzyme (e.g. glucose oxidase) immobilized via layer-by-layer assembly (Datta, Cecil et al. 2008). This reactive membrane platform can enhance the reactivity of particles (no aggregation), while eliminating the formation of chlorinated byproducts in the direct oxidation with free radicals.

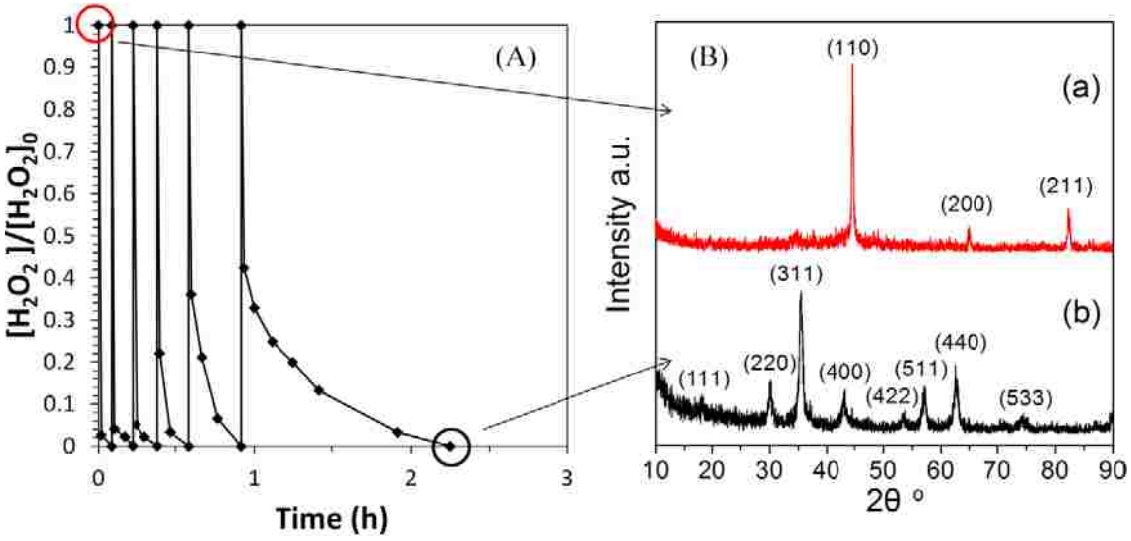

Figure 4.18. H_2O_2 decomposition with Fe nanoparticles (6 cycles). (A) H_2O_2 degradation; (B) iron transformation during H_2O_2 treatment. XRD spectra of Fe nanoparticles before and after H_2O_2 treatment are shown in (a) and (b), respectively. $[Fe]_0$=20 mM, $[H_2O_2]_0$=4.4 mM (each cycle), V=200 mL, pH=7.0-7.2. BET surface area (m^2/g): 37.8 (Fe^0) and 53.0 (Fe_3O_4).

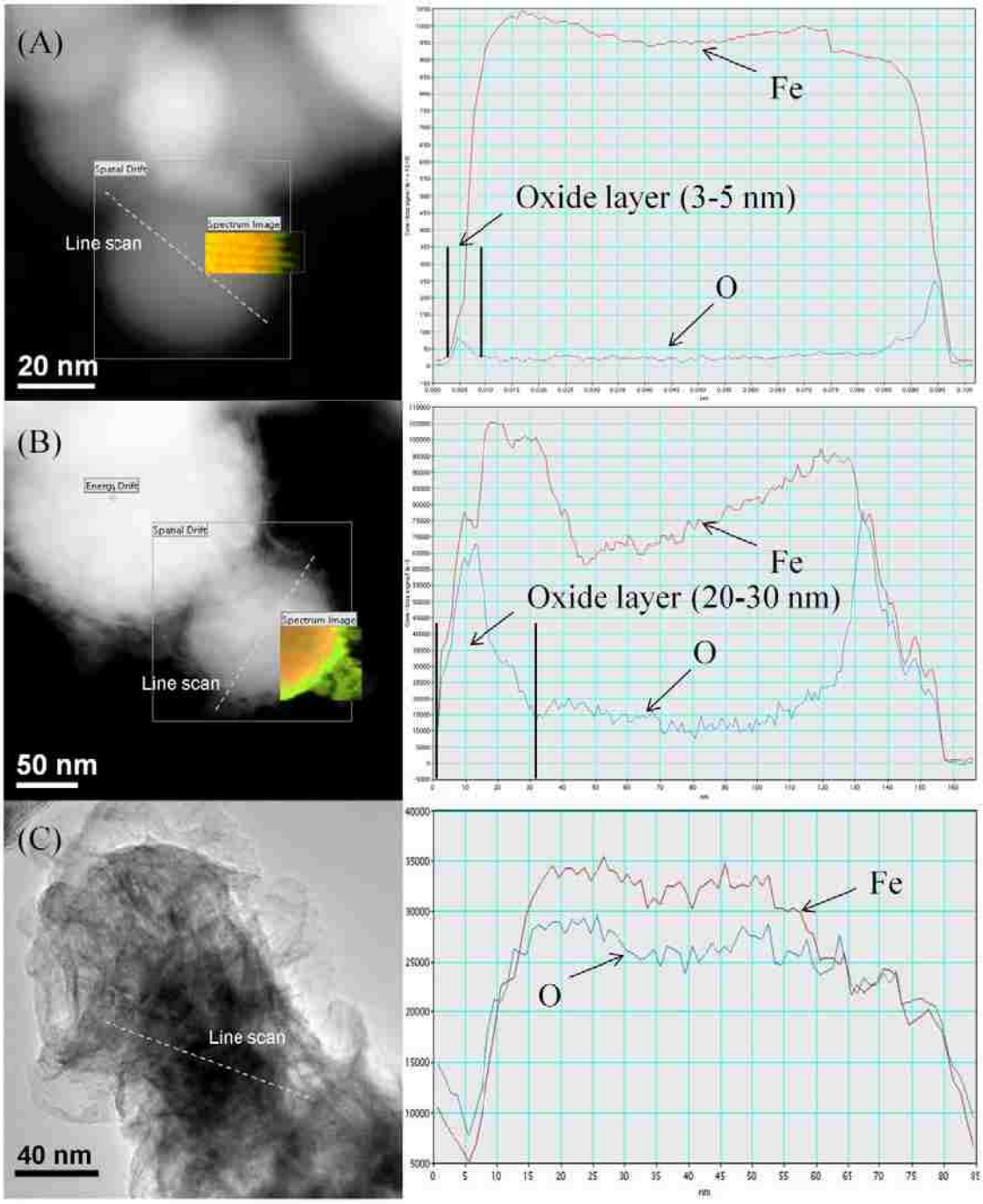

Figure 4.19. STEM-EELS line scan and elemental mapping of Fe nanoparticles during H_2O_2 oxidation. (A) Freshly made Fe^0; (B) Fe after H_2O_2 treatment (1 cycle); (C) Fe after H_2O_2 treatment (6 cycles). Yellow color indicates Fe and green color indicates O.

Chapter Five Engineered Iron/Iron Oxide Functionalized Membranes for Toxic Metal Removal

The removal of toxic metals and organics from water with high concentrations of salt has been an emerging area for membrane separation. Cost-effective nanomaterials such as iron and iron oxide nanoparticles have been widely used in reductive and oxidative degradation of chlorinated organic compounds. Similar procedures can be used for metal species change (e.g. metal oxyanions to elemental metal), and/or adsorption of species on iron oxide surface. In this chapter, iron functionalized membranes were developed for removal of selenium from scrubber water. To prevent the particle aggregation and reduce dissolved iron, polyacrylic acid (PAA) coated polyvinylidene fluoride (PVDF) membranes were developed in both lab-scale and full-scale for in-situ synthesis of iron. Water permeability of membrane decreased rapidly as membrane weight gain increased, and the highest ion exchange capacity (IEC) was obtained at weight gain around 20 % with highly pH responsive pores. By integration of nanofiltration (NF) and iron functionalized membranes, the interferences of sulfate and chloride in scrubber water were significantly reduced, and selenium concentration below 10 μg/L was achieved. Iron nanoparticles were also successfully synthesized in full-scale membrane module for selenium removal. The graphic abstract of Chapter Five is shown in Figure 5.1.

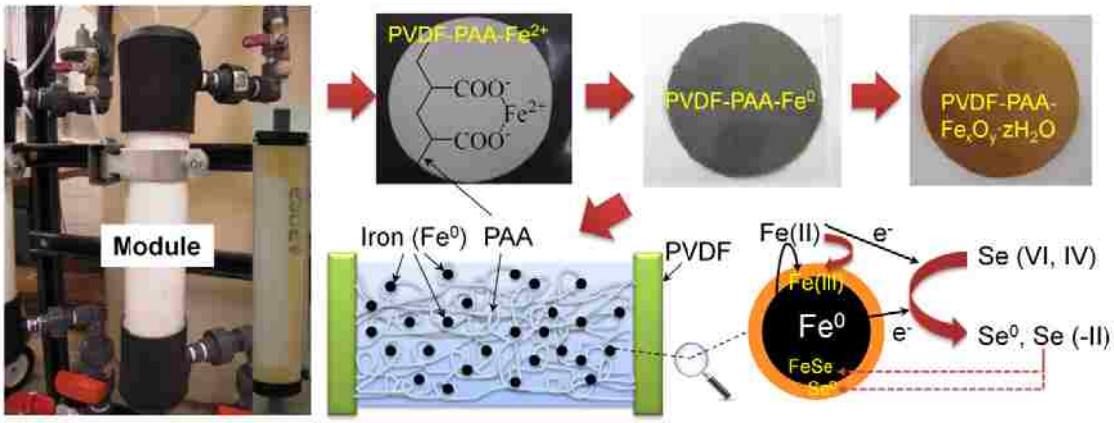

Figure 5.1. Graphic abstract of Chapter Five.

In Chapter Three and Chapter Four, PVDF-PAA functionalized membrane supported iron and iron oxide nanoparticles have shown promising results for chloro-organic degradation in groundwater remediation. In this chapter, the functionalized membrane technology is transferred to toxic metal removal for coal-fired power plant scrubber water application. It begins with an introduction to the existing technologies for toxic organic and metal removal from water containing high total dissolved solids (TDS), especially membrane separation and nanotechnology. Next, it focuses on the study of the effects of PAA functionalization on membrane transport, pH responsive behavior and ion exchange capacity. This is followed by discussion of selenium removal results in lab-scale iron functionalized membranes. The membrane reactivity is evaluated in DI water, synthetic salt water and real scrubber water. Water matrix and temperature effects on removal efficiency are discussed. Finally, the first reported iron synthesis in full-scale membrane module and successful selenium removal from scrubber water are highlighted.

5.1 Introduction

Various water sources contain toxic ingredients such as chlorinated organic compounds and heavy metals. Those contaminants are either recalcitrant to environmental degradation, or existing with high concentrations of total dissolved solids (TDS) like salts, which make them difficult to treat.

Membrane technologies allow the separation of solutes in water based on size exclusion, charge exclusion and diffusivity/solubility difference. Commercial membranes such as reserve osmosis (RO) and nanofiltration (NF) membranes have been extensively used for water softening and desalination (Elimelech and Phillip 2011). However, RO and NF membranes are not effective in removing some chlorination by-products such as

trichloroethylene (TCE), carbon tetrachloride, and dichlorobenzene, which have high solubility in membrane synthesis materials. Instead, the pretreatment of water with activated carbon filtration is often required. Additionally, the concentrated contaminants in the retentate need further treatment. Other existed technologies such as physical and biological treatment are either energy or capital intensive. One of the most promising ways to remove chlorinated organics from water is chemical remediation, including reductive and oxidative degradation with iron and iron oxide particles.

Iron nanoparticles made by borohydride or polyphenol reduction are most commonly used materials in chlorinated organic dechlorination (Zhang 2003; He and Zhao 2008; Hoag, Collins et al. 2009; Smuleac, Varma et al. 2011). With a second metal coating such as Fe/Pd and Fe/Ni, more rapid and complete hydrodechlorination can be achieved (Wang and Zhang 1997; Tee, Bachas et al. 2009). Alternatively, chloro-organics can be destructed by oxidation of hydroxyl radicals (OH•) from iron oxide catalyzed hydrogen peroxide decomposition (Pignatello, Oliveros et al. 2006; Xue, Hanna et al. 2009; Lewis, Datta et al. 2011; Gui, Smuleac et al. 2012). However, the aggregation and leaching of nanoparticles in direct injection are two main issues facing us, and the use of engineered nanomaterials already raised public concerns about their potential toxicity (Auffan, Rose et al. 2009; Lowry, Gregory et al. 2012; Schug, Johnson et al. 2013).

One possible solution is to synthesize nanoparticles through ion exchange or adsorption of precursor ions on porous substrates such as silica (Zheng, Zhan et al. 2008), activated carbon/carbon nanotubes (Tseng, Su et al. 2011), and polyelectrolyte pore-filled membranes (Winnik, Morneau et al. 1998; Kim, Hong et al. 2008; Lewis, Datta et al.

2011), followed by reduction. The functional groups on those substrates can eliminate the aggregation during the particle formation and release issues to environment, and allow the control of particles size (Xu and Bhattacharyya 2005; Huang, Shi et al. 2008). In our group, polyacrylic acid (PAA) functionalized polyvinylidene fluoride (PVDF) membrane with iron/iron oxide nanoparticles was developed for combined reductive and oxidative degradation of polychlorinated biphenyls (PCBs) (Gui, Ormsbee et al. 2013).

Our latest efforts focused on developing the full-scale functionalized membrane for groundwater remediation. The same membrane can be used for toxic metal removal, such as selenium oxyanion removal in scrubber water from coal-fired power plants. Selenium is an essential element in human and animal nutrition (Yoon, Kim et al. 2011), but it turns out to be toxic at high level due to its interaction with body tissue. Therefore, the control of selenium release to environment from mining, oil refineries, manufacturing and agriculture drainage has been a critical issue (Lalvani 2004; Lemly 2004). Iron has been reported to reduce selenate (VI) and selenite (IV) to elemental selenium (Se^0) and selenide (-II) (Mondal, Jegadeesan et al. 2004; Olegario, Yee et al. 2010; Yoon, Kim et al. 2011). However, most studies were conducted in iron particle suspension without the use of stabilizers.

5.2 Membrane Surface Characterization

To prove that PVDF membrane pores were successfully functionalized with PAA, XPS depth profile analysis was conducted from membrane top surface to pore region. The atomic percent (N, O, C and F) of functionalized membrane is shown in Figure 5.2A. On the top surface (etch time 0 s), F and O content were 2.5% and 31.9% respectively, compared to 42.5% and 2.7% for the pristine PVDF400HE membrane. As the ion beam

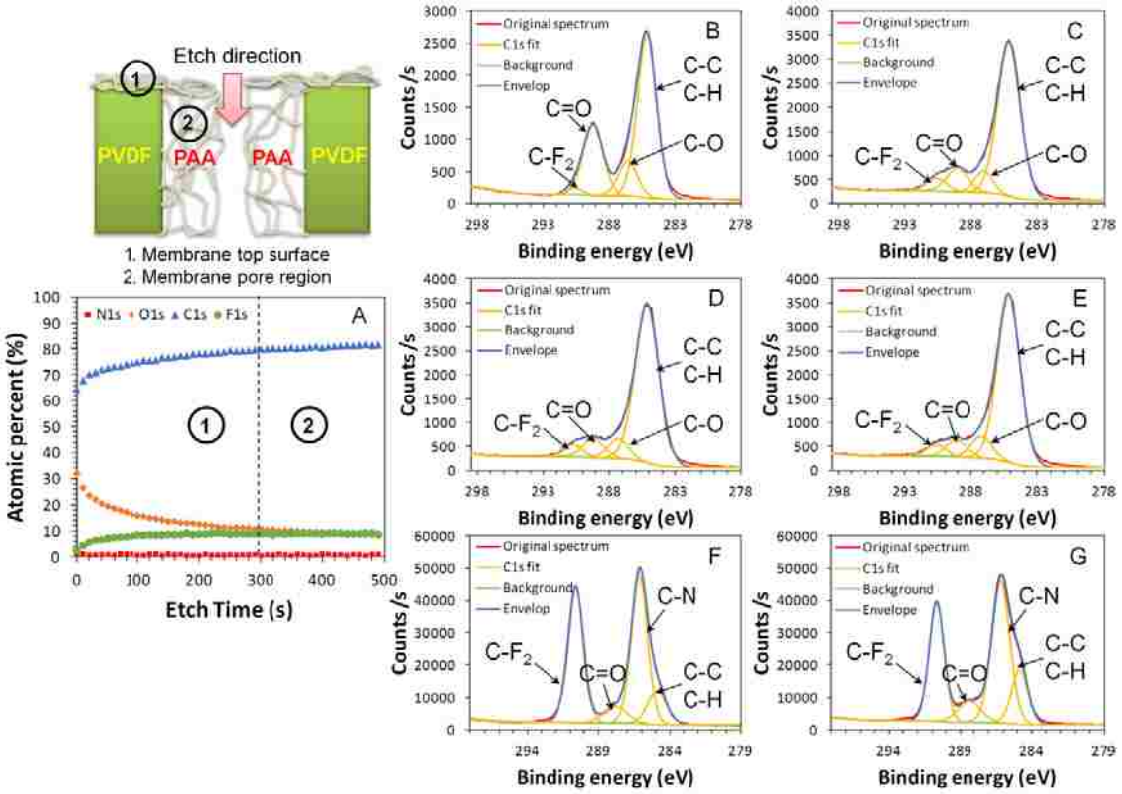

Figure 5.2. XPS depth profile analysis of functionalized membrane (PVDF400HE-PAA, 12.5% membrane weight gain). (A) Atomic percent profile; High resolution C1s spectra at etch time (B) t=0 s, (C) t=200 s, (D) t=300 s, (E) t=490 s. Ion beam energy: 200 eV (high), etch speed: 10 s/level, 0.07nm/s as Ta_2O_5. Number 1 and 2 show the regions of membrane top surface and pore, respectively. XPS spectra of full-scale PVDF400HE and functionalized membrane made by Ultura are shown in (F) and (G).

etching started, F content increased quickly while O content declined as approaching the pore region. The depth profile results clearly show that there was a thin layer of PAA above PVDF membrane. High resolution C1s spectra (Figure 5.2B) further proved that the top surface was covered with PAA as evidenced by C-O (286.7 eV) and C=O (289.0 eV) peaks from carboxyl groups with a tiny C-F_2 peak near 290.8 eV. The intensity of C-O and C=O peaks declined quickly from 0 s to 200 s (Figure 5.2C) with the rise of F content to 8.75%. The spectra at 300 s (Figure 5.2D) and 490 s (Figure 5.2E) were identical with the exactly same elemental composition, showing the ion beam penetrated the PAA layer, and reached the uniformly functionalized pore region.

An ideal functionalized membrane will have PAA in the pores instead of on the top surface. However, PAA formation near the pore mouth always happened due to the residual polymerization solution from dip coating. This thin layer reduced the membrane porosity significantly. During the manufacturing of full-scale functionalized membranes, the polymerization solution was pulled through PVDF membranes by applying vacuum from the backing side, followed by surface cleaning with air knife. This improvement indeed removed the accumulated polymerization solution above pores effectively. XPS spectrum of full-scale functionalized membrane (Figure 5.2G) shows similar C-F_2 and C-N peaks as PVDF membrane substrate (Figure 5.2F), since little PAA was formed on top of PVDF membrane. C-N peak could be from the cross-linker or additives during PVDF membrane formation such as polyvinylpyrrolidone (PVP). C=O peak was stronger in functionalized membrane due to PAA formation inside. As expected, the full-scale functionalized membrane had higher F/C ratio from PVDF substrate and lower O/C ratio from PAA coating than lab-scale one (Table 5.1). The main carbon source of

Table 5.1. XPS surface analysis results of pristine PVDF, PAA functionalized PVDF (PVDF400HE-PAA) and iron/iron oxide immobilized PVDF-PAA membranes (PVDF400HE-PAA-Fe/Fe(OH)$_x$).

Membranes	Atomic Ratio				Carbon Balance	Value of x in Fe(OH)$_x$
	F/C	O/C	N/C	Fe/C		
PVDF400HE (Ultura)	0.79	0.05	0.02	N/A	0.93	N/A
PVDF400HE-PAA (Ultura)	0.53	0.11	0.03	N/A	0.83	N/A
DVPP 14250 (Millipore)	0.50	0.26	0.005	N/A	0.88	N/A
PVDF400HE-PAA[a]	0.04	0.51	0.02	N/A	0.88	N/A
PVDF400HE-PAA-Fe after Se reduction in DIUF water[a]	0.22	0.65	0.04	0.16	0.68 (x=3)/ 1.39 (x=0)	1.66
PVDF400HE-PAA-Fe after Se reduction in synthetic water with $CaCl_2$ (75 mM)[b]	0.19	2.66	0.05	0.89	0.37 (x=3)/ 4.39 (x=0)	2.53
PVDF400HE-PAA-Fe after Se reduction in synthetic water with $MgSO_4$ (30 mM)[b]	0.21	2.62	0.03	1.03	0 (x=3)/ 4.28 (x=0)	2.12

[a]12.5% membrane weight gain; [b]20.7% membrane weight gain. x values were obtained by assuming the carbon balance. DVPP 14250 (Millipore) is hydrophilized PVDF membrane with cross-linked polyacrylate coating (average pore size: 650 nm, thickness: 125 μm). The coating was considered as PAA here for carbon balance calculation.

functionalized membrane included PVDF (F/C=1/1), PAA (O/C=2/3), and PVP (N/O/C=1:1:6). The carbon balance of full-scale PVDF400HE-PAA (Ultura) was close to commercial PVDF400HE and DVPP14250, showing the successful scale-up of functionalized membranes without blocking the pores. For iron/iron oxide immobilized membranes, iron can exist in multiple valence states, depending on the oxidation time and water pH. If $Fe(OH)_x$ is the overall formula of reacted particle, the value of x could vary from 0 (pure iron) to 3 (fully oxidized iron). With the carbon balance assumption, x fell between 1.5 and 3, suggesting iron was partially oxidized after selenium removal.

5.3 Functionalized Membrane Properties

5.3.1 Membrane Permeability with Weight Gain

The weight gain of functionalized membrane is defined as the ratio of dry weight difference through in-situ polymerization to the weight of pristine PVDF membrane.

$$Weight\ gain = \frac{W' - W_0}{W_0} \times 100\% \qquad \text{(E5.1)}$$

where W_0 and W' are the weight of membrane before and after functionalization, respectively. It should be noted that the weight of backing was also included in W_0 since the control experiment shows that PAA was also formed in the nonwoven backing due to its porous structure. The weight gain of PVDF400HE membrane increased linearly with the concentrations of monomer in polymerization solution (Figure 5.3A). Meanwhile water permeability of membrane dropped rapidly. From 2.2% to 36.3% weight gain, water permeability declined from 1220 LMH/bar to 1.9 LMH/bar at pH 3. It was mainly due to the decrease of membrane pore volume or effective pore size. With more polymer incorporated in pores, the polymer network has less porosity between segments, resulting

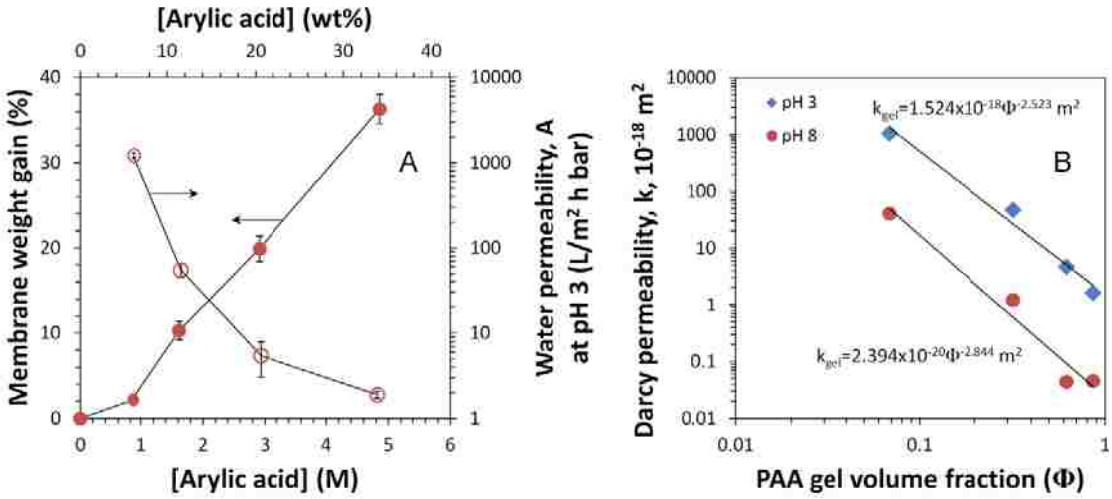

Figure 5.3. (A) Weight gain and water permeability of functionalized membranes (PVDF400HE-PAA) with concentrations of acrylic acid in polymerization; (B) Darcy permeability of pore-filled membrane as a function of polymer gel volume fraction at pH 3 and 8.Water permeability of PVDF400HE (Ultura) is 7512±125 L/(m^2·h·bar).

in denser material.

The membrane permeability is dependent on the property of cross-linked gel formed in pores. Darcy permeability of gel (k_{gel}, m^2) is related to membrane permeability (k_m, m^2) as,

$$k_{gel} = k_m /(\varepsilon_S / \tau_S) \tag{E5.2}$$

where ε_s is the porosity of substrate PVDF membrane, τ_s is the tortuosity of membrane. The porosity of PVDF400HE membrane is 0.5±0.05 according to manufacturer, and was further confirmed by SEM image of membrane top surface. τ_s can be obtained from Kozeny constant,

$$\tau_S = K_S / K^* \tag{E5.3}$$

where K_S=5 for a substrate membrane with porosity around 2/3, and K^*=2 with the assumption of parallel capillary-type pores of circular cross-section (Kapur, Charkoudian et al. 1996; Mika and Childs 2001). k_m can be calculated from the following equations,

$$k_m = \frac{J_w \eta}{\Delta P / L} \tag{E5.4}$$

$$J_w = Q / A_m \tag{E5.5}$$

where J_w is the water flux through the functionalized membrane, Q is the water volume flow rate, A_m is the membrane area (13.2 cm^2), L is the thickness of PVDF (70±5 μm) measured with cross-sectional image obtained in SEM, η is the dynamic water viscosity (0.89 mPa·s at 25 °C), and ΔP is the transmembrane pressure.

The gel volume fraction of functionalized membranes (Φ) is defined as the ratio of gel volume (V_{gel}) to total membrane pore volume (V_m). It can be estimated by

$$\phi = \frac{(W' - W_0)/\rho_{gel}}{A_m L \varepsilon_S} \quad \text{(E5.6)}$$

where ρ_{gel} is the density of PAA hydrogel in membrane pores. The volume and weight of PAA gel obtained in solution polymerization were measured, and the density was calculated to be 1.21±0.1 g/cm^3, which was close to reported value of uncross-linked PAA (1.37 g/cm^3) (Brandrup 2003). The gel volume fraction of membranes is proportional to the weight gain from polymerization, increasing from 0.069 (2.2%) to 0.862 (36.3%). The gel Darcy permeability obtained at pH 3 and 8 (Figure 5.3B) can be fit in a power law similar to previous studies, with a correlation coefficient R^2=0.981 ($k_{gel} = 1.524 \times 10^{-18} \phi^{-2.523} m^2$) at pH 3 and R^2=0.965 ($k_{gel} = 2.394 \times 10^{-20} \phi^{-2.844} m^2$) at pH 8. The exponent on Φ represents the rate of permeability change with the gel volume fraction. When pH increased from 3 to 8 with the same gel, the exponent varied within 12.7%, proving the excellent stability of PAA gel.

Darcy permeability of PAA gel synthesized in aqueous phase decreased faster with gel volume increase than previous study (Hu and Dickson 2007). The aqueous polymerization used here might cause greater gel heterogeneity, result in a larger exponent of Φ. Generally, free radical polymerization of acrylic acid in aqueous phase has a higher propagation rate than that in organic phase or in organic/water mixture. Water can enhance the reactivity of monomer and free radicals by solvation (Gromov, Galperina et al. 1980; Beuermann 2002). Looser polymer coils were formed in water, and they could facilitate the water and monomer transport, resulting in high concentration of monomer near the active growing center. While in organic phase, denser PAA coils could limit the entrance of monomer. Additionally, hydrogen bonding might also enhance the

polymerization by creating complexes between monomers, oligomers, and water (Chapiro and Mankowski 1981). Therefore, gel formed in aqueous phase may not be as uniform as that made in organic phase, but it should give higher water permeability due to the formation of loose polymer segments. This is indeed the case. Gel permeability at Φ=0.1 was enhanced by 53 time at pH 8, and 510 times at pH 3, compared to gel synthesized at cross-linking degree of 4 mol% in 1-propanol (50 wt%) (Hu and Dickson 2007). PVDF400HE membrane used here has a thinner PVDF layer (70±5 μm) with highly porous non-woven backing. This composite structure also enhanced the water permeability. Those benefits allow more PAA incorporated in membrane pores for nanoparticle synthesis.

The gel permeability at pH 3 is about 63 times higher than that at pH 8 when Φ=1, while this ratio decreased to 30 times when Φ=0.1. This significant difference indicates that the gel permeability was also related to the swelling of PAA with environmental pH, which can be the control factor when Φ>0.1.

5.3.2 pH Responsive Behavior with Weight Gain and Its Applications

PAA is well-known for its pH responsive (swelling/deswelling) behavior due to the reversible protonation and deprotonation of carboxyl groups with water pH variation. The acid dissociation constant (pKa) of PAA is usually around 4.2-4.9. At very low pH, carboxyl groups are in compact state without ionization. With pH increasing, carboxyl groups start the deprotonation accompanied by ion exchange with cations in water. The mesh size of PAA hydrogel also increased at high pH, resulting in higher swelling ratio. Our recent study shows that PAA synthesized through thermal polymerization had a swelling ratio around 2 at pH 2 and 17 at pH 9 (Hernandez, Papp et al. 2014). With PAA

incorporated in membrane pores as a "smart" valve, one can manipulate the water permeability of membranes by adjusting the water pH (Lewis, Datta et al. 2011).

The fraction of ionized carboxyl groups (degree of dissociation) with water pH can be estimated by,

$$Degree\ of\ \ dissociation = \frac{[COO^-]}{[COO^-]+[COOH]} \times 100\% \qquad \text{(E5.7)}$$

where [COO^-] and [COOH] are concentrations of ionized and unionized carboxyl groups, respectively. They can be calculated from Henderson-Hasselbach equation,

$$pH = pK_a + Log_{10}([COO^-]/[COOH]) \qquad \text{(E5.8)}$$

At pH 3, only 3.07% of carboxyl groups were ionized (assume pKa=4.5), while they are fully deprotonated (99.97%) at pH 8. Water flux ratio ($J_{w,\ pH=3}/J_{w,\ pH=8}$) increased as the amount of carboxyl groups increased, and reached as high as 92±21 with 0.49 mmol carboxyl groups (19.9% weight gains) incorporated in functionalized membranes. As the amount of carboxyl groups continued to grow to 0.89 mmol (36.3% weight gain), Water permeability was only 1.9 L/(m^2·h·bar) at pH 3, since membrane pores had been filled up with PAA gel. Due to the limited space in pores, some swollen gel was excluded from pores, and anchored at the pore mouth with low stability under the applied pressure. Some entangled gel was also observed on the top surface of membranes. With pH increasing and gel swelling, the gel homogeneity increased. However, the reduced draining region between polymer segments limited the gel swelling, resulting in a lower flux ratio at higher weight gain (36.3%).

Similar pH valve effect of PAA functionalized membranes was also reported by Hu et.al, with valve ratio up to 112 (Hu and Dickson 2007). At the same gel volume

fraction ($\Phi<0.1$), higher cross-linking degree created more heterogeneity and higher elastic modulus in polymer segments, resulting in higher water permeability and swelling ratio. In our study, the gel volume fraction was mainly higher than 0.1 ($0.069<\Phi<0.862$), indicating the formation of less heterogeneous polymer network via overlapping and interpenetration.

The flux modulation of three full-scale functionalized membranes with pH proves the successful scale-up of PAA functionalized PVDF membrane (Figure 5.4 inset). As expected, the spongy PVDF membranes got more PAA inside due to its larger pore volume.

5.3.3 Ion Exchange Capacity (IEC) of Functionalized Membranes

During the ion exchange process, the deporotonated carboxyl groups in PAA chains chelate with Fe^{2+} (molar ratio 2:1). Fe^{2+} can also be absorbed by carboxyl groups (molar ratio 1:1) through electrostatic binding. Ion exchange capacity of functionalized membranes varied from 0.60 to 7.57 meq/g PVDF, depending on the amount of carboxyl groups in membrane pores (Figure 5.4). The swelling of polymer led to the overlapping and interpenetration of polymer chains, and the diffusivity of ions in swelling gel was much lower than that in bulk. It explains why carboxyl groups were not fully utilized during ion exchange. The obtained IEC values were about 30% less than calculated values based on the membrane weight gain.

Higher amount of carboxyl groups in pores did not necessarily result in higher IEC. As the amount of PAA increased, some swollen gel came out of pores and lost the stability, as evidenced by ion exchange results of membrane with high PAA loading (0.89 mmol) (Figure 5.4). For full-scale functionalized membrane synthesis, membranes weight

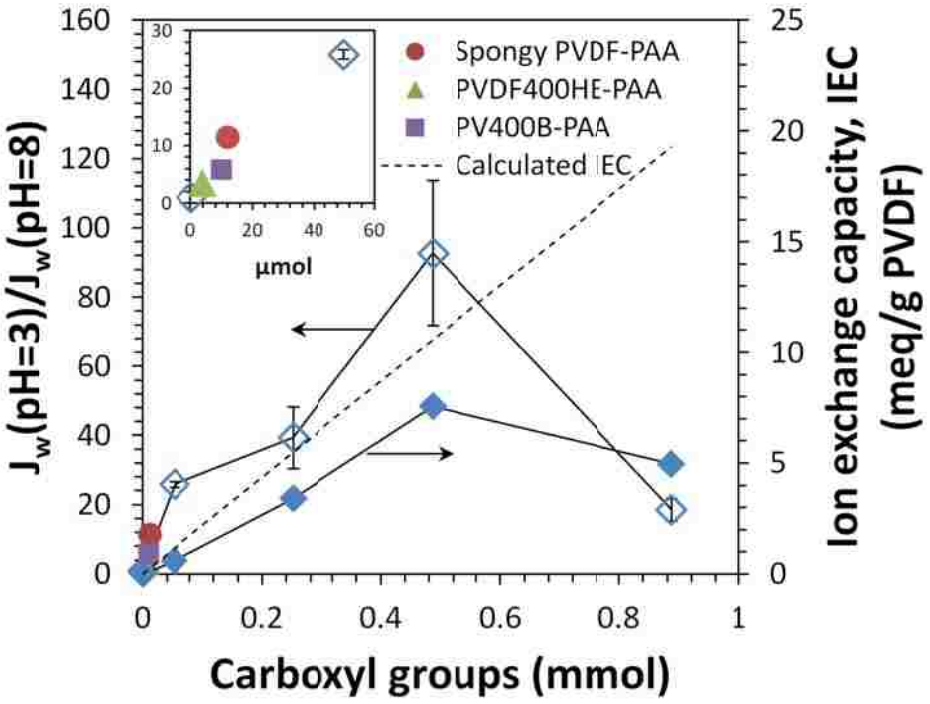

Figure 5.4. Water flux ratio (at pH=3 and pH=8) and ion exchange capacity (IEC) with total amount of carboxyl groups from functionalization. Three full-scale membranes (Spongy PVDF-PAA, PVDF400HE-PAA and PV400B-PAA) are shown in the inset, where the amount of carboxyl groups is calculated from ion exchange studies.

gain between 10% and 20% provided the advantages of a high swelling ratio and ion exchange capacity without sacrificing too much water permeability.

5.3.4 Nanoparticle Size Control

PAA acted as a stabilizer of iron precursor in nanoparticle synthesis, and also controlled the particle size. With PAA incorporated in membrane pores, both the rates of nucleation and particle growth were retarded. The aggregate formation during the particle growth can be effectively reduced as evidenced by SEM images (Figure 5.5). A higher molar ratio of carboxyl groups to ferrous ions resulted in smaller particle size and higher specific surface area. This property suggests the potential of using the functionalized membranes as a stabilizer to manipulate the nanoparticles reactivity via size control.

5.4 Selenium Oxyanion Removal

With iron as an electron donor, selenate was reduced to selenite and elemental selenium (Se^0). In reducing environment, iron selenide formation was also reported (Myneni, Tokunaga et al. 1997; Scheinost and Charlet 2008; Olegario, Yee et al. 2010; Yoon, Kim et al. 2011). Following are the possible reactions of selenium oxyanions with iron.

$$Fe^0 + SeO_4^{2-} + H_2O \rightarrow Fe^{2+} + SeO_3^{2-} + 2OH^-; E_0 = 0.497V \quad \text{(E5.9)}$$

$$3Fe^0 + SeO_4^{2-} + 4H_2O \rightarrow Se^0(s) + 3Fe^{2+} + 8OH^-; E_0 = 1.025V \quad \text{(E5.10)}$$

$$Fe^0 + Se^0(s) \rightarrow Se^{2-} + Fe^{2+}; E_0 = \text{-}0.477V \quad \text{(E5.11)}$$

Ferrous ions released from iron surfaces will precipitate as hydroxides containing Fe(II) at near neutral pH. This increasing oxide layer creates more resistance for reactants to transfer from bulk solution to iron surfaces. Eventually, iron will be consumed completely. Low pH will benefit the reduction by minimizing the formation of iron

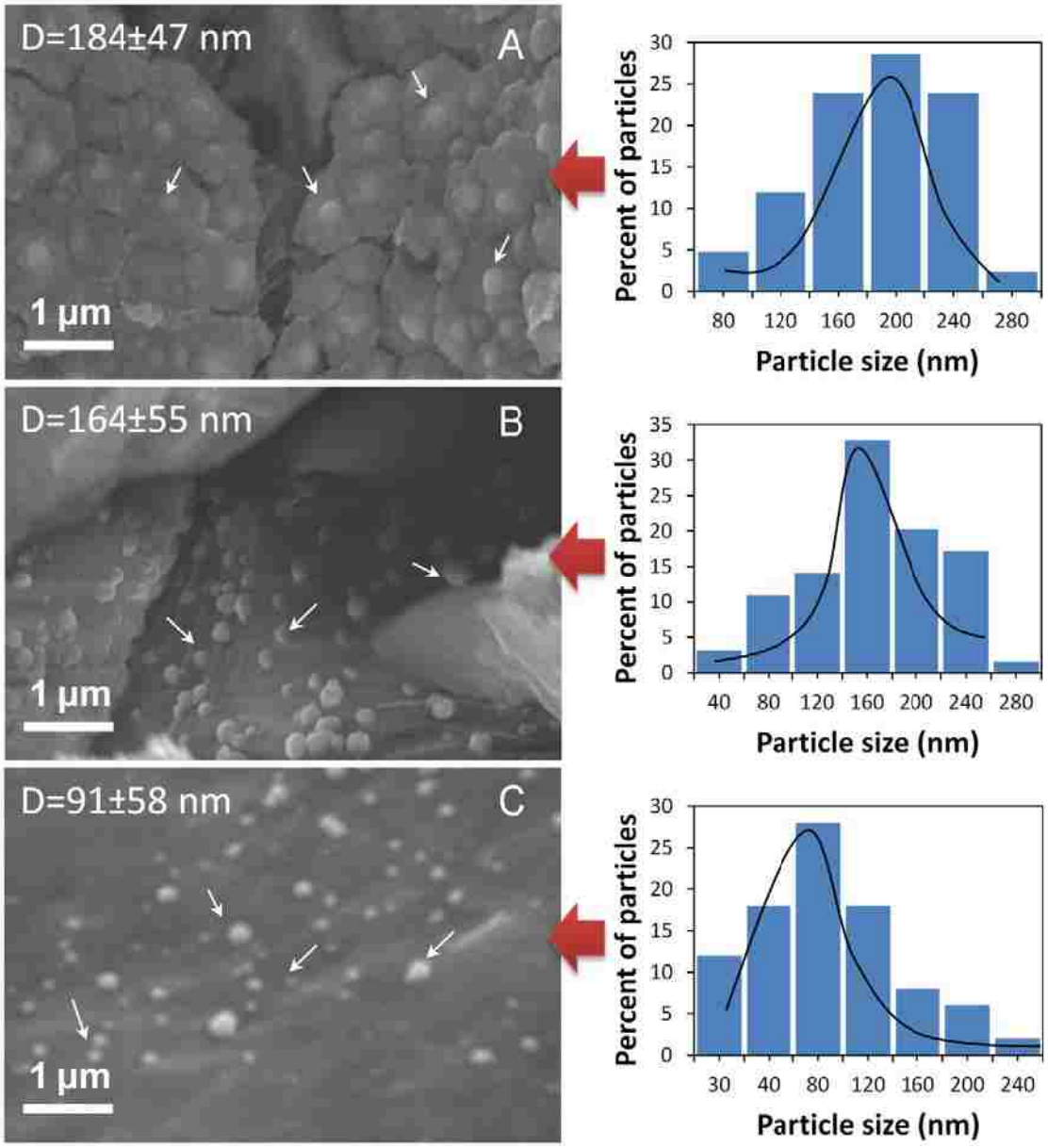

Figure 5.5. SEM images and particle size distribution of iron nanoparticles synthesized in functionalized membranes with molar ratio of carboxyl groups to Fe^{2+} as 1.8 (A), 2.8 (B), and 3.2 (C). D is the average particle size. White arrows indicate the nanoparticles.

hydroxide (Klas and Kirk 2013).

5.4.1 Effect of TDS in Water

Selenium oxyanion reduction with iron follows a pseudo-first-order law ($d[Se]/dt = -k_{obs,Se}[Se]$), where [Se] is the selenium concentration, and $k_{obs,Se}$ (observed reaction rate) is related to the particle loading and specific surface area. It is used to compare the reactivity of same iron nanoparticles in different water matrix. The average particle size synthesized in aqueous phase is 20±0.2 nm based on the obtained BET specific surface area (37.8 m^2/g). The same feed solution (2 mg/L as Se) was used in DI and synthetic water experiments. The concentration of selenate in DI water (pH 4.5) decreased to less than 5 μg/L within 10 minutes in the presence of iron (0.5 g/L). Iron nanoparticles maintained the reactivity with five cycle treatment, and $k_{obs,Se}$ in DI water (32.8 h^{-1}), which is 160 times higher than that obtained in scrubber water (0.204 h^{-1}).

Based on speciation results, selenium in scrubber water existed in the form of selenate (49.9%), selenite (48.3%) and methylseleninic acid (MeSe, 1.8%). The scrubber water mainly contains cations such as Ca^{2+} (90±10 mM), Mg^{2+} (30±3 mM), and Na^{+} (2.8±1.5 mM), and anions such as Cl^{-} (200±12 mM) and SO_4^{2-} (30±5 mM). Sulfate has very similar chemical properties as selenate, and could lower the rate of selenate removal via competing adsorption on iron surfaces (Zhang, Wang et al. 2005). It should be noted that the sulfate concentration in scrubber water was much higher than selenium (molar ratio=1000-1500:1), and thus its interference had to be considered. The experimental result in Na_2SO_4 solution (Figure 5.6) further proved that sulfate indeed inhabited the removal of selenate (Mondal, Jegadeesan et al. 2004), and this effect was even enhanced at a higher concentration (Table 5.2). A similar trend was observed when studying the

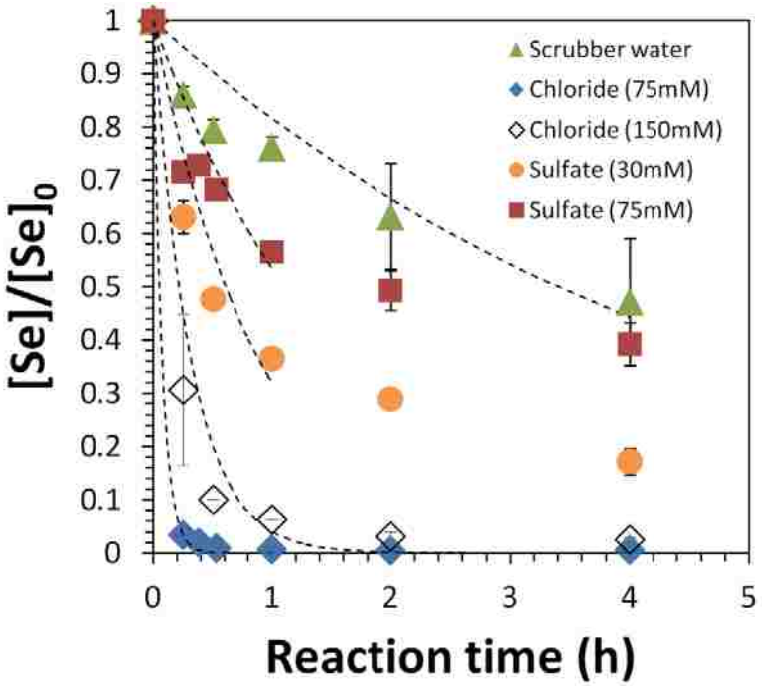

Figure 5.6. Selenium removal with iron nanoparticles suspension in batch mode. $[Fe]_0$=0.5±0.02 g/L; $[Se]_0$=1.3±0.1 mg/L in scrubber water, and 2±0.2 mg/L in synthetic NaCl and Na_2SO_4 solutions. pH of feed solution was adjusted to 4.5. Dash lines show the fit of pseudo-first-order law.

Table 5.2. Observed rate constant ($k_{obs,Se}$, h^{-1}) of selenium oxyanion removal with iron nanoparticles in different water matrix. $[Fe]_0$=0.5±0.02 g/L. Specific surface area: 37.8 m^2/g.

Water matrix	$k_{obs,Se}$ (h^{-1})
DIUF water	32.8
Scrubber Water	0.204
NaCl (75 mM/150 mM)	13.4/3.20
Na_2SO_4 (30 mM/75 mM)	1.14/0.626

effect of chloride with NaCl solution. Compared to sulfate, chloride had limited inhibition on the removal of selenate below 75 mM ($k_{obs,Se}$=13.4 h^{-1} at 75 mM). The rate constant decreased by 4 times ($k_{obs,Se}$=3.20 h^{-1}) after increasing its concentration to 150 mM. Similar results were reported by Mondal et al (Mondal, Jegadeesan et al. 2004), showing the selenate removal rate was greatly reduced by competing anions such as chloride at 10 g/L and sulfate at 2.5 g/L. In addition to adsorption, sulfate and chloride also enhanced the corrosion of iron, which formed an oxide layer and lifted the solution pH. Zeta potential measurement shows point of zero charge (PZC) of iron/iron oxide nanoparticles was between 7.5-7.8. At high pH (>8), the particle surface was negatively charged, and thus the adsorption of SeO_4^{2-} was weakened, resulting in a lower rate constant. After deoxygenated water washing, the reactivity of iron from selenate removal (100 mM Cl^-) was partially rejuvenated, with $k_{obs,Se}$=4.09 h^{-1} in NaCl solution and $k_{obs,Se}$=8.69 h^{-1} in DI water after washing (0.5±0.02 g/L iron). The increase of treatment time caused the rapid decline of reactivity in DI water ($k_{obs,Se}$=0.618 h^{-1} in the second cycle and $k_{obs,Se}$=0.473 h^{-1} in the third cycle). Those results provided the evidence that both anion adsorption and corrosion contributed to the slow removal of selenium oxyanions in scrubber water. Additionally, other ions existed in water such as NO_3^- (1.5±0.6 mM) and Ni^{2+} (6.7 μM) could also lower the reactivity of iron through reduction and/or adsorption (Su and Puls 2001; Lalvani 2004; Zhang, Wang et al. 2005).

5.4.2 Convective Flow Results with Functionalized Membranes

The high specific surface area of iron/iron oxide nanoparticles (20-300 m^2/g depending on the particle size) enhanced the removal of many toxic metals and organics through an adsorption-reduction-desorption process (Tee, Bachas et al. 2009), but the

particle aggregation due to ferromagnetic nature of iron, and the toxicity from iron leaching also need be evaluated before applying nanotechnology to real water treatment (Auffan, Rose et al. 2009; Lowry, Gregory et al. 2012; Schug, Johnson et al. 2013). PAA functionalized PVDF membrane provides a tunable platform for metal capture and nanoparticle in-situ synthesis, resulting in non-aggregated particles with uniform size (Xu and Bhattacharyya 2005). By applying the convective flow operation, the conversion of model compound is directly related to its residence time in membranes. Water is forced to flow through membranes under pressure, and thus the diffusion resistance from bulk solution to membrane pore area can be neglected. Additionally, there is no separation need when using membrane supported nanoparticles.

The residence time (τ) is defined as the ratio of membrane pore volume to water volume flow rate,

$$\tau = (A_m L \varepsilon_S (1-\Phi) - m_{Fe} / \rho_{Fe}) / Q \qquad \text{(E5.12)}$$

where m_{Fe} and ρ_{Fe} are the mass and density of iron nanoparticles in functionalized membranes. With a residence time of 10 s, 91.4% of selenate was removed in DI water at 25.2±1.9 L/(m^2·h·bar), while the conversion was 21.8% in scrubber water within 8.4 s at 15.3±0.4 L/(m^2·h·bar) (Figure 5.7). As discussed, the interference of salts and dissolved metal ions in scrubber water lowered the reactivity of iron. To recover the rate, either low TDS water (to reduce the competing adsorption) or more reactive iron (to compensate the reactivity loss with nitrate and dissolved metal ions) was required.

5.4.3 Integration of Nanofiltration (NF) and Functionalized Membranes

By applying NF membrane, divalent cations/anions were retained by charge exclusion, and counter ions associated with those ions were also retained due to charge

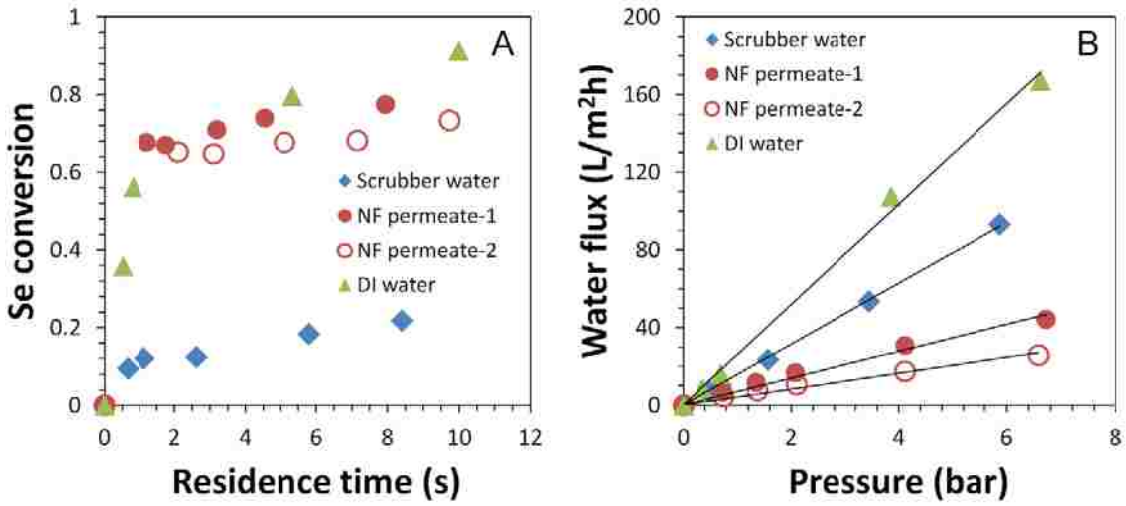

Figure 5.7. Selenium removal (A) and water flux (B) with iron functionalized membranes in different water matrix under convective flow condition. $[Se]_0$=1.3±0.1 mg/L in scrubber water, $[Fe]_0$=8.4 mg (20.7% weight gain), $[TDS]_0$=12 g/L ($[SO_4^{2-}]_0$=11.7 mM or 1120 mg/L); $[Se]_0$=52.3 µg/L in NF permeate-1 (positively charged NF membrane), $[Fe]_0$=9.9 mg (23% weight gain), $[TDS]_0$=2.4 g/L ($[SO_4^{2-}]_0$=292 µM or 28 mg/L); $[Se]_0$=11.0 µg/L in NF permeate-2 (negatively charged NF membrane), $[Fe]_0$=9.2 mg (23% weight gain), $[TDS]_0$=0.92 g/L ($[SO_4^{2-}]_0$=0.094 µM or 9 mg/L); $[Se]_0$=2±0.2 mg/L in DI water, $[Fe]_0$=4.0 mg (12.5% weight gain). pH of feed solution was adjusted to 4.5.

balance (within 5% difference). The total rejection of TDS was 94.0±1.5%. It should be noted that chloride rejection in NF membrane is completely different with Ca^{2+} or Na^{+} as counter ions. Divalent Ca^{2+} has higher electrical potential than Na^{+}, resulting in higher rejection of $CaCl_2$. The scrubber water mainly contains Ca^{2+} (90±10 mM) and Mg^{2+} (30±3 mM) as cations, with a small amount of Na^{+} (2.8±1.5 mM). Therefore, NF membrane is a better choice here to remove TDS, considering its higher water permeability and lower energy consumption than reverse osmosis membrane. Two types of nanofiltration membranes were used with different net charge, and the rejections of sulfate and chloride were 99.47±0.41% and 93.03±1.90%, respectively. The NF permeate had much less sulfate (0.07±0.05 mM) and chloride (13.1±3.6 mM), which didn't affect the removal of residual selenium oxyanions (0.16±0.07 μM). The conversion of selenium was 77.5% with a residence time of 8 s (Figure 5.7A). The major ion (i.e. chloride and sulfate) concentrations hardly changed when passing through functionalized membranes. With this combined technology, selenium concentration in final permeate was below 10 μg/L, which met U.S EPA's drinking water standard. This platform also benefited the removal of some other toxic metals such as arsenic, nickel and mercury. Arsenic concentration as low as 1 μg/L were achieved (Table 5.3). The reduction of Ni^{2+} by Fe^{0} forms Fe/Ni bimetallic nanoparticles, which can enhance the selenium removal via hydrogenation (Mondal, Jegadeesan et al. 2004). The same materials were also used for hydrodechlorination of chloro-organics (Tee, Bachas et al. 2009).

5.4.4 Effect of Temperature

Another possible solution to enhancing the reactivity of iron in scrubber water was to conduct the selenium removal at elevated temperatures. Mondal et al. reported that

Table 5.3. Selenium and other toxic metal removal from coal-fired power plant scrubber water via combined treatment with nanofiltraion and iron functionalized membranes.

	Se (µg/L)	As (µg/L)	Ni (µg/L)	Hg (µg/L)
Scrubber water-Feed	634	4.7	391	0.17
NF membrane treatment-Permeate	9-17	0.7-0.9	22.2-41.7	0.05-0.07
NF membrane followed by iron functionalized membrane treatment-Permeate	1.9-9.4	0.5	7.8-16.3	N/A

selenium removal increased by 22% when temperature rose from 25 °C to 65 °C (Mondal, Jegadeesan et al. 2004). The scrubber water from flue-gas desulfurization (FGD) process contains some waste heat with temperature around 40 °C. This could be a benefit for selenium removal. Our study shows the first-order rate constant of iron functionalized membranes increased by 3.8 times in DI water (Figure 5.8A), and 2.7 times in scrubber water at 40 °C (Figure 5.8B). The activation energy of iron in functionalized membranes was calculated to be 56.95 kJ/mol in DI water and 42.95 kJ/mol in scrubber water by Arrhenius equation and rate constants obtained (Table 5.4). The low activation energy in scrubber water can be due to the acceleration of iron corrosion by salts. The frequency factor in DI water (1.052×10^{10} h^{-1}) was three magnitudes higher than that in scrubber water (0.935×10^{7} h^{-1}). It again shows the competing adsorption of anions significantly inhabited the selenium removal.

5.4.5 Effect of Membrane Surface Charge

Iron functionalized membranes shows slightly higher reactivity in scrubber water but much lower reactivity in DI water than nanoparticles in suspension (Figure 5.8). Due to the incorporation of PAA, the functionalized membrane pores were negatively charged at pH 4.5 or above in DI water. Meanwhile, selenium oxyanions mainly existed as SeO_4^{2-} (pKa_2=1.9) and SeO_4^{2-}/$HSeO_3^-$ (pKa_1=2.9 and pKa_2=7.3) (Goldberg 2011). The repulsive electrostatic force between ionized carboxyl groups and selenium oxyanions might retard the selenium transport through membrane pores, especially inside the polymer domain where iron was immobilized, and thus delay the selenium removal. This assumption was proved by experimental results obtained in scrubber water, where membrane supported iron had better reactivity than iron suspension. Divalent cations (e.g. Ca^{2+}/Mg^{2+}) from

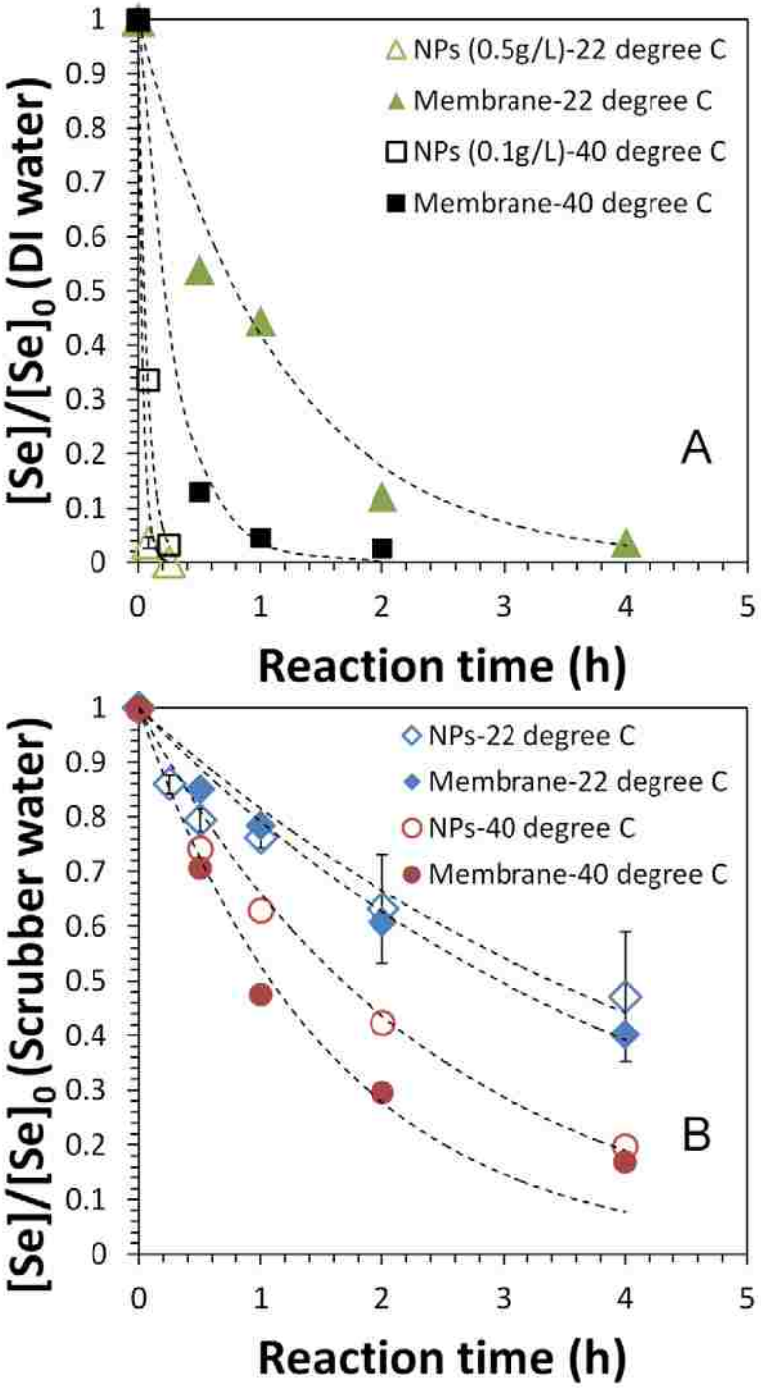

Figure 5.8. Temperature effect on selenium removal from DI water (A) and scrubber water (B) with iron nanoparticles suspension and iron functionalized membranes in batch mode. Dash lines show the fit of pseudo-first-order law. $[Fe]_0$=0.5±0.02 g/L (nanoparticles) and 0.47±0.04 g/L (membranes); $[Se]_0$=1.3±0.1 mg/L in scrubber water, and 2±0.2 mg/L in DI water. pH of feed solution was adjusted to 4.5. T=22 °C or 40 °C.

Table 5.4. Observed rate constant ($k_{obs,Se}$, h^{-1}) of selenium oxyanion removal with iron functionalized membranes at different temperatures. $[Fe]_0$=0.47±0.04 g/L.

T (°C)	DI water	Scrubber water
22	0.866	0.234
40	3.292	0.640

TDS immediately formed chelates with carboxyl groups, neutralizing the negative charge in membrane pores. The excessive cations adsorbed by PAA could also facilitate the diffusion of selenium oxyanions through the membrane. Additionally, the aggregation of nanoparticles (see TEM images in 5.4.7) could also increase the particle size and lower the specific surface area, resulting in lower reaction rate.

5.4.6 Iron Recapture by Functionalized Membranes

Iron oxidation in selenium removal and water corrosion can release ferrous ions into water, which are further oxidized to ferric ions in the presence of oxygen. Both ferrous and ferric ions precipitate as hydroxides at high pH. In DI water at 40 °C, iron loss with functionalized membranes (0.20±0.17%) was significantly lower than iron suspension result (5.4±0.6%) (Figure 5.9). The carboxyl groups of PAA formed chelates with Na^+ first, and then with Fe^{2+} during ion exchange. After $NaBH_4$ reduction, the carboxyl groups were back to Na^+ form, which could capture Fe^{2+} again. By taking advantage of this property, iron loading continued to grow with repeated ion exchange and reduction. However, with more iron immobilized in polymer network, the entry of Fe^{2+} into the carboxyl groups became more difficult, and IEC of membrane decreased by 43±5% after eight cycles. While in scrubber water, functionalized membranes lost the ion exchange ability since carboxyl groups of PAA also had strong binding affinity for Ca^{2+} and Mg^{2+}. With high TDS and an elevated temperature (40 °C), the dissolved iron percent also increased to 10.2±0.5% for iron functionalized membrane, and 8.7±1.9% for iron suspension.

5.4.7 Reduction and Adsorption Mechanism

The reduction of selenate by iron forms the elemental selenium (Se^0) and iron

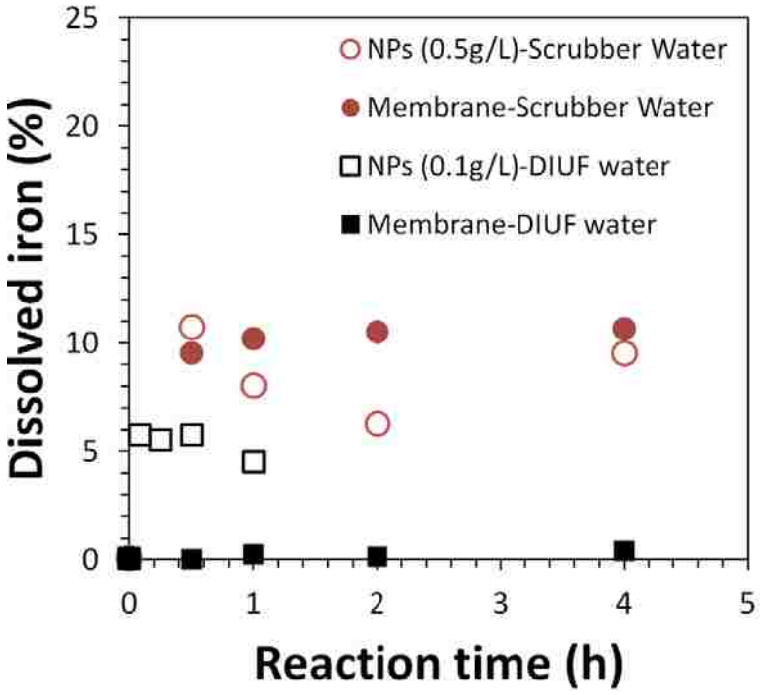

Figure 5.9. Dissolved iron percent in solutions during selenium removal with iron nanoparticle suspension and iron functionalized membranes in batch mode at 40 °C. $[Fe]_0$=0.47±0.04 g/L (membranes); $[Se]_0$=1.3±0.1 mg/L in scrubber water, and 2±0.2 mg/L in DI water. pH of feed solution was adjusted to 4.5.

selenide deposited on iron surface, as evidenced by X-ray absorption near edge structure (XANES) and extended x-ray absorption fine structure (EXAFS) spectroscopy (Scheinost and Charlet 2008). The release of ferrous ions due to electron transfer in selenium reduction resulted in the formation of an iron oxide layer above iron, which may contain ferrous/ferric hydroxides, lepidocrocite, maghemite and magnetite, depending on oxidation conditions (aerobic/anaerobic) and pH of solution (Murphy 1988; Olegario, Yee et al. 2010; Yoon, Kim et al. 2011). The Gibbs free energy change ($\Delta G<0$) and experimental results both shows that iron oxides containing Fe(II) such as green rust, ferrous hydroxide, mackinawite, siderite and magnetite could also achieve the transition from selenate/selenite to Se^0 (Murphy 1988; Myneni, Tokunaga et al. 1997; Zingaro, Dufner et al. 1997; Scheinost and Charlet 2008; Schellenger and Larese-Casanova 2013). Additionally, iron oxides such as ferrihydrite have been considered as good adsorbents for selenium removal, forming inner- and/or outer-sphere surface complexes (Peak and Sparks 2002; Das, Hendry et al. 2013). Therefore, selenium removal by iron nanoparticles involves both reduction and adsorption mechanism.

XPS spectra of iron after selenium removal shows both selenate (166.26 eV, 53.7 %) and Se^0 (161.07 eV, 46.3 %) existed on iron surface (Figure 5.10A). The oxidation of Se^0 deposited on iron surface was much slower compared to that of iron (Qiu, Lai et al. 2000). Therefore, selenate was mainly from iron oxide adsorption. Three main feature peaks including $2p_{3/2}$ (710.6 eV), satellite $2p_{3/2}$ (719.3 eV), and $2p_{1/2}$ (724.0 eV) are shown in Fe 2p spectra (Figure 5.10B), suggesting even the freshly made iron had an iron oxide layer (Sun, Li et al. 2006; Gui, Ormsbee et al. 2013). Iron nanoparticles were only partially oxidized after selenium removal as evidenced by Fe^0 peak at 706.6 eV.

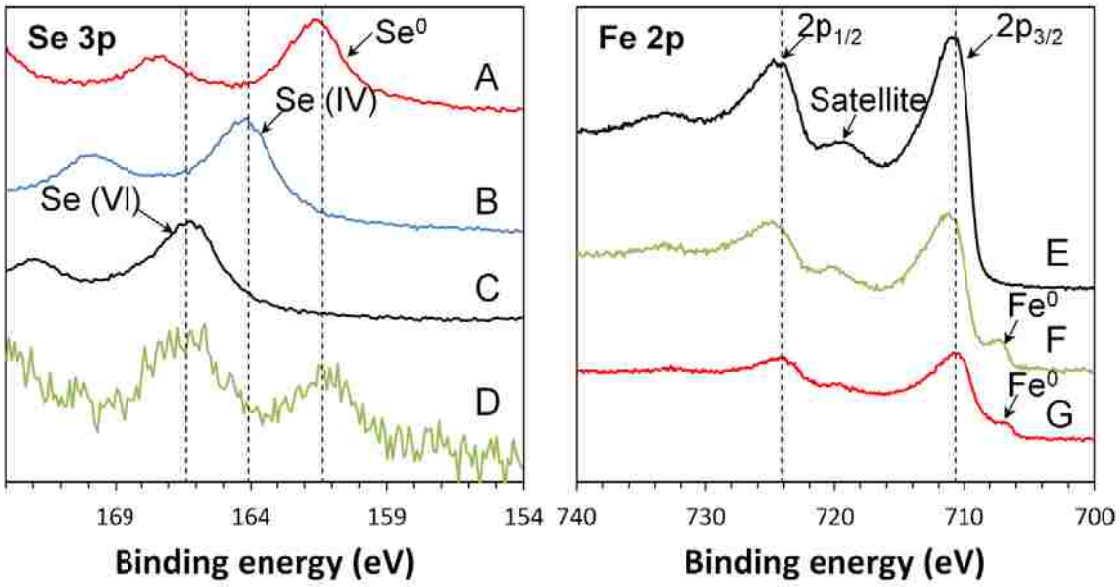

Figure 5.10. XPS spectra of iron nanoparticles after selenate removal. The left graph shows Se 3p spectra of (A) elemental selenium (Se^0), (B) sodium selenite, (C) sodium selenate, and (D) iron nanoparticles (0.5 g/L) after mixing with sodium selenate ($[Se]_0$=50 mg/L) for 1 h in DI water. The right graph shows Fe 2p spectra of (E) commercial iron oxide (γ-Fe_2O_3), (F) same as (D), and (G) freshly made iron (Fe^0). Se 3p spectra are used here due to an overlap between Se 3d and Fe 3p.

TEM image shows the morphology of iron/iron oxide nanoparticles after reduction of selenate (Figure 5.11). SAED patterns were similar to that of magnetite, suggesting that iron oxide layer contained mostly magnetite. Similar results were reported by Olegario et al. from XRD studies of nano Fe^0 oxidation during reaction with selenate (Olegario, Yee et al. 2010). High resolution image provides more details about the core-shell structure of partially oxidized iron, which contains an iron core (diameter: 15±2 nm) and iron oxide shell (thickness: 10±2 nm). The oxide layer was made of polycrystalline magnetite with size around 5 nm. Those iron oxides had high specific surface area, and were great materials for selenium adsorption. EDS line scan of particles in STEM mode also shows that outside particles had higher O/Fe ratio than those in core, and they were stacked on top of each other, forming a highly porous oxide layer. The intensity of Se peak was associated with that of iron peak, since the main source of selenium on iron surface was Se^0 from iron reduction. Even though iron was oxidized, the ratio of Fe/Se should have no significant change if there was no selenium dislodging from iron oxide surfaces.

To eliminate the effect of dissolved oxygen on reduction, selenium removal was conducted in a mixture of ethanol and deoxygenated water (9:1, v/v) with freshly made iron nanoparticles (Figure 5.12A) at high selenate concentration. After treatment, some needle-like materials with an amorphous structure was formed on iron surfaces (Figure 5.12B). Some particles were even embedded in a cotton-like structure (Figure 5.12C), which could be a mixture of iron corrosion products such as lepidocrocite and ferrous/ferric hydroxides (Olegario, Yee et al. 2010; Yoon, Kim et al. 2011). EDS elemental analysis on those reacted particles shows the selenium content was 0.8 at% in

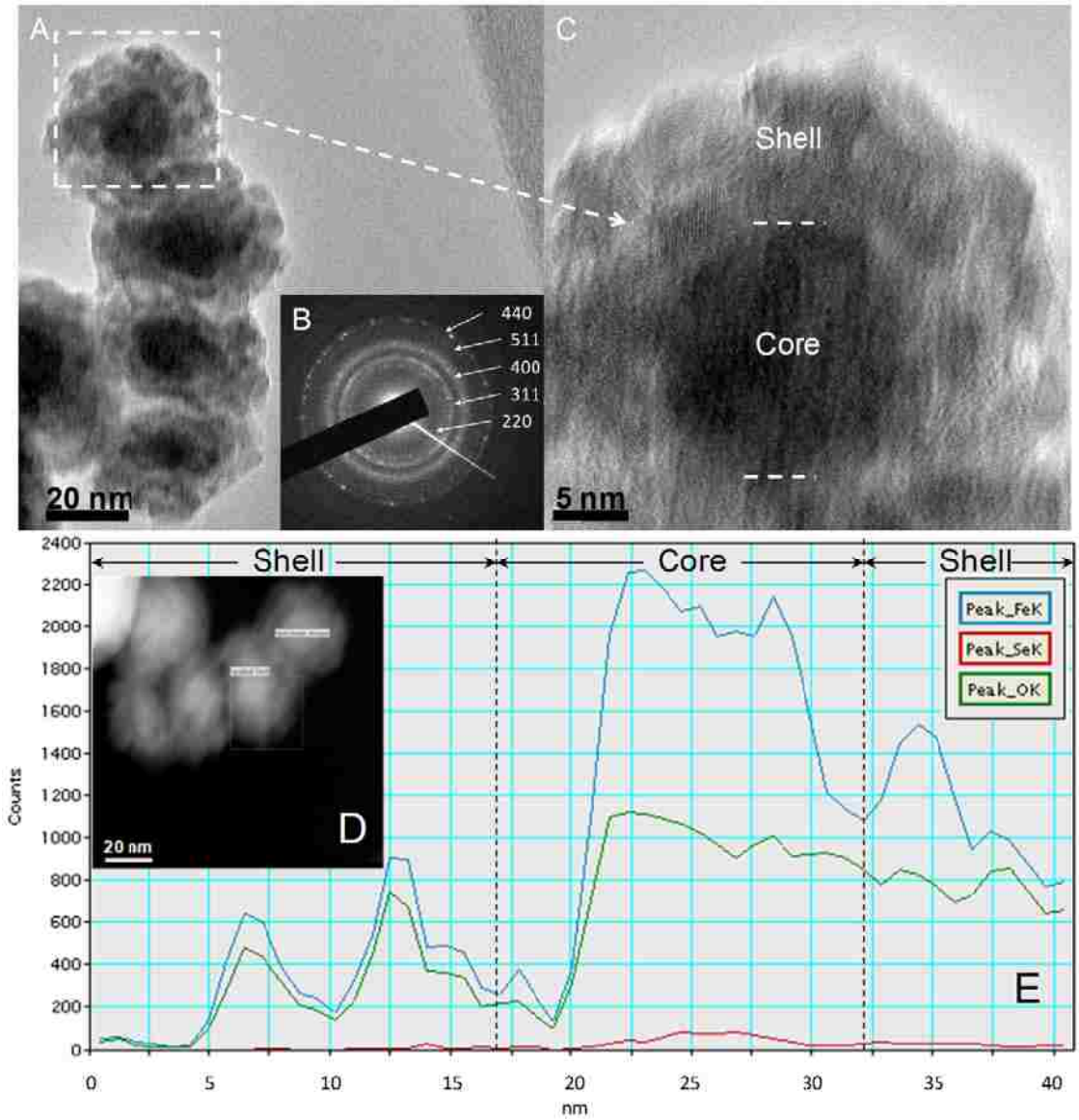

Figure 5.11. TEM images of iron nanoparticles after selenate removal in DI water (five cycle reaction). (A) Bright field image; (B) Selected area electron diffraction (SAED); (C) High-resolution TEM of iron/iron oxide core-shell structure; (D) Dark field image in STEM mode; (E) STEM-EDS line scan spectrum (step size: 1.5 nm, pixel time: 30 s). For each cycle, the reaction time was 10 min. $[Fe]_0$=0.5±0.02 g/L, $[Se]_0$=2±0.2 mg/L (made by Na_2SeO_4), and pH was adjusted to 4.5. The dash lines separate the core and shell of particles. Blue/red/green lines indicate Fe/Se/O, respectively.

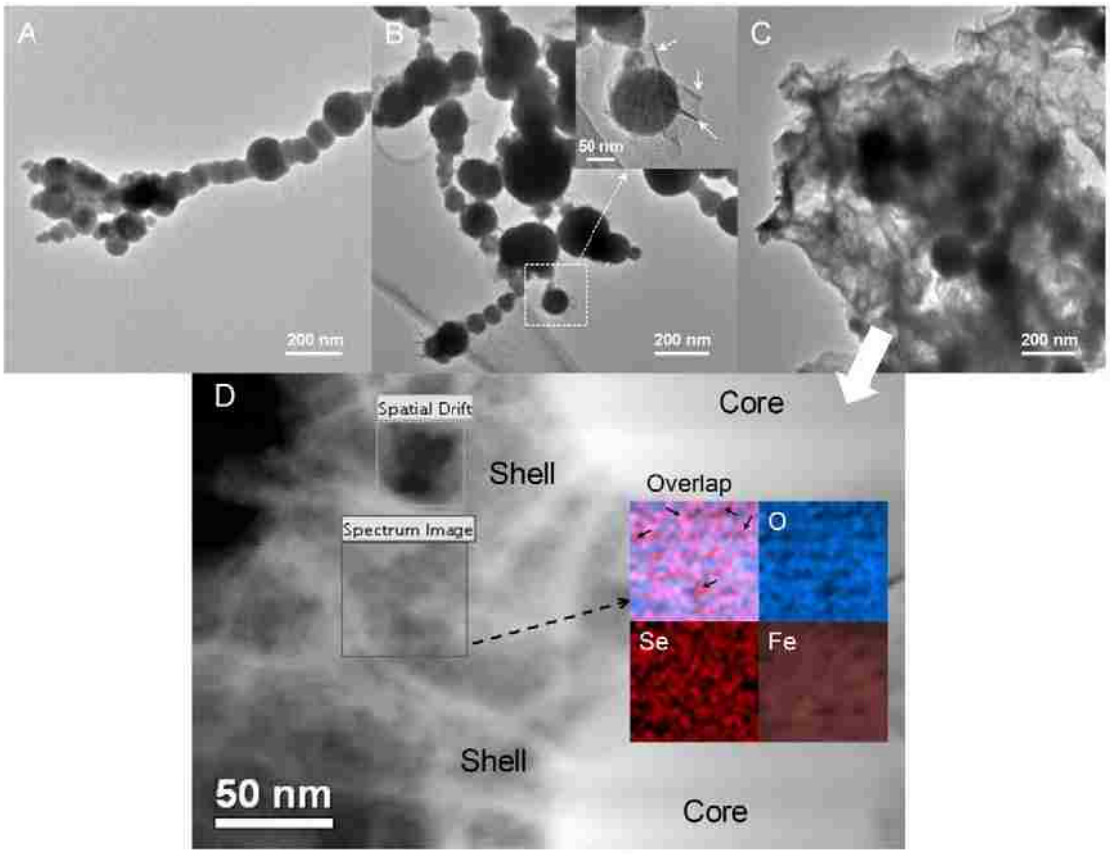

Figure 5.12. Iron oxide formation on iron surfaces during the selenium removal (anaerobic). (A) Freshly made iron; (B) (C) iron/iron oxide after reaction; (D) STEM-EELS mapping of iron oxide. Red/blue/brown colors indicate Se/O/Fe, respectively. Sample preparation: fresh iron nanoparticles ($[Fe]_0$=0.5±0.02 g/L) were mixed with Na_2SeO_4 solution for 24 h ($[Se]_0$=100 mg/L, [Ethanol]:[Deoxygenated water]=9:1, v/v). After that, iron was washed with deoxygenated water and pure ethanol, and sonicated for 30 s. TEM grid (lacey carbon film on 300 mesh copper grids) was soaked in diluted solution for seconds and dried in N_2 atmosphere before mounted in TEM sample holder.

Figure 5.12B and 8.6 at% in Figure 5.12C, with most selenium existing in iron oxide layer. The existence of iron selenide during reduction confirmed the deposition of Se^0 on iron surfaces (Myneni, Tokunaga et al. 1997; Scheinost and Charlet 2008; Olegario, Yee et al. 2010; Klas and Kirk 2013). Therefore, the diffusion of selenate through porous iron oxides and the electron transfer on iron surface could take place simultaneously. Ferrous ions are produced via reactions in E5.9-5.11 as well as the hydrogen generation with water (Sun, Li et al. 2006). Iron oxide precipitates containing Fe(II) can reduce selenate/selenite to Se^0, which stays in oxide layer (Myneni, Tokunaga et al. 1997). The dark field image clearly shows how iron oxide grew from iron surfaces. EELS mapping of a selected area in iron oxide layer gave the distribution of selenium, oxygen, and iron (Figure 5.12D). In some area, Se existed with Fe only (marked with arrows). This was consistent with XPS results, proving the simultaneous removal of selenium by reduction and adsorption.

5.5 Iron Nanoparticle Synthesis and Selenium Removal in Spiral Wound Module

The water flux of spiral wound functionalized membrane module (5 ft^2) varied between pH 4 and 9 with a transition pH at around 6 (Figure 5.13A), suggesting the successful pore functionalization. With repeated ion exchange and $NaBH_4$ reduction, 680±9 mg Fe was immobilized in this module. Synthetic solution with both selenate and selenite (same fraction as in scrubber water) was passed through iron functionalized membrane module convectively. With water flux of 110.4 L/(m^2·h) and a residence time of 1.2 s, the conversion of selenium was 0.47 in the permeate after running it for 1 min. It decreased rapidly from 1 min to 5 min, and maintained around 0.12 after 15 min (Figure 5.13B). The total volume of permeate was 17 L, and 27.6% of selenium was removed

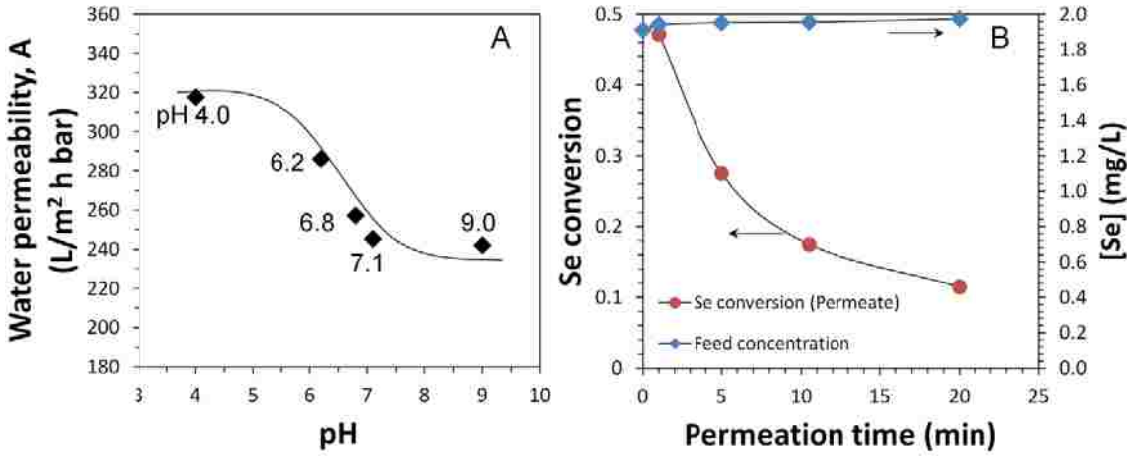

Figure 5.13. Full-scale PVDF400HE-PAA membrane module water flux and reactivity in selenium oxyanion removal. (A) Water permeability with pH at 25 °C; (B) Selenium removal results by passing synthetic selenium solution through iron immobilized module convectively. $[Fe]_0$=0.68 g, $[Se(VI)]_0$=1±0.05 mg/L, $[Se(IV)]_0$=1±0.05 mg/L (2±0.1 mg/L in total) in synthetic feed solution (pH=6.2), V=18 L, J_w=110.4 L/(m^2·h) and τ=1.2 s. The retentate flow rate was 22.5 L/h, and the total volume of permeate was 17 L. Effective membrane area: 5 ft^2. In pH responsive study, water flux was measured after being stabilized for 15 min. Water flux was already normalized with temperature due to viscosity change.

from synthetic solution, giving a minimum reduction capacity of 14.6±1.1 mg Se/g Fe. Feed concentration was measured during test, and the difference was within 3.3%. It should be noted that iron loading in the module (0.15 mg/cm^2) was half of that in lab-scale DI water study (0.30 mg/cm^2), resulting in a lower conversion. Iron corrosion was also faster in the module test since the selenium solution was exposed to air during circulation. Instead of using the functionalized membrane, a second NF membrane module can also further reduce the selenium concentration. However, the cost will be higher since the operating pressure of NF membrane is higher than that of functionalized membrane.

5.6 Membrane Regeneration

The maximum reduction capacity obtained in membrane convective experiments was 32.1±2.0 mg Se/g Fe, and significant amount of iron was not utilized during the selenium removal. As the thickness of iron oxide shell increases, neither electrons nor selenium oxyanions may transfer through this layer without iron surface regeneration. By acid treatment to dissolve the iron oxide, the membrane reactivity should be at least partially restored. For long-term treatment, the used membrane modules can be replaced by new modules considering the toxicity of selenium deposited on iron/iron oxide surface. Selenium can also be recycled via post treatment such as digestion and purification for further use in electronics industry.

Chapter Six Conclusions

In the last three chapters, the performance of iron and iron oxide functionalized membranes was evaluated in reductive and oxidative treatment of selected chloro-organics and toxic metals experimentally and mathematically. With the successful development of full-scale modules, this functionalized membrane technique potentially can be used for groundwater and scrubber water treatment.

6.1 Fundamental Advancements to Science and Engineering

The fundamental advancements to science and engineering achieved in this research are as follows.

- A solid proof of the concept that the integration of nanotechnology and membrane separation can extend the functionalized membrane applications through the creation of a reactive and tunable iron functionalized platform.
- The understanding of membrane transport in the development of both lab-scale and full-scale functionalized membranes for water remediation
- The use of heterogeneous Fenton reaction at near neutral pH for chlorinated organic degradation in groundwater can be achieved with reduced consumption of reactants by using engineered catalysts
- The advanced surface characterization techniques can be applied to functionalized membrane and nanocatalyst (metal/metal oxide) synthesis and reaction for better understanding the membrane formation and surface reaction mechanism
- The advantages of combining two chemical remediation methods for complete detoxification of selected chlorinated organics are demonstrated with less environmental and toxicity concern

6.2 Specific Achievements

The specific achievements made in membrane functionalization and water remediation are as follows.

- With improved in-situ polymerization technique, a highly pH responsive functionalized membrane platform is developed, with water permeability change up to 92±21 times from pH 3 to 8.
- Enhanced free radical oxidation efficiency was observed by using polysaccharide stabilized or functionalized membrane supported iron oxide nanoparticles. The aggregation of iron oxide catalysts can cause the increase of H_2O_2 consumption.
- Complete degradation of PCBs can be achieved via a combined reductive/oxidative pathway, using reactive membranes incorporated with iron related nanoparticles.
- The particle aggregation was eliminated through membrane synthesis, and membrane supported Fe/Pd show enhanced reactivity in PCB reductive dechlorination, compared to suspension.
- Laminar flow reactor model was developed for the prediction of PCB degradation through Fe/Pd functionalized membranes.
- Hydroxylated (Mono-, di- and trihydroxybiphenyls) and ring-open (benzoic acid) byproducts were detected as the main products in the subsequent oxidation of biphenyl by free radicals, proving the oxidation of PCBs started with the hydroxylation of aromatic ring followed by the ring cleavage.

- In convective flow mode, the diffusion resistance from bulk solution to membrane pore area was eliminated. 2-Chlorobipheyl and selenium can be completely removed by iron functionalized membranes in a short residence time.
- Selenium removal was significantly inhabited by competing adsorption of sulfate and chloride on iron surface. However, by lowering TDS concentration with NF membranes or applying elevated temperature, the salt interference was reduced or eliminated.
- Nanomaterial and membrane characterization methodologies were developed by using XPS as well as EDS/EELS line scan and elemental mapping in TEM. The formation of iron/iron oxide core-shell structure during iron controlled oxidation was confirmed. Iron oxides containing Fe(II) can enhance the oxidative dechlorination of biphenyl as well as the selenium removal through adsorption and reduction.
- For the first time, iron nanoparticles were in-situ synthesized in full-scale membrane module. Convective flow reaction results obtained from lab-scale and full-scale membranes demonstrated the potential of using this platform for groundwater and industrial wastewater treatment.

Nomenclature

Chapter Three

C_{H2O2} is the concentration of H_2O_2 in bulk solution (mmol/L)

k_{obs} is the observed first-order reaction rate of H_2O_2 decomposition (/h)

a_s is the specific surface area of particles (m^2/g)

ρ_m is the loading in the system (g/L)

k_{SA} is the surface-area-normalized rate for H_2O_2 decomposition ($L/(m^2 \cdot h)$)

E is the efficiency of H_2O_2 consumption in TCE oxidation

C_{TCE} is the TCE concentration in water (mmol/L)

$C_{OH\bullet}$ is the concentration of OH• near the reactive sites (mmol/L)

k'' is the second-order reaction rate of TCE oxidation (L/(mmol·h))

$k_{obs(TCE)}$ is the observed pseudo-first-order reaction rate of TCE oxidation (/h)

≡S is the reactive site on iron oxide surfaces

I is the intermediate formed during TCE oxidation

P is the final product

k_{TCE} is the oxidation rate of adsorbed TCE with OH• (L/(mmol·h))

k_{in} is the oxidation rate of adsorbed reaction intermediate I with OH• (L/(mmol·h))

$k_{TCE,a}$ is the adsorption rate of TCE on iron oxide surfaces (L/(mmol·h))

$k_{TCE,d}$ is the desorption rate of TCE on iron oxide surfaces (/h)

$k_{in,a}$ is the adsorption rate of reaction intermediate I on iron oxide surfaces (L/(mmol·h))

$k_{in,d}$ are the desorption rate of reaction intermediate I on iron oxide surfaces (/h)

$C_{TCE\equiv S}$ is the concentration of adsorbed TCE on iron oxide surfaces (mmol/L)

C_{S0} is the concentration of total reactive sites (mmol/L)

C_S is the concentration of unoccupied reactive sites (mmol/L)

θ is the fraction of occupied reactive sites ($\theta=C_{TCE\equiv S}/C_{S0}$)

k_1 represents the reactivity of OH• with TCE (mol/(L·h)) ($k_1=k_{TCE}C_{OH\bullet}C_{S0}$)

k_2 reflects the adsorption and desorption equilibrium of TCE on iron oxide surfaces (mol/L) ($k_2=(k_{TCE,d}+k_{TCE}C_{OH\bullet})/k_{TCE,a}$)

Chapter Four

η is the water viscosity (mPa·s)

L is the membrane thickness (m)

Q is the volume flow rate (L/h)

J_w is the water flux at a specific pressure (L/(m^2·h))

A_m is the external area of membrane (m^2)

ΔP is the transmembrane pressure (bar)

D_0 is the equivalent diameter for PVDF membrane support (nm)

A_0 is the water permeability for PVDF membrane support (L/(m^2·h·bar))

D is the equivalent diameter for the pore functionalized membrane (nm)

A is the water permeability for the pore functionalized membrane (L/(m^2·h·bar))

τ is the residence time of 2-chlorobiphenyl in the membrane (h)

V_m is the membrane pore volume (m^3)

ε_s is the membrane porosity

V_{GEL} is the polymer volume in the dried state (m^3)

V_{NP} is the volume occupied by Fe/Pd nanoparticles (m^3)

r is the reaction rate (mmol/(L·h))

$C_{0,PCB}$ is the concentrations of 2-chlorobiphenyl in the feed (mmol/L)

C_{PCB} is the concentrations of 2-chlorobiphenyl at time t (mmol/L)

$k_{obs,PCB}$ is the observed rate constant (/h)

$k_{SA,PCB}$ is the surface-area-normalized rate constant (L/(m^2·h))

α_s is the specific surface area of Fe/Pd particles (m^2/g)

ρ_m is the loading of particles (g/L)

X is the conversion of 2-chlorobiphenyl

u_r is the velocities at radius r (m/s)

u_0 is the velocities at pore center (m/s)

u_{ave} is the average velocity in the pore (m/s)

R is the equivalent pore radius (m)

Q_r is the volume flow rate through an annular element of radius r (L/h)

X_{ave} is the average conversion of 2-chlorobiphenyl

τ_0 is the residence time of 2-chlorobiphenyl at the pore center (h)

τ_∞ is the residence time of 2-chlorobiphenyl at wall (h)

C_{2OHBP} is the concentration of 2-hydroxybiphenyl in the solution (mmol/L)

$C_{OH\bullet}$ is the concentration of OH• (mmol/L)

k''_{2OHBP} is the second-order rate constant (L/(mmol·h))

k'_{2OHBP} is the first-order rate constant (/h) ($k'_{2OHBP} = k''_{2OHBP} C_{OH\bullet}$)

Chapter Five

W_0 is the weight of membrane before functionalization (g)

W' is the weight of membrane after functionalization (g)

k_{gel} is the Darcy permeability of gel (m^2)

k_m is the membrane permeability (m^2)

ε_s is the porosity of substrate PVDF membrane

τ_s is the tortuosity of membrane

J_w is the water flux through the functionalized membrane (L/(m^2h))

Q is the water volume flow rate (L/h)

A_m is the membrane area (m^2)

L is the thickness of membrane (m)

η is the water viscosity (mPa·s)

ΔP is the transmembrane pressure (bar)

K_S is the Kozeny constant (=5) for a substrate membrane with porosity around 2/3

K^* is the Kozeny constant (=2) for parallel capillary-type pores of circular cross-section

Φ is the gel volume fraction of functionalized membrane

V_{gel} is the gel volume (m^3)

V_m is the membrane pore volume (m^3)

ρ_{gel} is the density of PAA hydrogel in membrane pores (g/m^3)

[Se] is the selenium concentration (mmol/L)

$k_{obs,Se}$ is the observed first-order reaction rate (/h)

τ is the residence time of selenium in the membrane (h)

m_{Fe} is the mass of iron nanoparticles in functionalized membranes (g)

ρ_{Fe} is the density of iron nanoparticles in functionalized membranes (g/cm^3)

Chemical Abbreviations

AA: Acrylic acid

BSTFA: N,O-Bis(trimethylsilyl) trifluoroacetamide

BTEX: Benzene, toluene, ethylbenzene, and xylenes

NNMA: N,N’-methylenebisacrylamide

PAA: Polyacrylic acid

PCBs: Polychlorinated biphenyls

PES: Polyether sulfone

PSf: Polysulfone

PVDF: Polyvinylidene fluoride

PVP: Polyvinylpyrrolidone

TCE: Trichloroethylene

MATLAB Programs

Chapter Three: Adsorption and desorption model

(1) TCE oxidation in aqueous phase with CMC-stabilized iron oxide nanoparticles:

```
% [Iron oxide]=1.33 g/L
function Aqueous(data,zdata,k)
xdata = [0.270388155 0.250289146 0.2150186 0.085671083 0.004534603 3.81E-05]; %
TCE concentration (mM)
ydata = [0 3 8 17 24 48]; % Reaction time (h)
zdata = [0 0 0 0 0 0];
data = [xdata;ydata];
k0 = [1e-10 1e-10];
[k,Resnorm]=lsqcurvefit(@myfun, k0, data, zdata)
for t=0:48;
   c=fsolve(@(c) k(1)*t+k(2)*log(c./0.27)-(0.27-c),1e-12);
   fprintf('%s\t',c);
   plot(t,c,'ko-');
   hold on;
end
xlabel('Reaction time (h)');
ylabel('TCE concentration (mM)');
title('TCE oxidation with CMC-stabilized iron oxide nanoparticles (1.33 g/L)')
%-------------------------------------------------
function F = myfun(k,data)
x = data(1,:);
y = data(2,:);
F = k(1).*y+k(2)*log(x./0.27)-(0.27-x);

% [Iron oxide]=0.67 g/L
function Aqueous2(data,zdata,k)
xdata = [0.27 0.252166089 0.231821421 0.13399678 0.068301921 0.000846259]; %
TCE concentration (mM)
ydata = [0 3 7 17.5 25 49]; % Reaction time (h)
zdata = [0 0 0 0 0 0];
data = [xdata;ydata];
k0 = [1e-10 1e-10];
[k,Resnorm]=lsqcurvefit(@myfun, k0, data, zdata)
for t=0:48;
   c=fsolve(@(c) k(1)*t+k(2)*log(c./0.27)-(0.27-c),1e-12);
   fprintf('%s\t',c);
   plot(t,c,'ko-');
   hold on;
end
xlabel('Reaction time (h)');
```

```
ylabel('TCE concentration (mM)');
title('TCE oxidation with CMC-stabilized iron oxide nanoparticles (0.67 g/L)')
%-----------------------------------------------
function F = myfun(k,data)
x = data(1,:);
y = data(2,:);
F = k(1).*y+k(2)*log(x./0.27)-(0.27-x);
```

(2) TCE oxidation with membrane supported iron oxide nanoparticles:

```
function MEM(data,zdata,k)
xdata = [0.27 0.223721959 0.16103824 0.08627023 0.06819707]; % TCE concentration
(mM)
ydata = [0 12 24 33 48]; % Reaction time (h)
zdata=[0.02 0.05 0.05 0.02 0.02];% TCE adsorbed in membranes
data=[xdata;ydata];
k0=[1e-10 1e-10];
[k,Resnorm]=lsqcurvefit(@myfun, k0, data, zdata)
for t=0:48;
    c=fsolve(@(c) k(1)*t+k(2)*log(c./0.27)-(0.27-c),1e-12);
    fprintf('%s\t',c);
    plot(t,c,'ko-');
    hold on;
end
xlabel('Reaction time (h)');
ylabel('TCE concentration (mM)');
title('TCE oxidation with membrane supported iron oxide nanoparticles ([Fe]=0.88 g/L as
iron oxide)')
%-----------------------------------------------
function F = myfun(k,data)
x=data(1,:);
y=data(2,:);
F = k(1).*y+k(2)*log(x./0.27)-(0.27-x);
```

References

Ahmad, M., A. L. Teel, et al. (2012). "Oxidative and Reductive Pathways in Iron-Ethylenediaminetetraacetic Acid-Activated Persulfate Systems." Journal of Environmental Engineering-Asce **138**(4): 411-418.

Ahmad, M., M. A. Simon, et al. (2011). "Treatment of polychlorinated biphenyls in two surface soils using catalyzed H2O2 propagations." Chemosphere **84**(7): 855-862.

Ahn, J. Y., W. J. Chung, et al. (2008). "Poly sulfone/silica nanoparticle mixed-matrix membranes for gas separation." Journal of Membrane Science **314**(1-2): 123-133.

Ahuja, D. K., L. G. Bachas, et al. (2007). "Modified Fenton reaction for trichlorophenol dechlorination by enzymatically generated H2O2 and gluconic acid chelate." Chemosphere **66**(11): 2193-2200.

Ai, Z. H., L. R. Lu, et al. (2007). "Fe@Fe2O3 core-shell nanowires as iron reagent. 1. Efficient degradation of Rhodamine B by a novel sono-Fenton process." Journal of Physical Chemistry C **111**(11): 4087-4093.

Amarante, D. (2000). "Applying in situ chemical oxidation." Pollution Engineering **32**(2): 40-42.

Apel, P. (2001). "Track etching technique in membrane technology." Radiation Measurements **34**(1-6): 559-566.

Auffan, M., J. Rose, et al. (2009). "Towards a definition of inorganic nanoparticles from an environmental, health and safety perspective." Nature Nanotechnology **4**(10): 634-641.

Baker, R. W. (2004). Membrane Technology and Applications, Wiley.

Baker, R. W., J. G. Wijmans, et al. (2010). "Permeability, permeance and selectivity: A preferred way of reporting pervaporation performance data." Journal of Membrane Science **348**(1-2): 346-352.

Belfer, S., Y. Purinson, et al. (1998). "Surface modification of commercial composite polyamide reverse osmosis membranes." Journal of Membrane Science **139**(2): 175-181.

Belfer, S., Y. Purinson, et al. (1998). "Surface modification of commercial polyamide reverse osmosis membranes by radical grafting: An ATR-FTIR study." Acta Polymerica **49**(10-11): 574-582.

Bell, A. T. (2003). "The impact of nanoscience on heterogeneous catalysis." Science **299**(5613): 1688-1691.

Bergendahl, J. A. and T. P. Thies (2004). "Fenton's oxidation of MTBE with zero-valent iron." Water Research **38**(2): 327-334.

Bernardo, P., E. Drioli, et al. (2009). "Membrane Gas Separation: A Review/State of the Art." Industrial & Engineering Chemistry Research **48**(10): 4638-4663.

Betz, N., J. Begue, et al. (2003). "Functionalisation of PAA radiation grafted PVDF." Nuclear Instruments & Methods in Physics Research Section B-Beam Interactions with Materials and Atoms **208**: 434-441.

Beuermann, S. (2002). "Propagation kinetics in free-radical polymerizations." Macromolecular Symposia **182**: 31-42.

Bezbaruah, A. N., S. Krajangpan, et al. (2009). "Entrapment of iron nanoparticles in calcium alginate beads for groundwater remediation applications." Journal of Hazardous Materials **166**(2-3): 1339-1343.

Bhattacharyya, D., T. Schafer, et al. (2013). Responsive Membranes and Materials, John Wiley.

Bhut, B. V. and S. M. Husson (2009). "Dramatic performance improvement of weak anion-exchange membranes for chromatographic bioseparations." Journal of Membrane Science **337**(1-2): 215-223.

Bouroushian, M. (2010). Electrochemistry of the Chalcogens. Electrochemistry of Metal Chalcogenides. M. Bouroushian, Springer Berlin Heidelberg**:** 57-75.

Bowman, J. P., L. Jimenez, et al. (1993). "Characterization of the Methanotrophic Bacterial Community Present in a Trichloroethylene-Contaminated Subsurface Groundwater Site." Applied and Environmental Microbiology **59**(8): 2380-2387.

Brandrup, J., Immergut, E. H., E. A. Grulke, E. A. (2003). Polymer Handbook, Wiley-Interscience**:** VII-198.

Bruening, M. L., D. M. Dotzauer, et al. (2008). "Creation of functional membranes using polyelectrolyte multilayers and polymer brushes." Langmuir **24**(15): 7663-7673.

Chapiro, A. and Z. Mankowski (1981). "Influence of Solvents on Molecular Association and Kinetics of Acrylonitrile Polymerization - Supplementary Details on the Matrix Effect." European Polymer Journal **17**(5): 457-472.

Charcosset, C. (2012). Membrane chromatography. Membrane Processes in Biotechnologies and Pharmaceutics. C. Charcosset, Elsevier**:** 169-212.

Chen, N. H. (1983). Process Reactor Design, Allyn and Bacon.

Chen, X. F. and R. H. Schuler (1993). "Directing Effects of Phenyl Substitution in the Reaction of Oh Radical with Aromatics - the Radiolytic Hydroxylation of Biphenyl." Journal of Physical Chemistry **97**(2): 421-425.

Chen, X., Y. He, et al. (2014). "Temperature- and pH-responsive membranes based on poly (vinylidene fluoride) functionalized with microgels." Journal of Membrane Science **469**: 447-457.

Chen, Z., J. Zhang, et al. (2014). "Functionalized Anodic Aluminum Oxide Membrane-Electrode System for Enzyme Immobilization." Acs Nano **ASAP**.

Cheng, C., A. Yaroshchuk, et al. (2013). "Fundamentals of Selective Ion Transport through Multilayer Polyelectrolyte Membranes." Langmuir **29**(6): 1885-1892.

Chung, T. S., L. Y. Jiang, et al. (2007). "Mixed matrix membranes (MMMs) comprising organic polymers with dispersed inorganic fillers for gas separation." Progress in Polymer Science **32**(4): 483-507.

Clapp, P. A., D. F. Evans, et al. (1989). "Spectrophotometric Determination of Hydrogen-Peroxide after Extraction with Ethyl-Acetate." Analytica Chimica Acta **218**(2): 331-334.

Clochard, M. C., J. Begue, et al. (2004). "Tailoring bulk and surface grafting of poly(acrylic acid) in electron-irradiated PVDF." Polymer **45**(26): 8683-8694.

Costa, R. C. C., F. C. C. Moura, et al. (2008). "Highly active heterogeneous Fenton-like systems based on Fe-0/Fe3O4 composites prepared by controlled reduction of iron oxides." Applied Catalysis B-Environmental **83**(1-2): 131-139.

Cullity, B. D. and S. R. Stock (2001). Elements of X-Ray Diffraction, Prentice Hall.

Dai, J. H. and M. L. Bruening (2002). "Catalytic nanoparticles formed by reduction of metal ions in multilayered polyelectrolyte films." Nano Letters **2**(5): 497-501.

Dalla Vecchia, E., M. Luna, et al. (2009). "Transport in Porous Media of Highly Concentrated Iron Micro- and Nanoparticles in the Presence of Xanthan Gum." Environmental Science & Technology **43**(23): 8942-8947.

Das, S., M. J. Hendry, et al. (2013). "Adsorption of selenate onto ferrihydrite, goethite, and lepidocrocite under neutral pH conditions." Applied Geochemistry **28**: 185-193.

Datta, S., C. Cecil, et al. (2008). "Functionalized membranes by layer-by-layer assembly of polyelectrolytes and in situ polymerization of acrylic acid for applications in enzymatic catalysis." Industrial & Engineering Chemistry Research **47**(14): 4586-4597.

Dhananjeyan, M. R., E. Mielczarski, et al. (2001). "Photodynamics and surface characterization of TiO2 and Fe2O3 photocatalysts immobilized on modified polyethylene films." Journal of Physical Chemistry B **105**(48): 12046-12055.

Dotzauer, D. M., J. H. Dai, et al. (2006). "Catalytic membranes prepared using layer-by-layer adsorption of polyelectrolyte/metal nanoparticle films in porous supports." Nano Letters **6**(10): 2268-2272.

Elimelech, M. and W. A. Phillip (2011). "The Future of Seawater Desalination: Energy, Technology, and the Environment." Science **333**(6043): 712-717.

Fan, D. M., R. P. Anitori, et al. (2013). "Reductive Sequestration of Pertechnetate ((TcO4-)-Tc-99) by Nano Zerovalent Iron (nZVI) Transformed by Abiotic Sulfide." Environmental Science & Technology **47**(10): 5302-5310.

Fang, Y. X. and S. R. Al-Abed (2008). "Correlation of 2-chlorobiphenyl dechlorination by Fe/Pd with iron corrosion at different pH." Environmental Science & Technology **42**(18): 6942-6948.

Fang, Y. X. and S. R. Al-Abed (2008). "Dechlorination kinetics of monochlorobiphenyls by Fe/Pd: Effects of solvent, temperature, and PCB concentration." Applied Catalysis B-Environmental **78**(3-4): 371-380.

Fenton, H. J. H. (1894). "Oxidation of Tartaric Acid in Presence of Iron." Journal of the Chemical Society, Transactions **65**: 899-910.

Fogler, S. H. (2005). Elements of Chemical Reaction Engineering, Prentice Hall.

Freger, V., J. Gilron, et al. (2002). "TFC polyamide membranes modified by grafting of hydrophilic polymers: an FT-IR/AFM/TEM study." Journal of Membrane Science **209**(1): 283-292.

Freyria, F. S., B. Bonelli, et al. (2011). "Reactions of Acid Orange 7 with Iron Nanoparticles in Aqueous Solutions." Journal of Physical Chemistry C **115**(49): 24143-24152.

Furukawa, Y., J. W. Kim, et al. (2002). "Formation of ferrihydrite and associated iron corrosion products in permeable reactive barriers of zero-valent iron." Environmental Science & Technology **36**(24): 5469-5475.

Gates, D. D. and R. L. Siegrist (1995). "In-Situ Chemical Oxidation of Trichloroethylene Using Hydrogen-Peroxide." Journal of Environmental Engineering-Asce **121**(9): 639-644.

Giraldi, T. R., C. C. Arruda, et al. (2009). "Heterogeneous Fenton reactants: a study of the behavior of iron oxide nanoparticles obtained by the polymeric precursor method." Journal of Sol-Gel Science and Technology **52**(2): 299-303.

Girones, M., R. G. H. Lammertink, et al. (2006). "Protein aggregate deposition and fouling reduction strategies with high-flux silicon nitride microsieves." Journal of Membrane Science **273**(1-2): 68-76.

Goldberg, S. (2011). Chemical Equilibrium and Reaction Modeling of Arsenic and Selenium in Soils. Dynamics and Bioavailability of Heavy Metals in the Rootzone. H. Magdi Selim, CRC Press**:** 65-92.

Golzar, M., S. F. Saghravani, et al. (2014). "Experimental Study and Numerical Solution of Poly Acrylic Acid Supported Magnetite Nanoparticles Transport in a One-Dimensional Porous Media." Advances in Materials Science and Engineering.

Gong, Y. Y., Y. Y. Liu, et al. (2014). "Immobilization of Mercury by Carboxymethyl Cellulose Stabilized Iron Sulfide Nanoparticles: Reaction Mechanisms and Effects of Stabilizer and Water Chemistry." Environmental Science & Technology **48**(7): 3986-3994.

Grasselli, M. and N. Betz (2005). "Electron-beam induced RAFT-graft polymerization of poly(acrylic acid) onto PVDF." Nuclear Instruments & Methods in Physics Research Section B-Beam Interactions with Materials and Atoms **236**: 201-207.

Gromov, V. F., N. I. Galperina, et al. (1980). "Effect of Solvent on Chain Propagation and Termination Reaction-Rates in Radical Polymerization." European Polymer Journal **16**(6): 529-535.

Guan, Y. and Y. J. Zhang (2011). "PNIPAM microgels for biomedical applications: from dispersed particles to 3D assemblies." Soft Matter **7**(14): 6375-6384.

Gui, M. H., V. Smuleac, et al. (2012). "Iron oxide nanoparticle synthesis in aqueous and membrane systems for oxidative degradation of trichloroethylene from water." Journal of Nanoparticle Research **14**(5).

Gui, M., L. E. Ormsbee, et al. (2013). "Reactive Functionalized Membranes for Polychlorinated Biphenyl Degradation." Industrial & Engineering Chemistry Research **52**(31): 10430-10440.

Guillen, G. R., Y. J. Pan, et al. (2011). "Preparation and Characterization of Membranes Formed by Nonsolvent Induced Phase Separation: A Review." Industrial & Engineering Chemistry Research **50**(7): 3798-3817.

Guo, L., Q. J. Huang, et al. (2006). "PVP-coated iron nanocrystals: Anhydrous synthesis, characterization, and electrocatalysis for two species." Langmuir **22**(18): 7867-7872.

Gupta, B. D. and A. Chapiro (1989). "Preparation of Ion-Exchange Membranes by Grafting Acrylic-Acid into Pre-Irradiated Polymer-Films .1. Grafting into Polyethylene." European Polymer Journal **25**(11): 1137-1143.

Gupta, B. D. and A. Chapiro (1989). "Preparation of Ion-Exchange Membranes by Grafting Acrylic-Acid into Pre-Irradiated Polymer-Films .2. Grafting into Teflon Fep." European Polymer Journal **25**(11): 1145-1148.

Hageman, S. P. W., R. D. van der Weijden, et al. (2013). "Microbiological selenate to selenite conversion for selenium removal." Water Research **47**(7): 2118-2128.

Halpaap, K., M. G. Horning, et al. (1978). "Metabolism of Biphenyl in the Rat." Journal of Chromatography **166**(2): 479-490.

Han, K. P., W. D. Xu, et al. (2005). "Fabrication and characterization of polymeric microfiltration membranes using aperture array lithography." Journal of Membrane Science **249**(1-2): 193-206.

Hartmann, M., S. Kullmann, et al. (2010). "Wastewater treatment with heterogeneous Fenton-type catalysts based on porous materials." Journal of Materials Chemistry **20**(41): 9002-9017.

Hashimoto, T., K. Tsutsumi, et al. (1997). "Nanoprocessing based on bicontinuous microdomains of block copolymers: Nanochannels coated with metals." Langmuir **13**(26): 6869-6872.

Hautojarvi, J., K. Kontturi, et al. (1996). "Characterization of graft-modified porous polymer membranes." Industrial & Engineering Chemistry Research **35**(2): 450-457.

Hazen, T. C. (2010). In Situ: Groundwater Bioremediation, Springer-Verlag Berlin Heidelberg.

He, F. and D. Y. Zhao (2008). "Hydrodechlorination of trichloroethene using stabilized Fe-Pd nanoparticles: Reaction mechanism and effects of stabilizers, catalysts and reaction conditions." Applied Catalysis B-Environmental **84**(3-4): 533-540.

He, F., D. Y. Zhao, et al. (2007). "Stabilization of Fe-Pd nanoparticles with sodium carboxymethyl cellulose for enhanced transport and dechlorination of trichloroethylene in soil and groundwater." Industrial & Engineering Chemistry Research **46**(1): 29-34.

He, F., D. Y. Zhao, et al. (2010). "Field assessment of carboxymethyl cellulose stabilized iron nanoparticles for in situ destruction of chlorinated solvents in source zones." Water Research **44**(7): 2360-2370.

Hernandez, S., J. K. Papp, et al. (2014). "Iron-Based Redox Polymerization of Acrylic Acid for Direct Synthesis of Hydrogel/Membranes and Metal Nanoparticles for Water Treatment." Industrial & Engineering Chemistry Research **53**(3): 1130-1142.

Ho, W. and K. Sirkar (1992). Membrane Handbook, Springer.

Hoag, G. E., J. B. Collins, et al. (2009). "Degradation of bromothymol blue by 'greener' nano-scale zero-valent iron synthesized using tea polyphenols." Journal of Materials Chemistry **19**(45): 8671-8677.

Hollman, A. M. and D. Bhattacharyya (2004). "Pore assembled multilayers of charged polypeptides in microporous membranes for ion separation." Langmuir **20**(13): 5418-5424.

Hu, K. and J. M. Dickson (2007). "Development and characterization of poly(vinylidene fluoride)-poly (acrylic acid) pore-filled pH-sensitive membranes." Journal of Membrane Science **301**(1-2): 19-28.

Huang, H. H., M. C. Lu, et al. (2001). "Catalytic decomposition of hydrogen peroxide and 2-chlorophenol with iron oxides." Water Research **35**(9): 2291-2299.

Huang, K., G. P. Liu, et al. (2014). "A Graphene Oxide Membrane with Highly Selective Molecular Separation of Aqueous Organic Solution." Angewandte Chemie-International Edition **53**(27): 6929-6932.

Huang, Q. G., X. Y. Shi, et al. (2008). "Tunable Synthesis and Immobilization of Zero-Valent Iron Nanoparticles for Environmental Applications." Environmental Science & Technology **42**(23): 8884-8889.

Huang, Y. H., P. K. Peddi, et al. (2013). "Hybrid zero-valent iron process for removing heavy metals and nitrate from flue-gas-desulfurization wastewater." Separation and Purification Technology **118**: 690-698.

Huling, S. G. and B. Pivetz, E. (2006). In-situ Chemical Oxidation. EPA-Engineering Issue. Washington D.C., U.S. Environmental Protection Agency (EPA)**:** 60.

Hwang, I., H. S. Kim, et al. (2010). "Atmospherically Stable Nanoscale Zero-Valent Iron Particles Formed under Controlled Air Contact: Characteristics and Reactivity." Environmental Science & Technology **44**(5): 1760-1766.

Johnson, T. L., M. M. Scherer, et al. (1996). "Kinetics of halogenated organic compound degradation by iron metal." Environmental Science & Technology **30**(8): 2634-2640.

Johnson, T. L., W. Fish, et al. (1998). "Degradation of carbon tetrachloride by iron metal: Complexation effects on the oxide surface." Journal of Contaminant Hydrology **29**(4): 379-398.

Joo, S. H., A. J. Feitz, et al. (2004). "Oxidative degradation of the carbothioate herbicide, molinate, using nanoscale zero-valent iron." Environmental Science & Technology **38**(7): 2242-2247.

Joo, S. H., A. J. Feitz, et al. (2005). "Quantification of the oxidizing capacity of nanoparticulate zero-valent iron." Environmental Science & Technology **39**(5): 1263-1268.

Jordan, N., A. Ritter, et al. (2013). "Adsorption mechanism of selenium(VI) onto maghemite." Geochimica Et Cosmochimica Acta **103**: 63-75.

Joseph, N., P. Ahmadiannamini, et al. (2014). "Layer-by-layer preparation of polyelectrolyte multilayer membranes for separation." Polymer Chemistry **5**(6): 1817-1831.

Joshi, R. K., P. Carbone, et al. (2014). "Precise and Ultrafast Molecular Sieving Through Graphene Oxide Membranes." Science **343**(6172): 752-754.

Jung, D. H., S. Y. Cho, et al. (2003). "Preparation and performance of a Nafion (R)/montmorillonite nanocomposite membrane for direct methanol fuel cell." Journal of Power Sources **118**(1-2): 205-211.

Kanel, S. R., B. Manning, et al. (2005). "Removal of arsenic(III) from groundwater by nanoscale zero-valent iron." Environmental Science & Technology **39**(5): 1291-1298.

Kanel, S. R., R. R. Goswami, et al. (2008). "Two dimensional transport characteristics of surface stabilized zero-valent iron nanoparticles in porous media." Environmental Science & Technology **42**(3): 896-900.

Kapur, V., J. C. Charkoudian, et al. (1996). "Hydrodynamic permeability of hydrogels stabilized within porous membranes." Industrial & Engineering Chemistry Research **35**(9): 3179-3185.

Karppi, J., S. Akerman, et al. (2010). "Adsorption of metal cations from aqueous solutions onto the pH responsive poly(vinylidene fluoride grafted poly(acrylic acid) (PVDF-PAA) membrane." Journal of Polymer Research **17**(1): 71-76.

Keenan, C. R. and D. L. Sedlak (2008). "Factors affecting the yield of oxidants from the reaction of manoparticulate zero-valent iron and oxygen." Environmental Science & Technology **42**(4): 1262-1267.

Kharaka, Y. K., G. Ambats, et al. (1996). "Removal of selenium from contaminated agricultural drainage water by nanofiltration membranes." Applied Geochemistry **11**(6): 797-802.

Kim, E. J., J. H. Kim, et al. (2011). "Facile Synthesis and Characterization of Fe/FeS Nanoparticles for Environmental Applications." Acs Applied Materials & Interfaces **3**(5): 1457-1462.

Kim, E. J., J. H. Kim, et al. (2014). "Effects of Metal Ions on the Reactivity and Corrosion Electrochemistry of Fe/FeS Nanoparticles." Environmental Science & Technology **48**(7): 4002-4011.

Kim, H., H. J. Hong, et al. (2008). "Degradation of trichloroethylene by zero-valent iron immobilized in cationic exchange membrane." Desalination **223**(1-3): 212-220.

Kim, J. and B. Van der Bruggen (2010). "The use of nanoparticles in polymeric and ceramic membrane structures: Review of manufacturing procedures and performance improvement for water treatment." Environmental Pollution **158**(7): 2335-2349.

Kitajima, N., S. Fukuzumi, et al. (1978). "Formation of Superoxide Ion during Decomposition of Hydrogen-Peroxide on Supported Metal-Oxides." Journal of Physical Chemistry **82**(13): 1505-1509.

Klas, S. and D. W. Kirk (2013). "Understanding the positive effects of low pH and limited aeration on selenate removal from water by elemental iron." Separation and Purification Technology **116**: 222-229.

Kosinov, N., C. Auffret, et al. (2014). "Influence of support morphology on the detemplation and permeation of ZSM-5 and SSZ-13 zeolite membranes." Microporous and Mesoporous Materials **197**: 268-277.

Kwan, W. P. and B. M. Voelker (2003). "Rates of hydroxyl radical generation and organic compound oxidation in mineral-catalyzed Fenton-like systems." Environmental Science & Technology **37**(6): 1150-1158.

Ladhe, A. R., P. Frailie, et al. (2009). "Thiol-functionalized silica-mixed matrix membranes for silver capture from aqueous solutions: Experimental results and modeling." Journal of Membrane Science **326**(2): 460-471.

Laine, D. F. and I. F. Cheng (2007). "The destruction of organic pollutants under mild reaction conditions: A review." Microchemical Journal **85**(2): 183-193.

Lalvani, S. B. (2004). Selenium Removal From Agricultural L Drainage Water: Lab Scale studies. Sacramento, CA, Department of Water Resources.

Lau, W. J., A. F. Ismail, et al. (2012). "A recent progress in thin film composite membrane: A review." Desalination **287**: 190-199.

Lee, C. and D. L. Sedlak (2008). "Enhanced Formation of Oxidants from Bimetallic Nickel-Iron Nanoparticles in the Presence of Oxygen." Environmental Science & Technology **42**(22): 8528-8533.

Lee, C. and D. L. Sedlak (2009). "A novel homogeneous Fenton-like system with Fe(III)-phosphotungstate for oxidation of organic compounds at neutral pH values." Journal of Molecular Catalysis a-Chemical **311**(1-2): 1-6.

Lee, C., C. R. Keenan, et al. (2008). "Polyoxometalate-enhanced oxidation of organic compounds by nanoparticulate zero-valent iron and ferrous ion in the presence of oxygen." Environmental Science & Technology **42**(13): 4921-4926.

Lee, Y. and W. Lee (2010). "Degradation of trichloroethylene by Fe(II) chelated with cross-linked chitosan in a modified Fenton reaction." Journal of Hazardous Materials **178**(1-3): 187-193.

Lee, Y. N., R. M. Lago, et al. (2001). "Hydrogen peroxide decomposition over Ln(1-x)A(x)MnO(3) (Ln = La or Nd and A = K or Sr) perovskites." Applied Catalysis A-General **215**(1-2): 245-256.

Lemly, A. D. (2004). "Aquatic selenium pollution is a global environmental safety issue." Ecotoxicology and Environmental Safety **59**(1): 44-56.

Lewis, S. R., S. Datta, et al. (2011). "Reactive nanostructured membranes for water purification." Proc Natl Acad Sci U S A **108**(21): 8577-8582.

Lewis, S., A. Lynch, et al. (2009). "Chelate-Modified Fenton Reaction for the Degradation of Trichloroethylene in Aqueous and Two-Phase Systems." Environmental Engineering Science **26**(4): 849-859.

Li, K., M. I. Stefan, et al. (2007). "Trichloroethene degradation by UV/H2O2 advanced oxidation process: Product study and kinetic modeling." Environmental Science & Technology **41**(5): 1696-1703.

Li, N. N., A. G. Fane, et al. (2008). Advanced Membrane Technology and Applications, Wiley-AIChE.

Li, S. J., T. L. Li, et al. (2010). "Reduction and immobilization of chromium(VI) by nano-scale Fe-0 particles supported on reproducible PAA/PVDF membrane." Journal of Environmental Monitoring **12**(5): 1153-1158.

Li, Y. C., L. G. Bachas, et al. (2007). "Selected chloro-organic detoxifications by polychelate (Poly(acrylic acid)) and citrate-based Fenton reaction at neutral pH environment." Industrial & Engineering Chemistry Research **46**(24): 7984-7992.

Lien, H. L. and W. X. Zhang (2007). "Nanoscale Pd/Fe bimetallic particles: Catalytic effects of palladium on hydrodechlorination." Applied Catalysis B-Environmental **77**(1-2): 110-116.

Lim, H., J. Lee, et al. (2006). "Highly active heterogeneous Fenton catalyst using iron oxide nanoparticles immobilized in alumina coated mesoporous silica." Chemical Communications(4): 463-465.

Lin, S. S. and M. D. Gurol (1998). "Catalytic decomposition of hydrogen peroxide on iron oxide: Kinetics, mechanism, and implications." Environmental Science & Technology **32**(10): 1417-1423.

Liu, C. C., D. H. Tseng, et al. (2006). "Effects of ferrous ions on the reductive dechlorination of trichloroethylene by zero-valent iron." Journal of Hazardous Materials **136**(3): 706-713.

Liu, G. J., J. F. Ding, et al. (1999). "Preparation and properties of nanoporous triblock copolymer membranes." Angewandte Chemie-International Edition **38**(6): 835-838.

Loeb Sidney, S. S. (1964). High flow porous membranes for separating water from saline solutions, University of California at Los Angeles.

Lowry, G. V. and K. M. Johnson (2004). "Congener-specific dechlorination of dissolved PCBs by microscale and nanoscale zerovalent iron in a water/methanol solution." Environmental Science & Technology **38**(19): 5208-5216.

Lowry, G. V., K. B. Gregory, et al. (2012). "Transformations of Nanomaterials in the Environment." Environmental Science & Technology **46**(13): 6893-6899.

Madaeni, S. S., S. Zinadini, et al. (2011). "A new approach to improve antifouling property of PVDF membrane using in situ polymerization of PAA functionalized TiO2 nanoparticles." Journal of Membrane Science **380**(1-2): 155-162.

Maiers, D. T., P. L. Wichlacz, et al. (1988). "Selenate Reduction by Bacteria from a Selenium-Rich Environment." Applied and Environmental Microbiology **54**(10): 2591-2593.

Majumder, M., N. Chopra, et al. (2005). "Nanoscale hydrodynamics - Enhanced flow in carbon nanotubes." Nature **438**(7064): 44-44.

Malusis, M. A., C. D. Shackelford, et al. (2003). "Flow and transport through clay membrane barriers." Engineering Geology **70**(3-4): 235-248.

Maneval, J. E., G. Klein, et al. (1985). Selenium Removal From Drinking Water By Ion Exchange, United States Environmenatla Protection Agency.

Marques, D. S., U. Vainio, et al. (2013). "Self-assembly in casting solutions of block copolymer membranes." Soft Matter **9**(23): 5557-5564.

M'Bareck, C. O., Q. T. Nguyen, et al. (2006). "Fabrication of ion-exchange ultrafiltration membranes for water treatment I. Semi-interpenetrating polymer networks of polysulfone and poly(acrylic acid)." Journal of Membrane Science **278**(1-2): 10-18.

Meeks, N. D., E. Davis, et al. (2013). "Mercury removal by thiol-functionalized metal oxide-carbon black sorbent and mixed-matrix membranes." Environmental Progress & Sustainable Energy **32**(3): 705-714.

Meeks, N. D., V. Smuleac, et al. (2012). "Iron-Based Nanoparticles for Toxic Organic Degradation: Silica Platform and Green Synthesis." Industrial & Engineering Chemistry Research **51**(28): 9581-9590.

Meyer, D. E., S. Hampson, et al. (2009). "A Study of Groundwater Matrix Effects for the Destruction of Trichloroethylene Using Fe/Pd Nanoaggregates." Environmental Progress & Sustainable Energy **28**(4): 507-518.

Mika, A. M. and R. F. Childs (2001). "Calculation of the hydrodynamic permeability of gels and gel-filled microporous membranes." Industrial & Engineering Chemistry Research **40**(7): 1694-1705.

Miller, C. M. and R. L. Valentine (1995). "Hydrogen Peroxide Decomposition and Quinoline Degradation in the Presence of Aquifer Material." Water Research **29**(10): 2353-2359.

Miller, C. M. and R. L. Valentine (1999). "Mechanistic studies of surface catalyzed H2O2 decomposition and contaminant degradation in the presence of sand." Water Research **33**(12): 2805-2816.

Mohn, W. W., K. Westerberg, et al. (1997). "Aerobic biodegradation of biphenyl and polychlorinated biphenyls by arctic soil microorganisms." Applied and Environmental Microbiology **63**(9): 3378-3384.

Mondal, K., G. Jegadeesan, et al. (2004). "Removal of selenate by Fe and NiFe nanosized particles." Industrial & Engineering Chemistry Research **43**(16): 4922-4934.

Monticelli, O., A. Bottino, et al. (2007). "Preparation and properties of polysulfone-clay composite membranes." Journal of Applied Polymer Science **103**(6): 3637-3644.

Murphy, A. P. (1988). "Removal of Selenate from Water by Chemical-Reduction." Industrial & Engineering Chemistry Research **27**(1): 187-191.

Myneni, S. C. B., T. K. Tokunaga, et al. (1997). "Abiotic selenium redox transformations in the presence of Fe(II,III) oxides." Science **278**(5340): 1106-1109.

Nasef, M. M. and E. S. A. Hegazy (2004). "Preparation and applications of ion exchange membranes by radiation-induced graft copolymerization of polar monomers onto non-polar films." Progress in Polymer Science **29**(6): 499-561.

Nunes, S. P., A. R. Behzad, et al. (2011). "Switchable pH-Responsive Polymeric Membranes Prepared via Block Copolymer Micelle Assembly." Acs Nano **5**(5): 3516-3522.

Nunes, S. P. and K. V. Peinemann (2006). Membrane Technology: in the Chemical Industry, Wiley-VCH.

Nurmi, J. T., P. G. Tratnyek, et al. (2005). "Characterization and properties of metallic iron nanoparticles: Spectroscopy, electrochemistry, and kinetics." Environmental Science & Technology **39**(5): 1221-1230.

Okada, S., K. Mori, et al. (2011). "Active Site Design in a Core-Shell Nanostructured Catalyst for a One-Pot Oxidation Reaction." Chemistry-a European Journal **17**(33): 9047-9051.

Olegario, J. T., N. Yee, et al. (2010). "Reduction of Se(VI) to Se(-II) by zerovalent iron nanoparticle suspensions." Journal of Nanoparticle Research **12**(6): 2057-2068.

Oppelt, T. E. (2001). Selenium Treatment/Removal Alternatives Demonstration Project, National Risk Management Research Laboratory.

Oremland, R. S., J. T. Hollibaugh, et al. (1989). "Selenate Reduction to Elemental Selenium by Anaerobic-Bacteria in Sediments and Culture - Biogeochemical Significance of a Novel, Sulfate-Independent Respiration." Applied and Environmental Microbiology **55**(9): 2333-2343.

Orr, V., L. Y. Zhong, et al. (2013). "Recent advances in bioprocessing application of membrane chromatography." Biotechnology Advances **31**(4): 450-465.

Palai, T. and P. K. Bhattacharya (2013). "Kinetics of lactose conversion to galacto-oligosaccharides by beta-galactosidase immobilized on PVDF membrane." Journal of Bioscience and Bioengineering **115**(6): 668-673.

Palai, T., A. K. Singh, et al. (2014). "Enzyme, beta-galactosidase immobilized on membrane surface for galacto-oligosaccharides formation from lactose: Kinetic study with feed flow under recirculation loop." Biochemical Engineering Journal **88**: 68-76.

Park, C., J. Yoon, et al. (2003). "Enabling nanotechnology with self assembled block copolymer patterns (vol 44, pg 6725, 2003)." Polymer **44**(25): 7779-7779.

Park, S. J., R. K. Cheedrala, et al. (2012). "Nanofiltration membranes based on polyvinylidene fluoride nanofibrous scaffolds and crosslinked polyethyleneimine networks." Journal of Nanoparticle Research **14**(7).

Parshetti, G. K. and R. A. Doong (2012). "Dechlorination of chlorinated hydrocarbons by bimetallic Ni/Fe immobilized on polyethylene glycol-grafted rnicrofiltration membranes under anoxic conditions." Chemosphere **86**(4): 392-399.

Patil, A. B., P. Kandwal, et al. (2013). "Evaluation of DMDOHEMA based supported liquid membrane system for high level waste remediation under simulated conditions." Journal of Membrane Science **442**: 48-56.

Paul, D. R. and L. M. Robeson (2008). "Polymer nanotechnology: Nanocomposites." Polymer **49**(15): 3187-3204.

Peak, D. and D. L. Sparks (2002). "Mechanisms of selenate adsorption on iron oxides and hydroxides." Environmental Science & Technology **36**(7): 1460-1466.

Peng, S., C. Wang, et al. (2006). "Synthesis and stabilization of monodisperse Fe nanoparticles." Journal of the American Chemical Society **128**(33): 10676-10677.

Pham, A. L. T., C. Lee, et al. (2009). "A Silica-Supported Iron Oxide Catalyst Capable of Activating Hydrogen Peroxide at Neutral pH Values." Environmental Science & Technology **43**(23): 8930-8935.

Pham, A. L. T., F. M. Doyle, et al. (2012). "Inhibitory Effect of Dissolved Silica on H2O2 Decomposition by Iron(III) and Manganese(IV) Oxides: Implications for H2O2-Based In Situ Chemical Oxidation." Environmental Science & Technology **46**(2): 1055-1062.

Phenrat, T., H. J. Kim, et al. (2009). "Particle Size Distribution, Concentration, and Magnetic Attraction Affect Transport of Polymer-Modified Fe-0 Nanoparticles in Sand Columns." Environmental Science & Technology **43**(13): 5079-5085.

Pignatello, J. J. and G. Chapa (1994). "Degradation of Pcbs by Ferric Ion, Hydrogen-Peroxide and Uv-Light." Environmental Toxicology and Chemistry **13**(3): 423-427.

Pignatello, J. J., E. Oliveros, et al. (2006). "Advanced oxidation processes for organic contaminant destruction based on the Fenton reaction and related chemistry." Critical Reviews in Environmental Science and Technology **36**(1): 1-84.

Pouran, S. R., A. A. A. Raman, et al. (2014). "Review on the application of modified iron oxides as heterogeneous catalysts in Fenton reactions." Journal of Cleaner Production **64**: 24-35.

Prince, J. A., G. Singh, et al. (2012). "Preparation and characterization of highly hydrophobic poly(vinylidene fluoride) - Clay nanocomposite nanofiber membranes (PVDF-clay NNMs) for desalination using direct contact membrane distillation." Journal of Membrane Science **397**: 80-86.

Qian, S. H., G. Q. Huang, et al. (2000). "Studies of adsorption behavior of crosslinked chitosan for Cr(VI), Se(VI)." Journal of Applied Polymer Science **77**(14): 3216-3219.

Qiu, C. Q., S. R. Qi, et al. (2011). "Synthesis of high flux forward osmosis membranes by chemically crosslinked layer-by-layer polyelectrolytes." Journal of Membrane Science **381**(1-2): 74-80.

Qiu, S. R., H. F. Lai, et al. (2000). "Removal of contaminants from aqueous solution by reaction with iron surfaces." Langmuir **16**(5): 2230-2236.

Qiu, X. Y., H. Z. Yu, et al. (2013). "Selective Separation of Similarly Sized Proteins with Tunable Nanoporous Block Copolymer Membranes." Acs Nano **7**(1): 768-776.

Ravikumar, J. X. and M. D. Gurol (1994). "Chemical Oxidation of Chlorinated Organics by Hydrogen-Peroxide in the Presence of Sand." Environmental Science & Technology **28**(3): 394-400.

Russell, H. H., J. E. Matthews, et al. (1992). TCE Removal from Contaminated Soil and Ground Water. EPA Ground Water Issue, United States Environmental Protection Agency.

Saleh, A. M. and A. A. Jones (1984). "The Crystallinity and Surface Characteristics of Synthetic Ferrihydrite and Its Relationship to Kaolinite Surfaces." Clay Minerals **19**(5): 745-755.

Sartowska, B. A., O. L. Orelovitch, et al. (2012). "Nanopores with controlled profiles in track-etched membranes." Nukleonika **57**(4): 575-579.

Savage, N. and M. S. Diallo (2005). "Nanomaterials and water purification: Opportunities and challenges." Journal of Nanoparticle Research **7**(4-5): 331-342.

Scheinost, A. C. and L. Charlet (2008). "Selenite reduction by mackinawite, magnetite and siderite: XAS characterization of nanosized redox products." Environmental Science & Technology **42**(6): 1984-1989.

Schellenger, A. E. P. and P. Larese-Casanova (2013). "Oxygen Isotope Indicators of Selenate Reaction with Fe(II) and Fe(III) Hydroxides." Environmental Science & Technology **47**(12): 6254-6262.

Schug, T. T., A. F. Johnson, et al. (2013). "ONE Nano: NIEHS's Strategic Initiative on the Health and Safety Effects of Engineered Nanomaterials." Environ Health Perspect.

Schwartz, R. D., A. L. Williams, et al. (1980). "Microbial-Production of 4,4'-Dihydroxybiphenyl - Biphenyl Hydroxylation by Fungi." Applied and Environmental Microbiology **39**(4): 702-708.

Schwertmann, U. and H. Fechter (1982). "The Point of Zero Charge of Natural and Synthetic Ferrihydrites and Its Relation to Adsorbed Silicate." Clay Minerals **17**(4): 471-476.

Sedlak, D. L. and A. W. Andren (1991). "Aqueous-Phase Oxidation of Polychlorinated-Biphenyls by Hydroxyl Radicals." Environmental Science & Technology **25**(8): 1419-1427.

Seol, Y. and I. Javandel (2008). "Citric acid-modified Fenton's reaction for the oxidation of chlorinated ethylenes in soil solution systems." Chemosphere **72**(4): 537-542.

Seteni, B., J. C. Ngila, et al. (2013). "Dechlorination of 3,3 ',4,4 '-tetrachlorobiphenyl (PCB77) in water, by nickel/iron nanoparticles immobilized on L-lysine/PAA/PVDF membrane." Physics and Chemistry of the Earth **66**: 60-67.

Sheng, C. J., S. Wijeratne, et al. (2014). "Facilitated ion transport through polyelectrolyte multilayer films containing metal-binding ligands." Journal of Membrane Science **459**: 169-176.

Singh, N., J. Wang, et al. (2008). "Surface-initiated atom transfer radical polymerization: A new method for preparation of polymeric membrane adsorbers." Journal of Membrane Science **309**(1-2): 64-72.

Singh, N., S. M. Husson, et al. (2005). "Surface modification of microporous PVDF membranes by ATRP." Journal of Membrane Science **262**(1-2): 81-90.

Smuleac, V., L. Bachas, et al. (2010). "Aqueous-phase synthesis of PAA in PVDF membrane pores for nanoparticle synthesis and dichlorobiphenyl degradation." Journal of Membrane Science **346**(2): 310-317.

Smuleac, V., R. Varma, et al. (2011). "Green synthesis of Fe and Fe/Pd bimetallic nanoparticles in membranes for reductive degradation of chlorinated organics." Journal of Membrane Science **379**(1-2): 131-137.

Sonstegard, J., T. Pickett, et al. (2008). Full Scale Operation of GE ABMet® Biological Technology for the Removal of Selenium from FGD Wastewaters, GE Power and Water.

Stuart, M. A. C., W. T. S. Huck, et al. (2010). "Emerging applications of stimuli-responsive polymer materials." Nature Materials **9**(2): 101-113.

Su, C. M. and R. W. Puls (2001). "Arsenate and arsenite removal by zerovalent iron: Effects of phosphate, silicate, carbonate, borate, sulfate, chromate, molybdate, and nitrate, relative to chloride." Environmental Science & Technology **35**(22): 4562-4568.

Sun, S. P. and A. T. Lemley (2011). "p-Nitrophenol degradation by a heterogeneous Fenton-like reaction on nano-magnetite: Process optimization, kinetics, and degradation pathways." Journal of Molecular Catalysis a-Chemical **349**(1-2): 71-79.

Sun, Y. P., X. Q. Li, et al. (2006). "Characterization of zero-valent iron nanoparticles." Advances in Colloid and Interface Science **120**(1-3): 47-56.

Tee, Y. H. and D. Bhattacharyya (2008). Synthesis of Chitosan Membrane-Embedded Bimetallic Nanoparticles for the Remediation of Chlorinated Organics. Advanced Membrane Technology and Applications. W. S. Ho, A. G. Fane, N. Li and T. Matsuura, John Wiley**:** 189-216.

Tee, Y. H., L. Bachas, et al. (2009). "Degradation of Trichloroethylene and Dichlorobiphenyls by Iron-Based Bimetallic Nanoparticles." Journal of Physical Chemistry C **113**(22): 9454-9464.

Thompson, G. E. (1997). "Porous anodic alumina: Fabrication, characterization and applications." Thin Solid Films **297**(1-2): 192-201.

Tracey, E. M. and R. H. Davis (1994). "Protein Fouling of Track-Etched Polycarbonate Microfiltration Membranes." Journal of Colloid and Interface Science **167**(1): 104-116.

Tseng, H. H., J. G. Su, et al. (2011). "Synthesis of granular activated carbon/zero valent iron composites for simultaneous adsorption/dechlorination of trichloroethylene." Journal of Hazardous Materials **192**(2): 500-506.

Tyre, B. W., R. J. Watts, et al. (1991). "Treatment of 4 Biorefractory Contaminants in Soils Using Catalyzed Hydrogen-Peroxide." Journal of Environmental Quality **20**(4): 832-838.

Ulbricht, M. (2006). "Advanced functional polymer membranes." Polymer **47**(7): 2217-2262.

Valentine, R. L. and H. C. A. Wang (1998). "Iron oxide surface catalyzed oxidation of quinoline by hydrogen peroxide." Journal of Environmental Engineering-Asce **124**(1): 31-38.

vandeWitte, P., P. J. Dijkstra, et al. (1996). "Phase separation processes in polymer solutions in relation to membrane formation." Journal of Membrane Science **117**(1-2): 1-31.

Venkatachalam, K., X. Arzuaga, et al. (2008). "Reductive dechlorination of 3,3 ',4,4 '-tetrachlorobiphenyl (PCB77) using palladium or palladium/iron nanoparticles and assessment of the reduction in toxic potency in vascular endothelial cells." Journal of Hazardous Materials **159**(2-3): 483-491.

Venny, S. Y. Gan, et al. (2012). "Inorganic chelated modified-Fenton treatment of polycyclic aromatic hydrocarbon (PAH)-contaminated soils." Chemical Engineering Journal **180**: 1-8.

Voinov, M. A., J. O. S. Pagan, et al. (2011). "Surface-Mediated Production of Hydroxyl Radicals as a Mechanism of Iron Oxide Nanoparticle Biotoxicity." Journal of the American Chemical Society **133**(1): 35-41.

Walther, J. H., K. Ritos, et al. (2013). "Barriers to Superfast Water Transport in Carbon Nanotube Membranes." Nano Letters **13**(5): 1910-1914.

Wandera, D., S. R. Wickramasinghe, et al. (2010). "Stimuli-responsive membranes." Journal of Membrane Science **357**(1-2): 6-35.

Wang, C. B. and W. X. Zhang (1997). "Synthesizing nanoscale iron particles for rapid and complete dechlorination of TCE and PCBs." Environmental Science & Technology **31**(7): 2154-2156.

Wang, F., T. L. Chen, et al. (1998). "Sodium sulfonate-functionalized poly(ether ether ketone)s." Macromolecular Chemistry and Physics **199**(7): 1421-1426.

Wang, G. J. and J. B. F. N. Engberts (1994). "Synthesis and Catalytic Properties of Cross-Linked Hydrophobically Associating Poly(Alkylmethyldiallylammonium Bromides)." Journal of Organic Chemistry **59**(15): 4076-4081.

Wang, X. Y., C. Chen, et al. (2008). "Preparation and characterization of PAA/PVDF membrane-immobilized Pd/Fe nanoparticles for dechlorination of trichloroacetic acid." Water Research **42**(18): 4656-4664.

Wang, X. Y., J. C. Yang, et al. (2013). "Characterization and regeneration of Pd/Fe nanoparticles immobilized in modified PVDF membrane." Journal of the Taiwan Institute of Chemical Engineers **44**(3): 386-392.

Watts, R. J. and A. L. Teel (2005). "Chemistry of modified Fenton's reagent (catalyzed H2O2 propagations-CHP) for in situ soil and groundwater remediation." Journal of Environmental Engineering-Asce **131**(4): 612-622.

Watts, R. J., M. D. Udell, et al. (1999). "Fenton-like soil remediation catalyzed by naturally occurring iron minerals." Environmental Engineering Science **16**(1): 93-103.

Wei, G., B. M. Fan, et al. (2013). "Preparation of a nano-scale ceramic membrane and its application in the medium-pressure boiler with phosphate treatment." Desalination **322**: 167-175.

Winnik, F. M., A. Morneau, et al. (1998). "Polyacrylic acid pore-filled microporous membranes and their use in membrane-mediated synthesis of nanocrystalline ferrihydrite." Canadian Journal of Chemistry-Revue Canadienne De Chimie **76**(1): 10-17.

Wood, T. K. (2008). "Molecular approaches in bioremediation." Current Opinion in Biotechnology **19**(6): 572-578.

Wu, L. F. and S. M. C. Ritchie (2008). "Enhanced dechlorination of trichloroethylene by membrane-supported Pd-coated iron nanoparticles." Environmental Progress **27**(2): 218-224.

Wycisk, R. and P. N. Pintauro (1996). "Sulfonated polyphosphazene ion-exchange membranes." Journal of Membrane Science **119**(1): 155-160.

Xiao, L., A. B. Isner, et al. (2013). "Temperature responsive hydrogel with reactive nanoparticles." Journal of Applied Polymer Science **128**(3): 1804-1814.

Xu, J. and D. Bhattacharyya (2005). "Membrane-based bimetallic nanoparticles for environmental remediation: Synthesis and reactive properties." Environmental Progress **24**(4): 358-366.

Xu, J. and D. Bhattacharyya (2007). "Fe/Pd nanoparticle immobilization in microfiltration membrane pores: Synthesis, characterization, and application in the dechlorination of polychlorinated biphenyls." Industrial & Engineering Chemistry Research **46**(8): 2348-2359.

Xu, J. and D. Bhattacharyya (2008). "Modeling of Fe/Pd nanoparticle-based functionalized membrane reactor for PCB dechlorination at room temperature." Journal of Physical Chemistry C **112**(25): 9133-9144.

Xu, J., A. Dozier, et al. (2005). "Synthesis of nanoscale bimetallic particles in polyelectrolyte membrane matrix for reductive transformation of halogenated organic compounds." Journal of Nanoparticle Research **7**(4-5): 449-467.

Xue, X. F., K. Hanna, et al. (2009). "Adsorption and oxidation of PCP on the surface of magnetite: Kinetic experiments and spectroscopic investigations." Applied Catalysis B-Environmental **89**(3-4): 432-440.

Yamaguchi, N. U., M. Okazaki, et al. (1999). "Volume changes due to SO42-, SeO42-, and H2PO4- adsorption on amorphous iron(III) hydroxide in an aqueous suspension." Journal of Colloid and Interface Science **209**(2): 386-391.

Yang, J. C., X. Y. Wang, et al. (2014). "Investigation of PAA/PVDF-NZVI hybrids for metronidazole removal: Synthesis, characterization, and reactivity characteristics." Journal of Hazardous Materials **264**: 269-277.

Yang, S., N. Yoshida, et al. (2008). "Anaerobic biodegradation of biphenyl in various paddy soils and river sediment." Chemosphere **71**(2): 328-336.

Yang, X. J., X. M. Xu, et al. (2013). "Iron Oxychloride (FeOCl): An Efficient Fenton-Like Catalyst for Producing Hydroxyl Radicals in Degradation of Organic Contaminants." Journal of the American Chemical Society **135**(43): 16058-16061.

Yeh, C. K.-J., W.-S. Chen, et al. (2004). "Production of Hydroxyl Radicals from the Decomposition of Hydrogen Peroxide Catalyzed by Various Iron Oxides at pH 7." Practice Periodical of Hazardous, Toxic, and Radioactive Waste Management **8**(3): 161-165.

Yoon, I. H., K. W. Kim, et al. (2011). "Reduction and adsorption mechanisms of selenate by zero-valent iron and related iron corrosion." Applied Catalysis B-Environmental **104**(1-2): 185-192.

Zalusky, A. S., R. Olayo-Valles, et al. (2002). "Ordered nanoporous polymers from polystyrene-polylactide block copolymers." Journal of the American Chemical Society **124**(43): 12761-12773.

Zelmanov, G. and R. Semiat (2008). "Iron(3) oxide-based nanoparticles as catalysts in advanced organic aqueous oxidation." Water Research **42**(1-2): 492-498.

Zhan, J. J., B. Sunkara, et al. (2011). "Carbothermal Synthesis of Aerosol-Based Adsorptive-Reactive Iron-Carbon Particles for the Remediation of Chlorinated Hydrocarbons." Industrial & Engineering Chemistry Research **50**(23): 13021-13029.

Zhan, Z. B. and Y. Lei (2014). "Sub-100-nm Nanoparticle Arrays with Perfect Ordering and Tunable and Uniform Dimensions Fabricated by Combining Nanoimprinting with Ultrathin Alumina Membrane Technique." Acs Nano **8**(4): 3862-3868.

Zhang, P. C. and D. L. Sparks (1990). "Kinetics of Selenate and Selenite Adsorption Desorption at the Goethite Water Interface." Environmental Science & Technology **24**(12): 1848-1856.

Zhang, W. B., Y. Z. Zhu, et al. (2014). "Salt-Induced Fabrication of Superhydrophilic and Underwater Superoleophobic PAA-g-PVDF Membranes for Effective Separation of Oil-in-Water Emulsions." Angewandte Chemie-International Edition **53**(3): 856-860.

Zhang, W. X. (2003). "Nanoscale iron particles for environmental remediation: An overview." Journal of Nanoparticle Research **5**(3-4): 323-332.

Zhang, Y. Q., J. F. Wang, et al. (2005). "Removal of selenate from water by zerovalent iron." Journal of Environmental Quality **34**(2): 487-495.

Zheng, T. H., J. J. Zhan, et al. (2008). "Reactivity characteristics of nanoscale zerovalent iron-silica composites for trichloroethylene remediation." Environmental Science & Technology **42**(12): 4494-4499.

Zhu, B. W. and T. T. Lim (2007). "Catalytic reduction of Chlorobenzenes with Pd/Fe nanoparticles: reactive sites, catalyst stability, particle aging, and regeneration." Environmental Science & Technology **41**(21): 7523-7529.

Zingaro, R. A., D. C. Dufner, et al. (1997). "Reduction of oxoselenium anions by iron(II) hydroxide." Environment International **23**(3): 299-304.

Vita

Minghui Gui received his B.S. degree in Chemical Engineering from East China University of Science and Technology in 2007. After that, he continued his master studies there for two years. He started his Ph.D. studies in Chemical Engineering program at the University of Kentucky in 2009 fall.

HONORS AND AWARDS

- Third Place (out of 87) in the Graduate Student Poster Competition, NIEHS-Superfund Research Program (SRP) Annual Meeting, Baton Rouge, LA (Oct 2013) (Post Award Webinar, Apr 2014)
- First Place in NSF Research Experience for Undergraduates (REU) Summer Program Poster Competition (Graduate Student Mentor) (Aug 2013)
- Elias Klein Founders' Travel Award, $500 support for fifteen graduate students attending the North American Membrane Society (NAMS) 23rd Annual Meeting, Boise, ID (Jun 2013)
- Graduate Student Travel Fund, University of Kentucky ($400 per year) (2010-2013)
- First Place in the Application Contest of Chemical Engineering, ECUST (Team Leader) (Jun 2006)
- Outstanding Undergraduate Scholarship (top 15% of Chem. Eng. program) (2003-2007)

PUBLICATIONS

Gui, M., Papp, J. K., Colburn A. S., Teng, X., Ormsbee, L., and Bhattacharyya, D., "Engineered Iron/iron Oxide Functionalized Membrane for Toxic Metal Removal," Journal of Membrane Science, to be submitted.

Gui, M., Ormsbee, L. E., and Bhattacharyya, D., "Reactive Functionalized Membranes for Polychlorinated Biphenyl Degradation," Industrial & Engineering Chemistry Research, 2013, 52 (31), 10430-10440.

Gui, M., Smuleac, V., Ormsbee, L. E., Sedlak, D. L., and Bhattacharyya, D., "Iron Oxide Nanoparticle Synthesis in Aqueous and Membrane Systems for Oxidative Degradation of Trichloroethylene from Water," Journal of Nanoparticle Research, 2012, 14: 861-876.

Lewis, S. R., Datta, S., Gui, M., Coker, E.L., Huggins, F. E., Daunert, S., Bachas, L., and Bhattacharyya, D., "Reactive Nanostructured Membranes for Water Purification," Proceedings of the National Academy of Sciences, 2011, 108, 8577-8582.

PRESENTATIONS

Gui M., Papp, J. Ormsbee L. E., Bhattacharyya D., LaMonica D., and Wilf I., "Synthesis of Iron Functionalized Membranes for Polychlorinated Biphenyl (PCB) and Toxic Metal Remediation," NAMS Annual Meeting, Houston, TX, June 2014. (Oral and Poster)

Gui M., Colburn A. S., Bhattacharyya D., "Partial Desalination and Selenium Reduction for Energy Applications," 2014 Kentucky Water Resources Annual Symposium, Lexington, KY, March 2014. (Poster)

Gui M., Ormsbee L. E., and Bhattacharyya D., "Chloro-Organic Detoxification by Membrane Supported Iron/Iron Oxide System," NIEHS-SRP Annual Meeting, Baton Rouge, LA, October 2013. (Poster winner, Post Award Webinar on April 15, 2014)

Gui M., Ormsbee L. E., Bhattacharyya D., "Reactive Functionalized Membranes for Pollutants Degradation," NAMS Annual Meeting, Boise, ID, June 2013. (Oral and Poster)

Gui M., Smuleac V., Bhattacharyya D., "Membrane-Iron Oxide Nanoparticle System for Pollutant Degradation," American Institute of Chemical Engineers (AIChE) Annual Meeting, Pittsburgh, PA, October 2012. (Oral)

Gui M., Ormsbee L. E., Sedlak D. L., Bhattacharyya D., "Complete Detoxification of PCBs by Iron Based Nanostructured Membranes," NIEHS-SRP Annual Meeting, Raleigh, NC, October 2012. (Poster)

Gui M., Smuleac V., Bhattacharyya D., "Water Remediation by Iron/Iron oxide Nanoparticle Catalyzed Free Radical Reactions in Polyacrylic Acid (PAA) Functionalized Polyvinylidene Fluoride (PVDF) Membranes," AIChE Annual Meeting, Minneapolis, MN, October 2011. (Oral)

Gui M., Smuleac V., Ormsbee L. E. Bhattacharyya D., "Iron Based Nanostructured Materials for Water Purification," NIEHS-SRP Annual Meeting, Lexington, KY, October 2011. (Oral)

Gui M., Smuleac V., Ormsbee L. E., Bhattacharyya D., "Water Treatment by Iron-Iron Oxide Nanoparticle Catalyzed Free Radical Reactions in Aqueous Phase and in Polyacrylic Acid (PAA) Functionalized Polyvinylidene Fluoride (PVDF) Membranes," NAMS Annual Meeting, Las Vegas, NV, June 2011. (Oral and Poster)

Gui M., Smuleac V., Bhattacharyya D., "Synthesis of Iron/Iron Oxide Core-Shell Nanoparticle and Its Application in Hydrogen Peroxide and Pollutant Degradation," AIChE Annual Meeting, Salt Lake City, UT, November 2010. (Oral)